# BIOCOMPATIBLE AND ANTIBACTERIAL SILVER TANTALUM OXIDE THIN FILM BY MAGNETRON SPUTTERING FOR SURGICAL APPLICATIONS

**RODIANAH BINTI ALIAS**

**DEPARTMENT OF MECHANICAL ENGINEERING**
**FACULTY OF ENGINEERING**
**UNIVERSITY OF MALAYA**
**KUALA LUMPUR**

**2019**

# BIOCOMPATIBLE AND ANTIBACTERIAL SILVER TANTALUM OXIDE THIN FILM BY MAGNETRON SPUTTERING FOR SURGICAL APPLICATIONS

**RODIANAH BINTI ALIAS**

**THESIS SUBMITTED IN FULFILMENT OF THE REQUIREMENTS FOR THE DEGREE OF DOCTOR OF PHILOSOPHY IN MECHANICAL ENGINEERING**

**DEPARTMENT OF MECHANICAL ENGINEERING**
**FACULTY OF ENGINEERING**
**UNIVERSITY OF MALAYA**
**KUALA LUMPUR**

**2019**

**UNIVERSITY OF MALAYA**

**ORIGINAL LITERARY WORK DECLARATION**

Name of Candidate: Rodianah Binti Alias

Matric No: KHA 150012

Name of Degree: PhD in Mechanical Engineering

Title of Project Paper/Research Report/Dissertation/Thesis ("this Work"):

"Biocompatible and Antibacterial Silver Tantalum Oxide Thin Film by Magnetron Sputtering for Surgical Applications"

Field of Study: Advance Materials/Nanomaterials

I do solemnly and sincerely declare that:

(1) I am the sole author/writer of this Work;
(2) This Work is original;
(3) Any use of any work in which copyright exists was done by way of fair dealing and for permitted purposes and any excerpt or extract from, or reference to or reproduction of any copyright work has been disclosed expressly and sufficiently and the title of the Work and its authorship have been acknowledged in this Work;
(4) I do not have any actual knowledge nor do I ought reasonably to know that the making of this work constitutes an infringement of any copyright work;
(5) I hereby assign all and every rights in the copyright to this Work to the University of Malaya ("UM"), who henceforth shall be owner of the copyright in this Work and that any reproduction or use in any form or by any means whatsoever is prohibited without the written consent of UM having been first had and obtained;
(6) I am fully aware that if in the course of making this Work I have infringed any copyright whether intentionally or otherwise, I may be subject to legal action or any other action as may be determined by UM.

Candidate's Signature Date:

Subscribed and solemnly declared before,

Witness's Signature Date:

Name:

Designation:

## ABSTRACT

Stainless steel (SS) is used extensively for healthcare, hygiene and surgical applications due to its excellent corrosion resistance and adequate mechanical strength. SS grade 316L is the most widely employed stainless steel owing to the high corrosion resistance, good mechanical properties, resistance to sensitization and ease of fabrication. Nonetheless, stainless steel lacks antibacterial activity. To incorporate the antimicrobial characteristic in SS 316L-based surgical instruments, a new nanocomposite thin film coating comprising silver (Ag) and tantalum oxide ($Ta_2O_5$) was deposited by physical vapor deposition (PVD) reactive magnetron sputtering in this research. The delamination of the ceramic layers on the SS 316L substrate is one of the major limitations arising from insufficient crystallization and poor adhesion strength. It was found that the adhesion strength improved in a precisely controlled thermal treatment process. The microstructure, morphology, phases, elemental, structure, micromechanical properties, surface chemistry, hydrophobicity, toxicity and antibacterial performance of the as-deposited and annealed thin film specimens were analyzed to determine the characteristics of the developed layers. The thermal treatment setup involved temperatures of 250 to 850 °C that progressively increased the crystallinity and segregation of Ag at the surface. The highest adhesion strength was achieved when the coated samples were annealed at 400 °C, with 154 % improvement achieved compared to the as-deposited layer. The samples annealed at 400 °C demonstrated excellent antibacterial performance against gram-negative *Escherichia coli* (ATCC 15597) and gram-positive *Staphylococcus aureus* (NCTC 6571) according to inhibition zone measurements. Ag/Ag-$Ta_2O_5$ prepared at 400 °C exhibited significantly superior biocompatibility (cell attachment and proliferation of seeded

human bone marrow-derived mesenchymal stromal cells) compared to Ag/Ag-$Ta_2O_5$ annealed at 700 °C as well as SS 316L.

Keywords: Nano-composite; Magnetron sputtering; Substrate Temperature; Silver-Tantalum oxide; thermal annealing; antibacterial; biocompatibility

## ABSTRAK

Keluli tahan karat (SS) digunakan secara meluas dalam bidang kesihatan, kebersihan dan aplikasi pembedahan disebabkan oleh sifat tahan karat yang sangat baik dan mempunyai kekuatan mekanikal yang memuaskan. SS 316 L antara SS yang digunakan secara meluas kerana mempunyai sifat tahan karat, sifat mekanikal yang baik, tahan terhadap sensitiviti dan senang dibentuk. Untuk menghasilkan peralatan bedah berasakan SS 316L yang bersifat antimikrob, saduran nano komposit filem nipis baru ini terdiri daripada Perak (Ag) and Tantalum oksida ($Ta_2O_5$) telah didepositkan menggunakan Pendepositan Wap Fizikal (PVD) Pelapisan magnetron reaktif (dengan menyalurkan oksigen) dalam kajian ini. Penanggalan lapisan seramik pada substrat SS 316L adalah satu halangan yang besar berpunca daripada penghabluran yang tidak mencukupi dan kekuatan lekatan yang lemah. Ia didapati bahawa kekuatan lekatan telah dipertingkatkan dengan mengawal proses rawatan haba dengan betul. Mikrostruktur, morfologi, fasa, elemen, struktur, sifat mikro mekanikal, kimia permukaan, kehidrofobikan, prestasi antibakteria dan ketoksikan filem nipis baru-didepositkan dan filem nipis-disepuh telah dianalisa untuk menentukan karakter lapisan yang terbentuk. Penyediaan rawatan haba melibatkan suhu dari 250 to 850 °C menunjukkan kenaikan tahap penghabluran dan pengumpulan Ag ke permukaan secara berterusan. Kekuatan kelekatan yang tertinggi dicapai apabila saduran sampel disepuh pada suhu 400 °C, dengan peningkatan kekuatan lekatan sebanyak 154 % apabila dibandingkan dengan lapisan yang baru-didepositkan. Sampel yang disepuh pada suhu 400 °C menunjukkan prestasi antibakteria yang cemerlang terhadap Gram-negative (*Escherichia coli*, ATCC 15597) and a Gram-positive (*Staphylococcus aureus*, NCTC 6571) berdasarkan pengukuran zon perencatan. Ag/Ag-$Ta_2O_5$ yang disediakan pada suhu penyepuhan 400 °C menunjukkan bio keserasian yang sangat ketara (penempelan sel dan percambahan

sumsum tulang manusia yang dihasilkan dari sel Mesenchymal stromal) apabila dibandingkan dengan Ag/Ag-$Ta_2O_5$ yang disediakan pada suhu penyepuhan 700 °C serta SS 316L.

Kata-kata kunci: Komposit-nano; Pelapisan magnetron; Suhu substrat; Silver-Tantalum oksida; penyepuhan termal, antibakteria, bio keserasian

## ACKNOWLEDGEMENTS

All praises and profound gratitude are due to the Allah, the creator of heaven and earth, the initiator of knowledge for the life, health, wisdom and passion. He bestowed on me to reach this level of education and write this final research qualification. I would forever be thankful and grateful for this special honour. He bestowed on me.

My special gratitude and regards go to my supervisors Prof. Dr. Ir. Mohd Hamdi bin Abd Shukor and Dr. Reza Mahmoodian, whose endless guide me on research field until what I am today. His regular visit, progress meeting, asking problems would forever remain in my memory.

I am highly indebted to my entire family members and friends in the supporting emotional, need and everything related to my study. To my great mother Asiah Awang for their parental care, education and prayers; to my kids for being a coolant and understanding during this study life; to all my brothers for the continuous support and to all relatives.

To the entire surface engineering laboratory colleagues here at University of Malaya (UM) such as Madam Hartini, Umi Zalilah, Nur Syahira, Muhammad Rizwan, Nashrah Hani, Nur Maisarah need to be mentioned and acknowledged. Their contributions in one way or the other were significant. A special appreciation to the Dr. Krishnamurthy Ganesan and Dr. Kumutha Malar for their super precious help and contribution in Toxicity and Antibacterial test. A sincere appreciation to the all technical staffs in UM, UTM and also in MIMOS. En. Zaman, En Rafi, Dr. Rizwan, En Zaharuddin, Ms. Yee Mei, Dr. Idris, En. Hanafi and En. Herman are the kind peoples who made a great contribution to finish my research analysis. I want to end my acknowledgement

message with special thanks to Ministry of Higher Education, SLAI section for their sponsorship and University of Malaya, Postgraduate Research Grant-PPP (PG266-2015B) and RU005O-2016 for the fund during my study period. This privilege would never be forgotten.

## TABLE OF CONTENTS

## LIST OF FIGURES

## LIST OF TABLES

List of symbols and abbreviations

| | | |
|---|---|---|
| AgNPs | : | Silver nanoparticles |
| AgNPs-HA | : | Silver nanoparticles – Hydroxyapatite |
| $AgTaO_3$ | : | Silver Tantalite |
| $AgTa_2O_5$ | : | Silver Tantalum Oxide |
| $Ag/AgTa_2O_5$ | : | Silver/Silver Tantalum Oxide |
| Ar | : | Argon |
| AFM | : | Atomic force microscopic |
| β- $Ta_2O_5$ | : | Beta–Tantalum oxide |
| Co-Cr | : | Cobalt-Chromium |
| Cr | : | Chromium |
| CrN-Ag | : | Cromium Nitrate-Silver |
| DC | : | Direct current |
| DLC | : | Diamond like carbon |
| DMEM | : | Dulbecco modified Eagels's Medium |
| ECM | : | Extracellular matrix |
| EDX | : | Energy dispersive x-ray spectrometry |
| Fe | : | Ferum |
| FESEM | : | Field emission scanning electron microscopy |
| FIB | : | Focus ion beam |
| hBMSCs | : | Human Mesenchymal Stem Cells |
| HA | : | Hydroxyapatite |
| HAI | : | Health care-associated infections |
| ICU | : | Intensive Care Unit |
| $L_c$ | : | Critical load |

| | | |
|---|---|---|
| MDR-HAI | : | Multidrug-Hospital Acquired Infection |
| $Mo_2BC$ | : | Molybdenum-boron-carbon |
| Ni | : | Nickel |
| NA | : | Nutrient agar |
| Nb-Ag | : | Niobium-Silver |
| $O_2$ | : | Oxygen |
| PVD | : | Physical Vapor Deposition |
| Pt | : | Platinum |
| RF | : | Radio frequency |
| PTFE | : | 1,1,2,2-tetrafluoroethylene |
| SAED | : | Selected Area Electron Diffraction |
| SEM | : | Scanning electron microscopy |
| SS | : | Stainless Steel |
| Si | : | Silicon |
| SS 316 L | : | Stainless steel 316L |
| Ta | : | Tantalum |
| TaO | : | Tantalum oxide |
| $Ta/Ta_2O_5$ | : | Tantalum/Tantalum oxide |
| $Ta_2O_5$ | : | Tantalum oxide |
| $TaO_2$ | : | Tantalum dioxide |
| $Ta_2O_5$\Ag\ $Ta_2O_5$ | : | Tantalum oxide/Silver/ Tantalum oxide |
| TaON | : | Oxynitride |
| TEM | : | Transmission electron microscopic |
| Ti | : | Titanium |
| Ti-Ag | : | Titanium/silver |

| | | |
|---|---|---|
| Ti-Ag-N/Ag | : | Titanium/silver–Nitrate-Silver |
| TiAlN | : | Titanium–Aluminium-Nitrate |
| TiCN | : | Titanium-Carbon-Nitrate |
| TiN | : | Titanium- Nitrate |
| Ti-Ni | : | Titanium-Nickel |
| Ti-Nb-Zr-Ta | : | Titanium-Niobium-Zirconium-Tantalum |
| Ti–6Al–4V | : | Titanium-6Aluminium-4Vanadium |
| $TiO_2$ | : | Titanium dioxide |
| WHO | : | World Health Organization |
| XPS | : | X-ray Photoelectron Spectrometry |
| XRD | : | X-ray diffraction |
| YSZ–Ag–Mo | : | Yttria-stabilized zirconia-Silver-Molybdenum |
| $\gamma_{SV}$ | : | Solid-vapor interface |
| $\gamma_{SL}$ | : | Solid-liquid interface |
| $\gamma_{LV}$ | : | Liquid-vapor interface |
| ZnO | : | Zinc oxide |
| Zr-Cu-Ag | : | Zirconium-Cuprum-Silver |
| Zr-Cu-Al | : | Zirconium-Cuprum-Aluminium |
| Zr-Cu-Al-Ag-N | : | Zirconium-Cuprum-Aluminium-Silver-Nitride |

# CHAPTER 1: INTRODUCTION

## 1.1 Background

Antibiotic resistance can be life-threatening to humans, mainly because bacteria have always adapted so well in order to survive antibiotic exposure. Prior studies have pointed out that in 2011, about 722,000 patients caught an infection while staying in acute care hospitals in the United States, 75,000 of which died as a result. Today, approximately 1 out of 25 patients is exposed to hospital-acquired infections (Lázár et al., 2013; Leslie et al., 2014; Spellberg et al., 2013)

Fewer bacterial infections evidently mean less antibiotic consumption, which would consequently depress antibiotic resistance. One viable means of preventing bacterial infections in the first place is to develop and engineer material surface coatings with antibacterial properties (Lemire et al., 2013; Page et al., 2009)

Modifying the surfaces of metallic biomaterials with functional properties has for centuries been recognized as a way to facilitate favorable biological responses, particularly for implant screws, surgical instruments and dental applications (Raza et al., 2016). Good biomaterials should be inert but strong enough to allow biomechanical loading, easy to handle, non-corrosive, non-toxic, non-allergenic, non-carcinogenic, easy to sterilize, inexpensive and resistant to infection.

Biomaterials can be classified into several categories, including metallic, ceramic, polymeric, composite and biodegradable polymeric biomaterials (Blackford et al., 2006; Kulinets, 2015; Mahapatro, 2015; Nasab & Hassan, 2010; Navarro et al., 2008; Parida et al.). Among these, metallic biomaterials are of particular interest. Common metallic biomaterials are stainless steel, titanium (Ti) alloy, cobalt-chromium (Co-Cr) alloy and titanium-nickel (Ti-Ni) alloy, which are applied in medical devices and surgical

instruments extensively. Stainless steel (SS), particularly SS 316L, has been of great relevance to surgical instruments owing to its high corrosion resistance, good strength, low cost, low carbon content (to resist sensitization) and good formability (Oshkour et al., 2015).

Although the desired properties of SS 316L for surgical instruments has already been proven, the antibacterial coatings can block the bacterial attachment on instrument's surface which very good to employ in healthcare and hygiene applications, (Park & Lakes, 2007). The biocompatible coatings can prevent the human cell death, disturb the normal body function and influence the proliferation cell (Liu et al., 2018b). The coated material for surgical instruments application required a properties that material compatible with the living tissue (Bekmurzayeva et al., 2018). The biocompatible surgical instruments are referred to its ability to forbid the conflict effect when it come in contact with the body cell. There are several examples of biocompatible surgical instruments which aid the positive surgery results; i)cutting tool does not support blood clotting when come in contact with bloodstream (Vanags et al., 2017), ii)suture that can promote tissue healing without trigger cellular dysfunction (Wang et al., 2017b) and iii)blade does not irritate the skin cell (Sankar et al., 2019).

The modified surgical instrument's surface with antibacterial and biocompatible coating is insufficient good without the satisfied SS 316L-coating adhesion strength. The high SS 316L-material coating bonding (adhesion strength) of surgical instruments can extend the coating's age which can maintain its functionalities. Thus, the combination characteristics of excellent antibacterial, biocompatible and adhesion strength coating is highly recommended to adapt with the surgical condition.

## 1.2 Problem Statement

The transmission of nosocomial infections, otherwise known as healthcare-associated infections (HAI), through healthcare facilities and products is among the most significant causes of complications and deaths resulting from infections (Dominguez-Wong et al., 2014; Otter et al., 2011). Antibiotic resistance is presently a great threat that is increasing year by year (Rizwan et al., 2018). According to the World Health Organization (WHO), 170,000 mortalities related to antibiotic-resistant bacteria have been recorded (Ventola, 2015). Every year almost 99,000 deaths in the US are associated with HAI (Weber et al., 2010). Moreover, the invasive methicillin-resistant *Staphylococcus aureus* (MRSA) infection has led to around 94,000 hospitalizations and 19,000 mortalities in the United States alone (Klevens et al., 2007). Cancer patients primarily in the intensive care unit (ICU) are susceptible to MDR-HAI (multidrug-resistant hospital-acquired infection), which also contributes to mortality. Common nosocomial infections can occur in the bloodstream, urinary tract or at the surgical site (Dasgupta et al., 2015).

A good example of MDR-HAI is the *Mycobacterium chimaera* infection after heart bypass surgery (Cornejo-Juárez et al., 2015; Sax et al., 2015). The surgical site is an easy, preferential target for bacteria to attack by colonization and biofilm formation due to the weakened immune system in the presence of foreign materials (Atefyekta et al., 2016). Surgical instruments/implants can carry such bacteria that cause infectious diseases (Yu et al., 2017b). Biofilms are difficult to remove and they form in response to bacteria being in stressful conditions. The best strategy is to prevent biofilms from forming at all (Rizwan et al., 2018). Biofilms exhibit a high tendency to resist antibiotic medication; hence, antibiotic treatment in dealing with biofilm formation is not an effective strategy (Spellberg & Gilbert, 2014; Yu et al., 2017b). Employing surfaces that

counteract the adherence and growth of bacteria is the best solution to avoid such infections (Campoccia et al., 2013). There is growing research interest in developing hygienic healthcare product surfaces to combat the transmission of infections. Such developments would help improve health, save lives and yield monetary benefits (Dominguez-Wong et al., 2014; Ge et al., 2017).

In addition to the proven durability of materials with antibacterial properties, the adhesion strength of SS 316L coatings has also been found to be effective. In surgical environments and sterilization processes, resistance against delamination and abrasion from daily stress and rough usage is a desirable specification of coatings. A poorly crystallized tantalum oxide (TaO) layer exhibits weak thin film-substrate interfacial bonding and conveys oxide defects. Furthermore, non-hardened coated films influence the release of the coating elements into the fluid system. Thus, excellent antibacterial properties are not the only key factor in preventing bacterial growth. Satisfactory adhesion strength also contributes to antibacterial coating life.

### 1.3 Research Objectives

- To develop single layer Silver Tantalum Oxide (Ag-$Ta_2O_5$) and multilayer Silver/Silver Tantalum Oxide (Ag/Ag-$Ta_2O_5$) thin films on 316 L Stainless steel (SS 316L) using Physical Vapor Deposition (PVD) reactive magnetron sputtering.
- To improve the adhesion strength and crystallinity of the as-deposited films by post annealing.
- To characterize the physicochemical properties (microstructure, elemental composition, hydrophobicity, micro mechanical, morphology, phase, structure, surface chemistry), antibacterial and biocompatibility performance of the deposited thin films.

## 1.4 Significant of studies

Over the past few decades, researchers have been seeking distinct types of antibacterial coatings to prevent MDR-HAI in patients. The problem is bacterial start growing during surgical procedure. When the duration of procedure is long for instance orthopedic or open heart surgery, the bacteria has enough time and environment to grow whereas further sanitization may not be possible. Surgical tools such as lamping, fixture, suture, scissor, blade with an effective durable antibacterial coating can reduce the risk of bacterial contamination and development.

In this study, a durable Ag/Ag-$Ta_2O_5$ nanocomposite thin film coating on Stainless steel was developed to address such a shortcoming. The as-deposited Ag/Ag-$Ta_2O_5$ nanocomposite film under study underwent thermal treatment to enhance the mechanical properties of the film. The modified thin film not only can avoid or limit bacterial adhesion on surgical instrument surfaces, but it was found that the superior adhesion strength of the treated film can reduce and slow down delamination during use in the rugged surgical environment. The behavior and interaction of such thin film coating is elucidated using *In-vivo* test of Bone Marrow cell and in presence of bacteria culture.

## 1.5 Scope of study

This research work focuses on optimizing the PVD magnetron sputtering parameters and annealing temperature to develop Ag-$Ta_2O_5$ and Ag/Ag-$Ta_2O_5$ film coatings on SS 316L substrate with superior adhesion strength. The proposed annealed samples serve to prove the enhancement in adhesion strength, antibacterial performance and biocompatibility properties.

## 1.6 Contribution to world of knowledge

A contribution of this research to the world of knowledge is the development of a new functional surface coating that may have important health, safety and economic consequences. Ag/Ag-$Ta_2O_5$ nanocomposite thin film was coated on surgical grade stainless steel 316L using PVD magnetron sputtering. Thermal treatment was applied to the thin film coatings by controlling the temperature to enhance the adhesion strength between the coating and stainless steel 316L. According to the micro scratch test results for the thin film coating adhesion strength, 3310±84 mN was achieved with the best experimental setup combination of magnetron sputtering and thermal treatment temperature. In addition, the optimized Ag/Ag-$Ta_2O_5$ nanocomposite thin film showed antibacterial activity against the pathogens *Escherichia coli* (ATCC 15597) and *Staphylococcus aureus* (NCTC 6571). The Ag/Ag-$Ta_2O_5$ thin film developed displayed good biocompatibility with human mesenchymal stromal cells. Therefore, these favorable mechanical and biological properties of Ag/Ag-$Ta_2O_5$ nanocomposite thin film make a large contribution to the area of medical applications for preventing infections, particularly regarding surgical instruments.

## 1.7 Outline of thesis

This thesis is written in five chapters. Chapter one presented the background of the study, problem statement, research objectives, research questions, significance of the study, scope of study and contributions to knowledge. Chapter two covers an introduction to biomaterials, SS 316L for surgical instruments and functional coatings for surgical tools as well as a literature review for the thin film deposition method of PVD magnetron sputtering. The second chapter also includes a literature review pertaining to antibacterial coating types, thin films for surgical instruments developed previously, silver nanoparticles and bulk particles, tantalum oxide, the thermal treatment

of Ag and TaO-based ceramic system, and antibacterial and biocompatibility tests. Chapters three and four present the methodology and results and a discussion involving different methods (A, B and C) of fabricating Ag-$Ta_2O_5$ thin film:

i. Method A: a combination of depositing a single-layer Ag-$Ta_2O_5$ thin film and annealing the as-deposited film at temperatures of 300, 400, 500 and 600 °C.

ii. Method B: a combination of depositing a multilayer Ag/Ag-$Ta_2O_5$ thin film and annealing the as-deposited film at 400 °C.

iii. Method C: a combination of depositing a multilayer Ag/Ag-$Ta_2O_5$ thin film and annealing the as-deposited film at 250, 400, 550, 700 and 850 °C.

Chapter five delivers the conclusions of the thesis and future work suggestions.

# CHAPTER 2: LITERATURE REVIEW

## 2.1 Introduction

Metallic materials have been used as biomaterials on a large scale for many decades. Unlike polymeric and ceramic materials, they have superior tensile strength, fatigue strength, and fracture toughness, which are paramount properties required in replacing structural human body components. Accordingly, metallic biomaterials are used in medical devices, such as artificial joints, bone plates, screws, intramedullary nails, spinal fixations and spacers, external fixators, pacemaker casings, artificial heart valves, wires, stents and dental implants. Type 316L stainless steels, cobalt-chromium alloys, commercially pure titanium and Ti6Al4V alloys are typical metallic biomaterials used in biomedical applications.

## 2.2 316 L Stainless steel for surgical instruments

316L surgical grade stainless steel (SS 316L) has been widely used in biomedical applications for many decades. SS 316L exists as a low-carbon version (0.03 %) compared to the 316 straight grade with 0.08 % maximum carbon content. Carbon is found to cause the formation of chromium carbides at the grain boundaries, leading to localized corrosion (Srinivasan et al., 2015). Thus, decreasing the carbon content boosts the corrosion resistance of stainless steel (Chen & Thouas, 2015). In addition, SS 316L displays excellent tensile strength of 400 MPa and hardness of 42 HRA on the Rockwell scale (Abenojar et al., 2002). According to Sumita et al. (2004), SS 316L is available commercially for implantable devices because SS 316L is 10-20 % cheaper than other metallic biomaterials.

Owing to its outstanding chemical composition, mechanical properties and monetary advantage, SS 316L was introduced for medical devices, orthopedic implants and

surgical instruments (De Las Heras et al., 2017; Plecko et al., 2012). Regarding surgical instrument applications, SS 316L is used extensively in manufacturing a variety of devices and tools, such as sutures, needles, catheters, plates and tooth fillings. Even though SS 316L exhibits properties favorable for surgical instrument applications, the unmodified instruments are unable to perform effectively. For instance, an uncoated SS 316L surgical tool poses high risk of variant Creutzfeldt-Jakob disease infection caused by tissue contamination during neurological surgery (Bruce et al., 2001). Hence, surface modification to achieve more desirable mechanical properties and biological responses is essential to assure the surgical instruments are safe, reliable and bio-friendly for human health. Researchers have discovered a new material by combining metals with ceramic (silver + Ta-based ceramic) that improves product functionality (Alias et al., 2018). Thus, the performance of SS 316L for surgical instrument applications is comprehensively studied and investigated in this research.

### 2.3 Functional coating for surgical instruments

Surgical site infections may develop when pathogens like *coagulase-negative staphylococci* and *Bacillus subtilis* attach onto the instruments during surgical procedures (Dancer et al., 2012). Approximately 724,000 surgical procedures are performed in the United States each year, with up to 1 % resulting in such infections (de Lissovoy et al., 2009). This figure is considered a catastrophe because contracted infections can lead to mortality and escalating care costs. Therefore, various potential surgical instrument coatings have been developed to combat infection issues. Polymer and nonmetal-based material coatings are employed in several surgery specialties. The metal composite-based coating technology has received exceptional attention for its potential to be conveyed to general surgical instruments.

### 2.3.1 Instruments coating for neurosurgery

A common instrument used in neurological surgery is the stainless steel forceps. This tool can easily be contaminated with microbes associated with prion protein in tissue. Because it is clearly so challenging to remove attached microbes, researchers have initiated a prevention step by depositing diamond-like carbon (DLC) on the surface of bare stainless steel. When such DLC-coated surgical instrument comes in contact with tissue, it has a good tendency to resist bacterial attachment. Besides, this coating is not easily damaged by rough use (Secker et al., 2012). Previous studies on coating forceps with Teflon (Ceviker et al., 1998) and Gold-1,1,2,2-tetrafluoroethylene (gold-PTFE) (Mikami et al., 2007) have indicated satisfactory hydrophobicity properties. The Teflon coating developed can avoid sticking to tissue during cauterization, while the metal-polymer Gold-1, 1, 2, 2-tetrafluoroethylene (gold-PTFE) coating helps repel protein.

### 2.3.2 Instruments coating for cardiovascular surgery

The most important instruments in cardiovascular surgery are clamps, cutting instruments, needle holders, retractors, forceps and guide wires. Hergenrother et al. (1995) discovered that photoactive polymer coating on a metallic guide wire exhibited hydrophilicity. This coating also demonstrated tight polymer-metal bond, and good lubricity and maneuverability.

### 2.3.3 Instruments coating for orthopedic surgery

Bone hooks, screws, plates, drill bits and tendon instruments are vital utensils in orthopedic surgery. The poor hemocompatibility properties of uncoated stainless-steel surgical instruments lead to adverse effects when uncoated stainless steel makes direct contact with patient blood. Hence, it is essential to modify the surfaces of these surgical instruments by adding materials to sustain rugged use and sterilization for better adhesion strength and hemocompatibility.

### 2.3.4 Instruments coating for dentistry surgery

Oral health practice often involves chisels, elevators, iris curved scissors and sutures. The life span of chisels can be extended by applying chromium oxide to the surface (Kumar et al., 2017a). Sutures are extremely valuable clinical kit components for dentists and are highly praised for easing surgical procedures. Layering ethylene propylene on sutures is promoted and according to research results this type of coating has lower surface roughness and improved suture performance (Pokropinski et al., 2000).

However, instruments coated with non-metal polymers are recognized as having poor thermal stability (Heim & Brassell, 2017). For example, blades coated with at least one polydiorganosiloxane or PTFE mix confer stickiness properties when introduced to elevated temperatures. Consequently, researchers have found new alternatives to attain better thermal stability, such as applying metals or metal-ceramic composites as coating materials.

### 2.3.5 Metal and metal-ceramic composite based surgical instruments coating

There are few scientific information sources about the shortcomings and impacts of surgical instrument coatings on human health. Nonetheless, Bruce et al. (2001) addressed this issue and found that SS 316L surgical blades coated with $TiO_2$ and TiN had poor bonding between the coating and substrate. The metal elements Cr, Fe and Ni leached into blood and body fluids, thus reducing the functional coating performance.

Previous investigations generally present several limitations when it comes to describing findings for coated surgical tools in terms of adhesion strength performance, cytotoxicity and antibacterial activity. In one study, Park et al. (2003) studied TiN-coated surgical instruments and found improvements in the cytocompatibility properties

through the in-vitro standard cytotoxicity test ISO10993-5. However, their article did not cover the antibacterial performance and adhesion strength evaluation results for TiN-coated surgical instruments, both of which are essential properties for excellent instrument performance. In fact, studies on TiAlN and TiCN coatings have demonstrated strong film-substrate bonding as well as biocompatibility with hog's kidney cell, which only highlights the void in research on TiN regarding antibacterial function (Hollstein & Louda, 1999). Other researchers have investigated a similar subject, but more specifically, zirconium nitride-coated surgical instruments. Although the modified instruments can attain satisfactory hardness and enhanced wear life, no antibacterial properties have been reported (Navarre & Steiman, 2002; Rhandhawa, 1991).

The PVD antibacterial Zr-Cu-Ag thin film coating introduced by Bouala et al. (2018) is not described much in terms of toxicity. The subject of toxicity to the human body is highly controversial due to concerns about Ag nanoparticles (AgNPs) being used in thin film. AgNPs exhibit cytotoxicity at higher concentrations primarily because of their small size and variable properties (Burd et al., 2007; Hussain et al., 2005).

### 2.4 Thin film deposition

Thin film deposition methods can be divided into two types: chemical vapor deposition (CVD) and physical vapor deposition (PVD). PVD has attracted extra attention for the great diversity of deposition techniques. For instance, several PVD coating techniques implemented in industry include vacuum thermal evaporation, electron beam heating, ion beam deposition and magnetron sputtering. Each process has unique, specific features designated to effectuate target applications.

### 2.4.1 Physical Vapor Deposition (PVD)

Physical vapor deposition (PVD) is primarily used to deposit thin layers of material within a certain size range from nanometers to micrometers (Huff & Sunal, 2015; Mazzi et al., 2016; Qi et al., 2016). PVD is used extensively for industrial applications, such as microelectronic devices, cell electrodes, optical instruments, conductive coatings and surface modifications (Dixit et al., 2016; Elahi & Ghoranneviss, 2016; Pozio et al., 2016; Raniero et al., 2016; Zhang et al., 2017a). Three main concepts involved in this process are vaporization, transportation and condensation. High-temperature plasma vaporizes the target material, after which the vapor is transported in vacuum condition to the substrate surface (Gassner et al., 2016). The most common PVD types are thermal evaporation, ion beam sputtering and magnetron sputtering (Alishahi et al., 2016; ke et al., 2016; Mahan, 2000). In the present investigation, the magnetron sputtering technique is chosen and discussed in detail.

### 2.4.2 PVD magnetron sputtering

A wide range of industrial coating technologies are available. The preferred technique is physical vapor deposition (PVD) magnetron sputtering because it assists with attaining good coating performance. Magnetron sputtering offers unique advantages through the ability to operate at low temperatures and high material deposition rate(Reddy & Udayashankar, 2016; Zhang et al., 2017b).

PVD is one of the most favorable techniques for producing uniform coating thicknesses on flat substrates, homogenous coatings and most importantly, high-adhesion coatings (Li et al., 2017; Mohseni et al., 2014; Popa et al., 2015). The three main PVD process steps are vaporization, transportation and condensation (Gassner et al., 2016). Evaporation and magnetron sputtering are the most popular PVD forms.

Magnetron sputtering is appropriate for depositing a wide range of thin films (Aijaz et al., 2016; Raj et al., 2014; Wang et al., 2014) . With this method, deposition entails expelling the material (target) onto the substrate in vacuum condition. This process is associated with a carrier gas in the plasma chamber, such as argon, neon, krypton or xenon (Gu et al., 2014; Mohseni et al., 2014). The schematic diagram in Figure 2.1 shows the mechanism of PVD magnetron sputtering. The strong magnet across the target creates a magnetic field. When direct current (DC) or radio frequency (RF) power is applied, the gas becomes ionized and plasma forms in front of the target. In the plasma, free electrons hit the gas atoms, thus producing positively charged gas atoms and secondary electrons as well. These positively charged atoms accelerate towards the negatively charged target material, bombarding and then expelling the target. The ejected atoms condense onto the substrate surface, ultimately forming a thin film (Velasco et al., 2016).

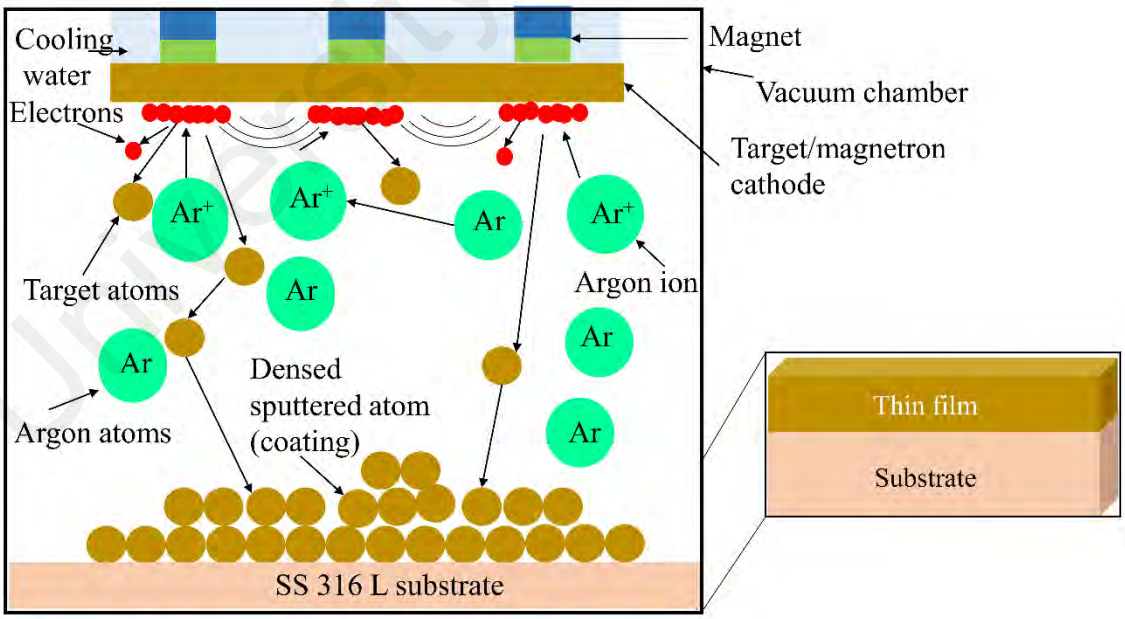


Figure 2.1: Schematic diagram of magnetron sputtering

According to the literature, a number of researchers have developed functional coatings via PVD magnetron sputtering (Chang et al., 2014; Huang et al., 2014; Lee et al., 2013a; Rahmati et al., 2015b; Siegel et al., 2015; Zhao et al., 2007). The sputtering conditions that receive the greatest attention include sputtering pressure, DC/RF sputtering power, gas flow rate, and substrate temperature. Results from literature have shown that different magnetron sputtering conditions produce varying surface morphologies and mechanical properties.

In magnetron sputtering, the deposition power has a central role in plasma formation as it determines the target ion bombardment (Peng et al., 2016). A number of researchers have studied the deposition of Ta/$Ta_2O_5$ multilayer coating on Ti substrate using 200 W (Ta) and 100 W ($Ta_2O_5$) DC power (Chang et al., 2014; Huang et al., 2014). Findings indicate that the deposited coatings showed a crystalline phase of the Ta layer and an amorphous phase of nanostructured $Ta_2O_5$ film. In preceeding published work, Gnanarajan et al. (2007) reported that the crystallized $Ta_2O$ phase can be obtained at higher substrate temperature and through post thermal treatment, which is explained further in the next section. Low deposition temperature cannot provide sufficient energy to stack the TaO atoms in solid form. A similar result was obtained by Rahmati et al. (2015b). An amorphous TaO coating was achieved by using 200 W DC power, leading to low adhesion strength between the TaO and Ti6Al4V. Furthermore, the 100-200 W deposition power range has a good tendency to produce small deposited particle size with low surface roughness. Yet with increasing sputtering power, the deposited particle size and surface roughness increase according to Wang et al. (2017a). However, the deposition of molybdenum coating carried out by Dai et al. (2014) at 100-250 W power suggests that a much more compact and smooth surface can be achieved at higher sputtering power (200-250 W). Zhao et al. (2007) revealed that the coating surface

roughness is relative to the arrangement of the structural film stacks. The Ag/$Ta_2O5$ structure resulted in lower surface roughness than $Ta_2O_5$/Ag/$Ta_2O_5$. Increasing the target material power exhibited a substantially better chance of depositing a larger amount of material. A study by Huang et al. (2014) showed that $Ta_2O_5$/Ag coating containing 23.3 atomic percentage of Ag deposited at 40 W DC power yielded a bigger contact angle than the sample deposited at 20 W DC. The greater contact angle attained due to the higher Ag content that exhibits hydrophobicity is a favorable characteristic for related biomedical applications.

Oxygen flow rate also has an important effect on the formation of tantalum oxide in magnetron sputtering. According to Achache et al. (2018) study, the addition of oxygen during sputtering has a strong influence on the microstructure, texture and mechanical properties of quaternary TiNbZrTa coating. Raising the oxygen flow rate from 0 to 10 standard cubic centimeters per minute (sccm) reduced the crystallite size by about 83 %. This grain refinement resulted from compressive stress and led to an increase in hardness.

Another vital parameter in magnetron sputtering is the substrate temperature, which alters the mechanical properties of the coating. A recent investigation carried out by Gleich et al. (2018) proved that raising the substrate temperature resulted in very good hardness and Young's modulus of molybdenum-boron-carbon ($Mo_2BC$) film. The substrate temperature can also influence the crystallinity and surface roughness. Increasing the substrate temperature from RT to 200 °C generated better crystallinity but a rougher ZnO film.

Sputtering pressure of Ar gas can meaningfully affect the surface characteristics of coated materials. The contact angle and surface roughness of diamond-like carbon

coating deposited at various pressure values had a nonlinear relationship. In an early stage when the sputtering pressure was increased from 0.2 to 1.0 Pa, the contact angle decreased. However, beyond 1.0 Pa, the contact angle increased. When the sputtering pressure was increased from 0.2 to 1.0 Pa, the surface roughness value gradually increased and once the sputtering pressure reached 1.4 Pa, the surface roughness slightly decreased (Liu et al., 2018a). found that raising the sputtering pressure (0.4–0.8 Pa) decreased the surface roughness of coated $Ta_2O_5$. According to Stan et al. (2013) work, increasing the sputtering pressure (0.2-0.4 Pa) decreased the coating thickness gradually.

Generally speaking, the sputtering conditions have a strong relationship with the coating crystallinity, particle size, surface roughness, elemental composition, hardness, wettability and thickness. The literature contains an insufficient number of studies on the effect of magnetron sputtering conditions on the adhesion strength of TaOAg coating with antibacterial performance.

### 2.4.3 Ag and Ta-O based thin film of deposited by PVD magnetron sputtering

The literature indicates that a variety of thin films have been developed by magnetron sputtering for medical device applications as listed in Table 2.1. However, a large number of thin films such as tantalum (Ta), tantalum oxide (TaO and $Ta_2O_5$), silver nanoparticle-hydroxyapatite (AgNPs-HA), titanium-silver (TiAg) and zirconium-cuprum-silver (ZrCuAg) have been considered for implantation purposes. Although this class of functional thin films has satisfactory mechanical properties, antibacterial performance and proliferation cell activity, available research on Ag and TaO coated surgical instruments is still in emergent stages.

Table 2.1: Ag and Ta-O based thin film of deposited by PVD magnetron sputtering

| Coated material/ substrate | Application | Mechanical and/ or biological properties | References |
|---|---|---|---|
| Ta-O/ Ti | Orthopedic & dental | The as-deposited Ta-O exhibit good antibacterial performances & cytocompatibility | (Chang et al., 2014) |
| $Ta_2O_5$-Ag/ SS 304 | Biomedical materials & devices | $Ta_2O_5$ and $Ta_2O_5$-Ag coatings with 12.5 at. % of Ag has improved antibacterial effects & cytocompatibility | (Huang et al., 2014) |
| Ta-O/ Ti–6Al–4V | Implant applications | The adhesion strength of annealed Ta-O film increased | (Rahmati et al., 2015a) |
| $Ta_2O_5$/ ZK60 | Orthopedic implants | The $Ta_2O_5$ layer enhanced the corrosion resistance of ZK60 | (Jin et al., 2017) |
| Ta/ SS 316L | Implant | Ta and TaO coatings were non-cytotoxic | (Moreira et al., 2017) |
| Ta Ti–6Al–4V | Biomedical | Ta films improved the corrosion resistance and adhesion strength of SS 316L | (Hee et al., 2016) |
| AgNPs-HA/ Ti | Medical implants | AgNPs-HA coating exhibited better nanohardness and elastic modulus | (Ivanova et al., 2016) |
| Ti-Ag/ Ti | Orthopedic & dental implant | Ti-Ag film showed a very good antibacterial effect & enhanced osteoblast functions. | (Bai et al., 2015) |

Table 2.1 continued: Ag and Ta-O based thin film of deposited by PVD

| | | | |
|---|---|---|---|
| Zr-Cu-Ag/ Si | Implants & surgical instruments | Durable & has bioactivity effect at 11 at.% of Ag content. | (Bouala et al., 2018) |
| Zr-Cu-Al-Ag-N/ Bulk metallic glass (BMG) | Biomedical | Excellent nanohardness and elastic modulus & superior antimicrobial properties with minor Ag content | (Lee et al., 2017) |
| Ti-Ag-N/Ag/ Ti6Al4V | Implant | Antimicrobial activity & biocompatibility properties | (Yu et al., 2017a) |
| Ag-Au/PTFE/ Si | Medical polymer device | Extreme antibacterial effect | (Zaporojtchenko et al., 2006) |
| Ag/ Polyimide | Medical tool | Ag demonstrated a good antibacterial effect | Siegel et al. (2011) |
| Ti-Ag and Nb-Ag/ Si | Bone implant & dental device | Superior antibacterial performance | (Wojcieszak et al., 2016) |
| Ag-HA/ Ti | Implant | Ag-HA layer has shown good antibacterial effect | (Chen et al., 2006) |
| Ag doped $TiO_2$/ SS | Implant | Lower Ag ion released showed good antimicrobial activity & non-cytotoxicity | (Jamuna-Thevi et al., 2011) |
| Ag-HA/ Ti | Implant | HA coating enhanceded adaptation & proliferation cells | (Surmeneva et al., 2017) |

Table 2.1 continued: Ag and Ta-O based thin film of deposited by PVD

| | | | |
|---|---|---|---|
| Zr-Cu-Ag/ Metallic glass | Dental & orthopaedic implant | Zr-Cu-Ag has strong biocide effect | (Etiemble et al., 2016) |

## 2.5 Types of antibacterial coating

Antibacterial coatings have a tendency to be therapeutic at specific sites and are thus more efficient at inhibiting biofilm development than oral administration, which is leads more to side effects and toxicity (Kumar & Madhumathi, 2016). There are three primary types of antibacterial coatings: i) antiadhesive, ii) contact killing, and iii) antibacterial agent release coatings (Cloutier et al., 2015). For bacteria to grow, they need to adhere to the implant surface. Although polymer brushes are the most efficient against bacterial adhesion, total inhibition of adhesion is still not possible. Bacteria that evade brushing get the chance to adhere and develop biofilms on the implant surface (Nejadnik et al., 2008). With the contact killing method, antimicrobial compounds attract and kill bacteria upon contact (Alvarez-Lorenzo et al., 2016). These compounds, for instance antimicrobial peptides, attach to the implant surface through covalent bonding and kill bacteria by disrupting the microbial membrane (Coad et al., 2016). The effectiveness of the membrane disruption mechanism has been challenged and is still controversial. It has been suggested that membrane disruption is a temporary effect rather than a permanent solution (Salwiczek et al., 2014). Moreover, the ability to kill only those microbes that come in direct contact limits the compounds' effectiveness (Jain et al., 2016). Out of these three techniques, antimicrobial agent release has drawn the most attention. The antimicrobial agent release technique not only eliminates microorganisms directly attached to surgical instrument surfaces but can also attack other unwanted pathogens nearby (Swartjes et al., 2015). Amongst the antibacterial

coatings established, the silver and tantalum oxide types will be discussed further in the next section regarding surgical instrument applications.

### 2.6 Silver nanoparticle (AgNPs) and Silver bulk particle (Ag)

Silver nanoparticles (AgNPs) refer to particles smaller than 100 nm in at least one dimension. These nanoparticles have the potential to serve as an antibacterial agent and are widely used for biomedical purposes involving devices, clinical applications, pharmaceutical products, etc. (Franci et al., 2015; Tran et al., 2015). Due to the antibacterial character of AgNPs, they have shown interesting antibacterial activities against many pathogens, such as *S. sanguinis, L. salivarius, Escherichia coli, Pseudomonas aeruginosa* and *Staphylococcus aureus* (Guzman et al., 2012; Pal et al., 2007; Shahverdi et al., 2007). AgNPs possess a unique set of chemical and/or physical properties due to the small size (Soenen et al., 2015). In fact, the nanosize proportions facilitate greater bacteria killing effectiveness and slowed nucleus growth (Hajipour et al., 2012). Ivanova et al. (2015), embedded AgNPs in HA coating and observed antibacterial effects without cytotoxicity if appropriate AgNPs content was used. Huang et al. (2014) discovered that 12.5 % AgNPs in Ag-$Ta_2O_5$ coating is the maximum limit to achieve effective antibacterial behavior without causing cytotoxicity. Yu et al. (2017a) attained enhanced cytocompatibility by controlling the Ag content in TiAgN/Ag multilayer coating. Therefore, it can be concluded that a controlled dosage of AgNPs ensures the right bactericidal effect without causing toxicity. However, in a very recent study by Shevtsov et al. (2018) AgNPs were found to be totally cytocompatible with a variety of cell types. Furthermore, Liao et al. (2010) showed that AgNPs did not exhibit any cytotoxicity during testing of human gingival fibroblasts. Physiochemical aspects, such as particle size, degradability and agglomeration have a central role in cell viability (Gliga et al., 2014; Lankoff et al., 2012). Moreover, the effectiveness of AgNP

toxicity is determined by size, contact duration and environmental aspects (Akter et al., 2017).

Silver has been recognized for its strong antibacterial behavior for centuries and therefore used in various medicinal forms to treat infections and burns (Rai et al., 2009). Using Ag in biomedical applications is usually considered safe unless open wounds are exposed to a very high content of Ag, which may lead to argyria (Leaper, 2006). Bosetti et al. (2002) studied the *in vitro* behavior of Ag on fibroblasts (NIH 3T3) and osteoblast-like cells and found it to be absolutely cytocompatible. Recently, Shevtsov et al. (2018) confirmed the non-cytotoxic and antibacterial behavior of an Ag layer through an *in vitro* study of MG-63 cells, mesenchymal stem cells (MSCs) and bacterial growth. Furthermore, an *in vivo* analysis was also carried out for 6 months on a model of above-knee amputation in rabbits with no complications observed during the postoperative period (Shevtsov et al., 2018).

### 2.7 Tantalum oxide (TaO)

Different modification techniques facilitate different chemical bonding structures and functional properties of TaO. For one, a thin layer of TaO forms naturally on tantalum metal surfaces in air. The reaction between tantalum (Ta) and oxygen ($O_2$) forms a stable oxide part called tantalum oxide (TaO, $Ta_2O_5$). Nevertheless, the biological function of TaO films has not been researched frequently.

Recent studies have shown that TaO exhibits excellent durability, hardness, strength, and corrosion resistance. Besides, TaO has good biocompatibility properties, making it a viable candidate for material coatings on clinical instruments (Bah et al., 2016; Hee et al., 2016; Jin et al., 2017; Köse & Kacar, 2016).

Tantalum oxide coatings exist in amorphous and crystalline phases (Chang et al., 2014; Mungchamnankit et al., 2016). Both amorphous and hydrophilic crystalline $Ta_2O_5$ coatings are good antibacterial agents (Chang et al., 2014). From the two, crystalline $Ta_2O_5$ showed good cellular biocompatibility with human skin fibroblasts (Chang et al., 2014).

TaO is an emerging biomaterial due to its extraordinary blood compatibility, good cytocompatibility and antibacterial response (Chang et al., 2014). The wide band gap of TaO is primarily responsible for its excellent antithrombotic performance (high resistance against blood clotting), hence rendering it a strong candidate as a coating material on SS 316L and Ti-based blood-contacting devices (e.g. stents) (Leng et al., 2006). The antithrombotic nature and cytocompatibility of TaO films has been confirmed by researchers through *in vitro* analyses of human skin fibroblast cells (CCD-966SK) and human umbilical vein endothelial cells (HUVEC) (Huang et al., 2014; Leng et al., 2006).

Although both Ag and TaO display excellent biological performance, which is required for surgical tool applications, the mechanical aspect needs serious attention. It is known that surgical instruments must be hard enough to take and hold a cutting edge, for example scissors. Poor coating quality or low coated material crystallinity have been found to affect surgical instrument life.

## 2.8 Thermal treatment of Ag and TaO-based ceramic system

Since adhesion is a vital factor in evaluating the performance and durability of coatings, the post annealing treatment seems to be a good solution (Zhang et al., 2018). This treatment is credited for being the most desirable treatment technique because it is

inexpensive, easy to incorporate into a process device and yields better mechanical properties and microstructural stability.

According to literature, several annealing experiments have been conducted to study the influence of thermal treatment on the behavior and morphology of coatings (Lopes et al., 2015; Siegel et al., 2015; Velasco et al., 2016). This essential process, thermal treatment, under certain conditions can help the metal/ceramic coating material attain well-structured of nanocrystal (Tong et al., 2015), improved adhesion strength (Boi et al., 2015; Fang et al., 2014; Sidane et al., 2015) and a crystalline structure (Chou & Hsu, 2016; Dualeh et al., 2014; Hu et al., 2014; Tang et al., 2017; Zhao et al., 2016).

Low temperatures and low-energy ion bombardment are generally utilized in the sputtering process, which allow limited growth of the film morphology and microstructure. Outcomes such as the attachment of impurities, small particle size and formation of lattice point defects influence the metastable phase of the film. According to earlier work, annealing is one of the simplest treatment methods used to improve film phase stability. The recovery effect associated with the annealing process generates the migration, recombination and eradication of point defects, rearrangement and annihilation of dislocations, and growth (Lopes et al., 2015).

Several published works reported annealing Ag or TaO-based films under various conditions for biomedical applications. A range of annealing temperatures and various conditions have often been employed to improve as-deposited film performance. In a study of as-deposited AgNPs annealed at 250 °C for 15 minutes in air and Ar ambient, Otieno et al. (2016) demonstrated the significant AgNP size enhancement, increased surface roughness and reconstructed shape. This is consistent with the results reported

by Siegel et al. (2015). Using the same temperature and annealing the AgNP nanolayer in air for 1 hour showed a transformation of the AgNP structure into larger spherical-shaped particles. The individual larger and spherical particles together provided a greater surface area for the annealed Ag film, which presented a stronger antibacterial effect against the *E. coli* and *S. epidermidis* pathogens.

In Lopes et al. (2015) work, $TiAg_x$ thin film annealed at 500 °C in vacuum condition for one hour encouraged good stability of the TiAg intermetallic phase with higher crystallinity, better mechanical properties and grain refinement (Lopes et al., 2015). The results from Rahmati et al. (2015b) study indicate that the adhesion strength of the coated film to the substrate is directly proportional to the annealing temperature according to a micro-scratch testing evaluation. The adhesion strength of as-deposited TaO film improved by about 63 % after annealing at 500 °C in air for 1 hour. The reaction between TaO film and air during annealing influences stable $Ta_2O_5$ formation. A recent study by Perez et al. (2018) of TaO pointed out that annealing at 1000 °C is the optimal condition to produce $Ta_2O_5$. Lee et al. (2013a) reported that the annealing of as-deposited Ag-$Ta_2O_5$ nanocomposite at 700 °C in atmosphere for 1 hour facilitates the formation of Ag nanoparticles.

Tantalum oxide crystallization can be achieve above 600 °C, or more specifically at 700 °C. The formation of crystallized $Ta_2O_5$ has been reported elsewhere (Donaldson et al., 2016; Gnanarajan & Lam, 2008; Huang et al., 2014; Mungchamnankit et al., 2016; Zhabrev et al., 2004). Annealing amorphous Ag-$Ta_2O_5$ at 700 °C for 30 s with a rapid thermal annealing system keeps the AgNPs at the surface. Nano-crystallized Ag-$Ta_2O_5$ film with 12.5 % Ag has good antimicrobial activity against *S. Aureus* and is biocompatible with skin fibroblast cells. However, the biocompatibility decreases if

double the amount of Ag is added to the Ag-$Ta_2O_5$ film due to the higher AgNPs fraction (Huang et al., 2014).

Furthermore, annealing at 700 °C enhances the crystallinity of $Ta_2O_5$, as reported by Mungchamnankit et al. (2016). In their study, the crystallized $Ta_2O_5$ showed greater surface roughness but no antibacterial effect. The *S. Aureus* colonies survived neither on amorphous nor crystallized $Ta_2O_5$ surface film.

In Chang et al. (2014) study, rapid annealing of as-deposited $Ta_2O_5$ at 700 °C in air for 1 hour stimulated the crystallization of β-$Ta_2O_5$ with lower hydrophobicity properties. The amorphous $Ta_2O_5$ exhibited good antimicrobial performance against *S. aureus* and *A. actinomycetemcomitans* and thus has potential for use in medical device applications for the purpose of decreasing the risk of infection. Hydrophilic β-$Ta_2O_5$ coatings encourage excellent viability of human skin fibroblast cells and can be used as a surface modification for Ti implant applications to increase biocompatibility. Thus, amorphous $Ta_2O_5$ evidently has potential to reduce infections, while crystallized β-$Ta_2O_5$ can increase biocompatibility, both of which are helpful for medical applications.

The annealing of Ta film at thermal oxidation with low pressure for 15 minutes shifts the amorphous phase into crystallized epitaxial $Ta_2O_5$ and $Ta_2O$ films. However, further annealing up to 1 hour transforms the film to the single $Ta_2O_5$ phase (Gnanarajan & Lam, 2008).

Amorphous TaO film was isothermally annealed by Donaldson et al. (2016). A series of metastable tetragonal tantalum dioxide ($TaO_2$) phases formed due to insufficient oxygen. However, Donaldson et al. (2016) observed that $Ta_2O_5$ was not produced at all when annealing at temperature and time ranges of 900-1100 °C and 1–100 h, respectively.

## 2.9 Ostwald Ripening

Ostwald ripening process of the nanocomposite film describes the growth of the unstable nano-size particle. Since the nano particles are more vigorously and not stable rather than the larger particle, the Ostwald ripening process occurs spontaneously. The numerous of Ostwald ripening studies concerning the evolution of the surface morphology when the annealing temperature was applied (Jiang et al., 2016; Kyaw et al., 2019). By referring to Figure 2.2, the annealing temperature influences the smaller particles to combine and contribute to a larger and stable form. As the kinetic energy per time or annealing temperature increases, the higher surface energy of nano-size particle will pursue its neighbours to aggregate progressively. As a result, the number of nano particles decrease while larger particles grow with time. The larger particles tend to exhibit more stable structure, crystal phase and enhanced mechanical properties.

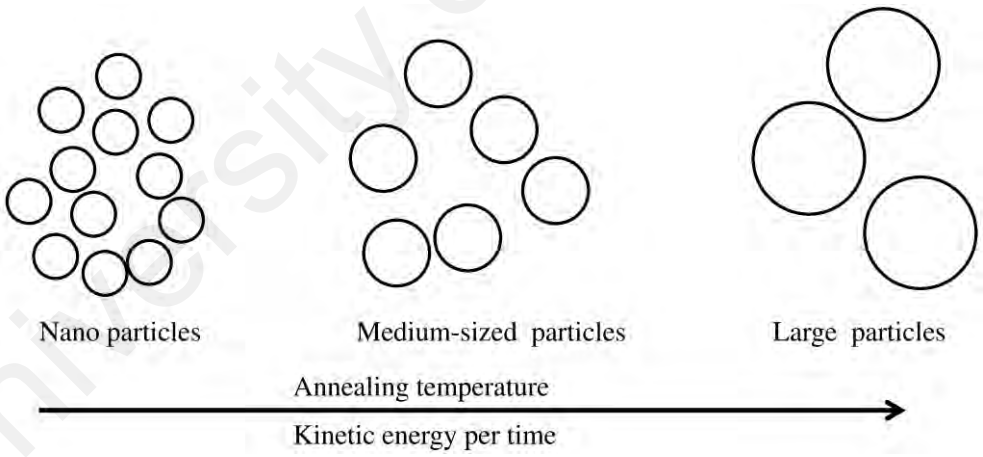


Figure 2.2: Ostwald Ripening process

## 2.10Antibacterial Test

There has been rising a number of research works aimed at developing antibacterial agents to solve the multidrug resistance issue (Xu et al., 2018). Therefore, with respect to the surgical field, it is compulsory to advance knowledge about screening for the performance of antibacterial coatings. Arias and Murray (2015) proposed that the

antimicrobial susceptibility test (or antibacterial test) developed in the 1940s seems to be a good platform to screen microorganisms for whether they are sensitive or resistant. Antibacterial testing is conducted to evaluate antimicrobial activity and encompasses a series of methods. Common laboratory methods developed previously are disk-diffusion (Chandrasekaran et al., 2018) well diffusion (Kaviyarasu et al., 2017), plug diffusion (Balouiri et al., 2016) and antimicrobial gradient (Salman et al., 2017). These *in vitro* antimicrobial activity methods require modest equipment and simple standardized techniques. The agar disk-diffusion method (Kirby-Bauer) has several advantages: it is economical, easy to interpret the results and can be used to test a large array of microorganisms and antibacterial agents (Köser et al., 2012). Zaporojtchenko et al. (2006) used *Staphylococcus epidermidis, Staphylococcus aureus*, *Enterococcus faecalis*, *Pseudomonas aeruginosa, Escherichia coli*, *Klebsiella pneumoniae* and *Candida albicans* as test microorganisms to evaluate the antibacterial potency of Ag/PTFE and Ag–Au/PTFE coated medical device. They found that their composite material is more susceptible to *Staphylococcus aureus,* which is the largest contributor to surgical site infections (Dolgin, 2010). In other study, AgNPs-HA exhibited good antibacterial activity against *Escherichia coli* and *Staphylococcus aureus* (Iconaru et al., 2014).

In the disk-diffusion procedure, an antibacterial agent and a bacteria test sample are diffused onto an agar plate. A good antibacterial agent will inhibit the growth of the test bacteria. The antibacterial activity (performance) of the agent is measured against the test bacteria according to the diameter of the inhibition zones surrounding the test sample**.**

### 2.11 Biocompatibility Test

Modifying surgical instrument surfaces by adding functional coatings has become increasingly common to improve instrument performance. Since an instrument may

react with living cells upon contact, the patient's safety should be emphasized. The surgical instrument must be compatible with the biological system, otherwise it attracts possible harm, such as inflammation, fibrosis, thrombosis or infection (Campa et al., 2018; Wen et al., 2018). Thus, surgical instruments must undergo a systematic measurement generally known as a biocompatibility test to meet the International Standard ISO 10993-1 requirement (Hou et al., 2017; Wettlaufer & Penn, 2018). Biocompatibility testing is intended to check how compatible an instrument is with an organ system and to determine the harmfulness of the instrument to body part functions.

Various biocompatibility test methods have been proposed since decades ago to assess the biocompatibility of medical devices in terms of cytotoxicity (tissue culture) (Nouri & Wen, 2015), sensitization assays (Kleinstreuer et al., 2018), irritation tests (Sugiyama et al., 2018), genotoxicity (Velickova & Milev, 2017), and hemocompatibility (Yilmaz et al., 2018). Among these, the cytotoxicity test is the most attractive means of evaluating the biocompatibility of medical instruments. It is used to measure cell viability in parallel with the release of toxic substances at different concentrations. Prior to the *in vivo* biocompatibility test, the cell culture is isolated from two types of groups: adherent and suspension cells (Lyness et al., 2018). Fibroblasts and mesenchymal cells from the adherent cell type group have been the center of attention in determining the biocompatibility of functional coatings (Chen et al., 2018; Meran et al., 2018; Surmeneva et al., 2015). Many studies have demonstrated that mesenchymal and fibroblast cells can be derived from bone marrow (Imamura et al., 2018; Jiang et al., 2002)

In earlier work, the attachment of MG-63 osteoblast cell (Maheshwari et al., 2014) and human mesenchymal stem cells (Lee et al., 2013b) has been observed through SEM micrograph. The appearance of the F-actin cytoskeleton on the tested zinc oxide surface

coating is a good sign of biocompatibility properties (Alves et al., 2018). This is further supported by the F-actin morphology organization by alloy steel-seeded human epithelial cell line after 72 h of interaction (Balas et al., 2018). The material surface properties, including chemical substance, surface charge, wettability and surface roughness influence the biocompatibility results (Chang & Wang, 2011). It is considered that a positive charge, hydrophobicity and rough surface indicate positive results (Xu & Siedlecki, 2007). Ponsonnet et al. (2003) found that cell proliferation is better at $60.4 \pm 5.8$ ° of contact angle while cell attachment is ideal under 1 µm surface roughness. Research by Mishra et al. (2017) demonstrated that osteoblasts proliferating on AgNPs cored in polyvinyl alcohol nanocapsules are superior to other test materials and are recommended for orthopedic applications.

### 2.11.1 Summary

This literature review highlighted that the SS 316L biomaterial boasts favorable chemical composition, low production cost and good strength, all of which are essential in related surgical instrument applications. Various surgical instrument coatings developed in the past exhibit desirable characteristics for surgical instrument performance. PVD magnetron sputtering with the multitude of advantages is utilized to develop antibacterial coatings containing for example Ag and $Ta_2O_5$. Ag, amorphous $Ta_2O_5$ and crystalline $Ta_2O_5$ exhibit good antibacterial responses, while crystalline $Ta_2O_5$ outperforms these in terms of cellular biocompatibility. It has been found that the post thermal treatment of Ag significantly changes the particle size, shape, surface roughness and phase. Thermal treatment at 700 °C crystallizes the $Ta_2O_5$ phase for better hydrophilic properties and greater compatibility with human skin cells. Earlier research works have also been conducted with cytotoxic testing to evaluate the harmfulness of medical devices to the living cell system. Not only is the compatibility

of instruments with living cells of great interest, but so is the sensitivity of microorganisms to devices/instruments. Antibacterial activity testing of coated medical devices is routinely carried out by disk-diffusion. To the date, there is no comprehensive work to address Ag-$Ta_2O_5$ nanocomposite on stainless steel as surface modification for surgical instruments application. Thus, this study is justified due to the insufficient research to date, particularly $AgTa_2O_5$ based films, to describe a physicochemical, biocompatibility and antibacterial properties.

# CHAPTER 3: METHODOLOGY

## 3.1 Introduction

This chapter introduces the three experimental methods used in this research to develop durable Ag-$Ta_2O_5$ thin film, namely Methods A, B and C. The material and substrate preparation, an overview of the experimental methods, PVD magnetron sputtering for thin film deposition, thermal treatment and characterization are also explained in this chapter. .

## 3.2 Materials and sample preparation

Commercial tantalum (Ta) and silver (Ag) 99.99 % pure targets produced by Kurt J. Lesker Company were used for deposition. The diameter and thickness of the targets were 101.6 and 3.1 mm, respectively. Stainless steel (SS 316L) sheets as substrates of 20 x 10 x 2 mm were ground with SiC paper (1500–2500 grit). Then the surfaces were polished to a mirror-like finish using 3 μm polycrystalline diamond suspension. The next step entailed washing the samples with distilled water and then air blow drying. The specimens were subsequently cleaned ultrasonically in acetone and then in ethanol for 10 minutes, after which they were dried again.

## 3.3 Overview of overall methodology

The overall Ag-$Ta_2O_5$ thin film development methodology comprising Methods A, B and C is summarized in the flowchart in Figure 3.1. After substrate (sample) preparation, the Ag-$Ta_2O_5$ thin film was deposited by PVD magnetron sputtering. With Method A, a single layer Ag-$Ta_2O_5$ thin film was deposited onto the sample called "$S_1$". With Method B, a multilayer Ag/Ag-$Ta_2O_5$ thin film was deposited onto four specimens called "S2", "S3", "S4", and "S5". Then with Method C, a multilayer Ag/Ag-$Ta_2O_5$ thin film was deposited on five samples, namely "$S_6$", "$S_7$", "$S_8$", "$S_9$" and "$S_{10}$". Methods B

and C involved different magnetron sputtering setups, which are presented in the next section (3.4). Afterward, thermal treatment was applied with each Method (A, B and C) for different conditions, as explained further in subsection 3.5.1. Next, physicochemical characterization of the microstructure, elemental structure, hydrophobicity, micro-mechanical properties, topography, phases and surface chemistry was carried out. The biological test results were also examined. Each method is explained in detail in the following section.

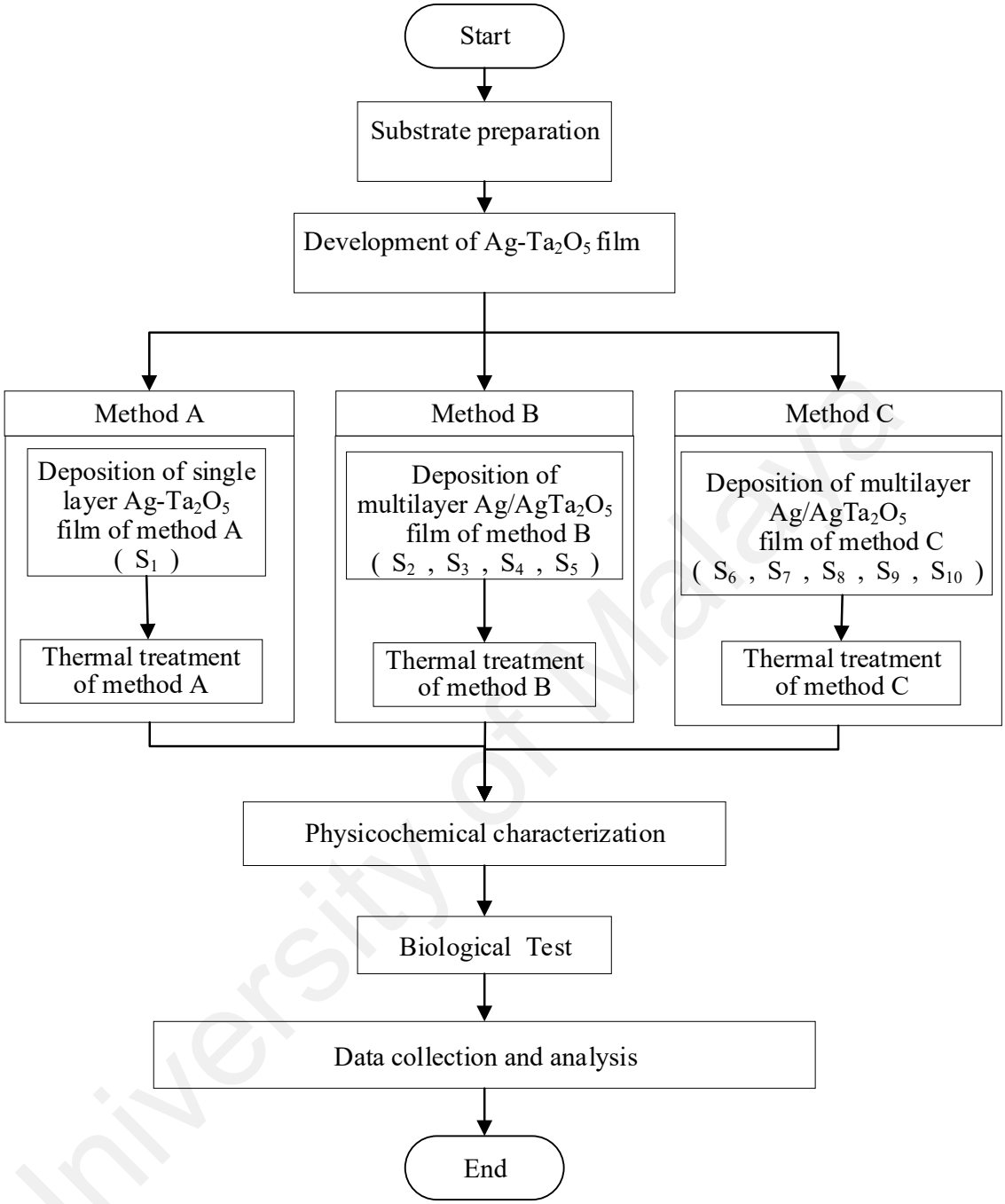


Figure 3.1: Flowchart of the overall methodology: Method A, B and C for developing Ag-$Ta_2O_5$ thin film

### 3.3.1 Experimental procedure of Method A

The procedure with Method A is illustrated in Figure 3.2. After the substrate preparation step, "$S_1$" was deposited with a single layer Ag-$Ta_2O_5$ thin film by PVD magnetron sputtering. A schematic of the single layer Ag-$Ta_2O_5$ thin film is shown in Figure 3.3. The as-deposited "$S_1$" was then annealed at a range temperature of 300 to 600 °C at 5 °C/min ramp rate. The microstructure, element, hydrophobicity, adhesion strength, micro hardness, topography and phase of the as-deposited "$S_1$" and all annealed "$S_1$" Ag-$Ta_2O_5$ thin film were characterized. The as-deposited "S1" and "$S_1$" annealed at 400 °C with the highest adhesion strength were kept on for structural analysis. Then the antibacterial performance of "$S_1$" annealed at 400 °C was determined . At the same time, "$S_1$" annealed at 500 °C, which had an $AgTaO_3$ phase available (found initially), was further investigated by changing the ramp rate to 2 °C/min. The microstructure, elemental structure, adhesion strength, hardness and phases of the new sample ("$S_1$" annealed at 500 °C and 2 °C/min) were characterized. Data collection and analysis were then executed for all samples.

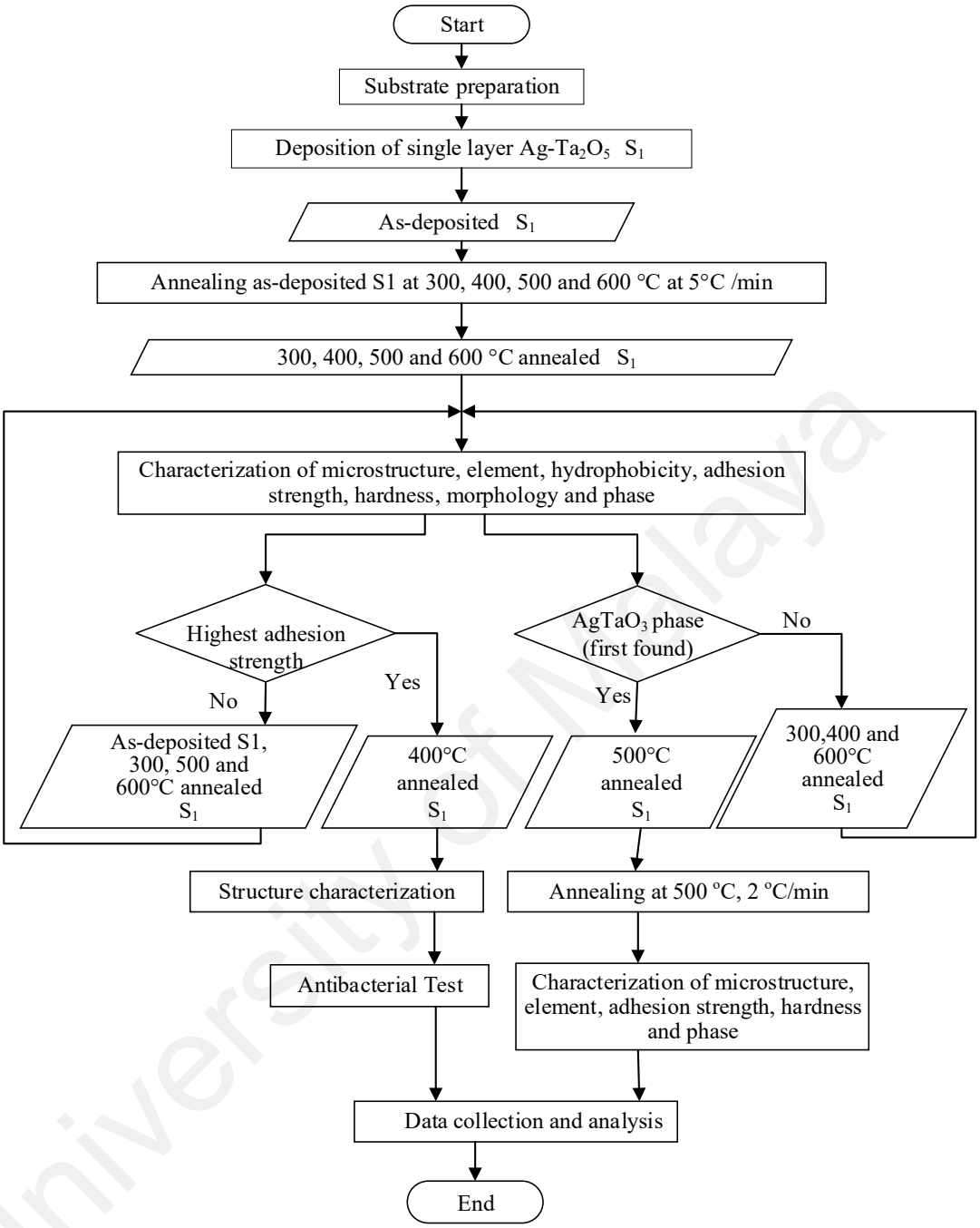


Figure 3.2: Flowchart of Method A for Ag-$Ta_2O_5$ thin film development

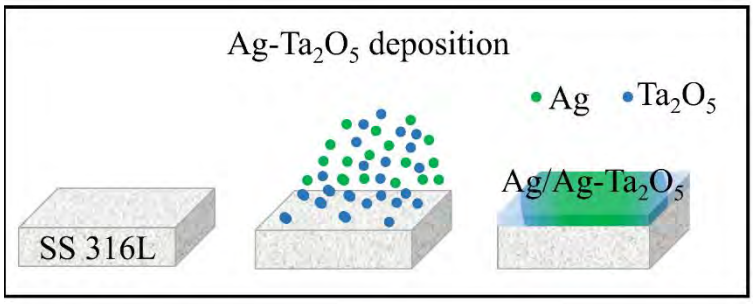


Figure 3.3: Schematic diagram of reactive magnetron sputtering deposition of single layer Ag-$Ta_2O_5$ thin film on SS 316L substrate

### 3.3.2 Experimental procedure of Method B

The procedure with Method B is illustrated in Figure 3.4. Following substrate preparation, "$S_2$" to "$S_5$" were deposited with multilayer Ag-$Ta_2O_5$ thin film method B by PVD magnetron sputtering. A schematic drawing of the multilayer Ag/Ag-$Ta_2O_5$ is displayed in Figure 3.5. The microstructure, elemental structure, hydrophobicity, adhesion strength, microhardness and phases of the as-deposited "$S_2$" to "$S_5$" were characterized. The as-deposited "$S_4$" was then annealed at 400 °C and 2 °C/min ramp rate because it had the highest adhesion strength amongst the as-deposited "$S_2$" to "$S_5$". Subsequently, the microstructure, elemental structure, hydrophobicity, adhesion strength, microhardness and phase characterization was repeated for the 400 °C annealed "$S_4$". Data collection and analysis were then done for all samples.

.

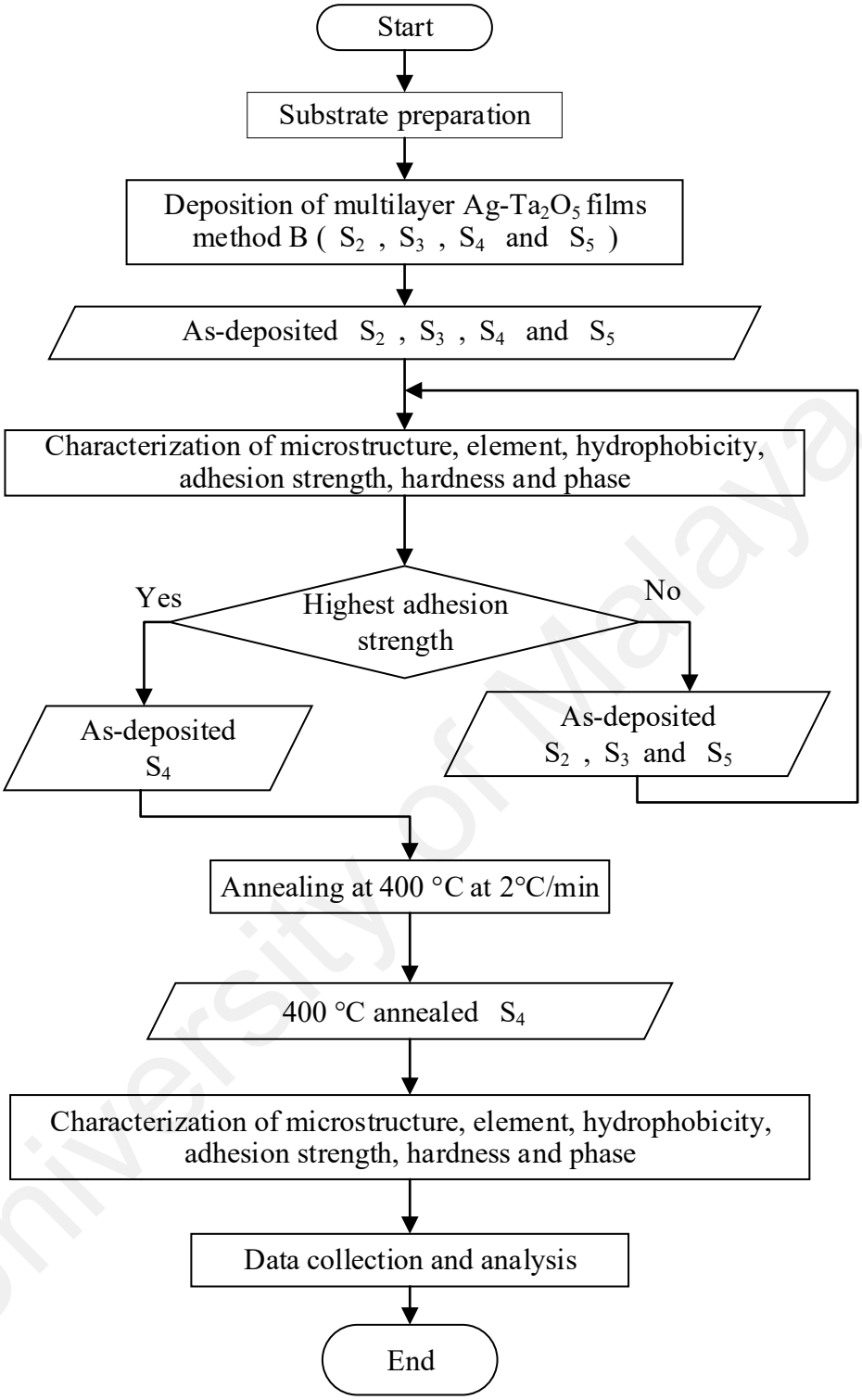


Figure 3.4: Flowchart of Method B for Ag/Ag-$Ta_2O_5$ thin film development

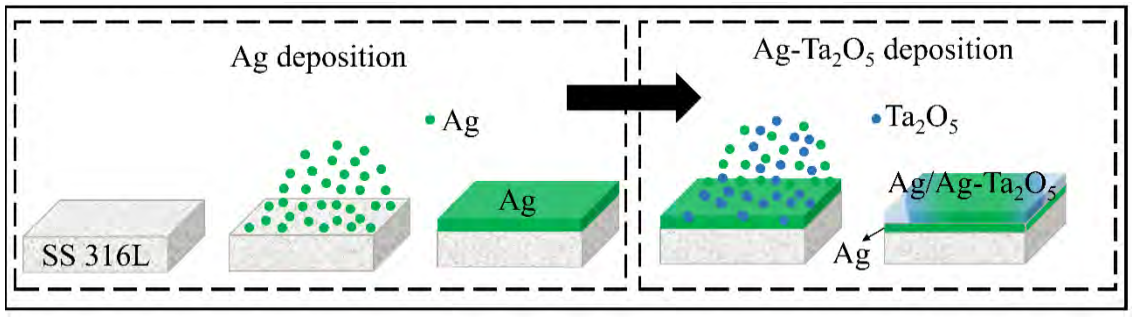


Figure 3.5: Schematic diagram of reactive magnetron sputtering deposition of multilayer Ag/Ag-$Ta_2O_5$ thin film on SS 316L substrate

### 3.3.3 Experimental procedure of method C

The procedure of Method C is illustrated in Figure 3.6. After the substrates were prepared, multilayer Ag-$Ta_2O_5$ thin films were deposited on "$S_6$" to "$S_{10}$" with Method C by PVD magnetron sputtering. The microstructure, hydrophobicity, adhesion strength and phases of as-deposited "$S_6$" to "$S_{10}$" were characterized. The as-deposited "$S_7$" was then annealed at temperatures ranging from 250 to 850 °C and 2 °C/min ramp rate because it had the highest adhesion strength amongst as-deposited "$S_6$" to "$S_{10}$". Subsequently, the as-deposited "$S_7$" and annealed "$S_7$" thin films were characterized for their microstructure, hydrophobicity, adhesion strength, phases and nanohardness. X-ray photoelectron spectroscopy (XPS) was also done to analyze the surface chemistry of as-deposited "$S_7$" and 400 °C annealed "$S_7$" (highest adhesion strength among annealed samples). Antibacterial and cytotoxicity tests were then carried out on the 400 and 700 °C annealed "$S_7$" samples (exhibiting comparable $AgTaO_3$) before data collection and analysis for all samples.

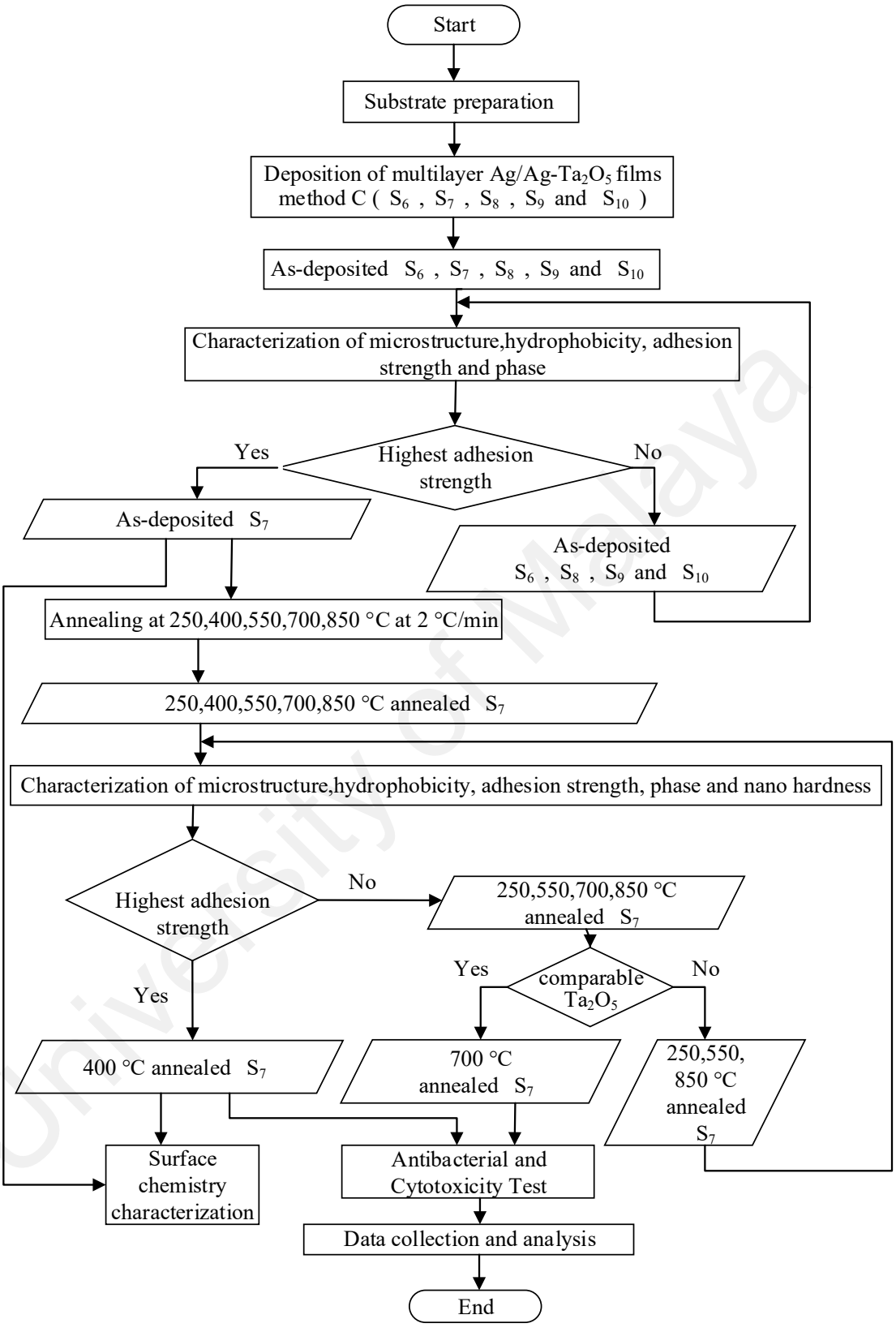


Figure 3.6: Flowchart of Method C for Ag/Ag-$Ta_2O_5$ thin film development

### 3.4 PVD magnetron sputtering experimental set up

A PVD (TF450 Sputtering System, SG Control Engineering Singapore) series magnetron sputtering system was utilized to deposit single layer Ag-$Ta_2O_5$ and multilayer Ag/Ag-$Ta_2O_5$ thin films. The prepared specimens were placed in the deposition chamber of the PVD magnetron sputtering system. The base pressure of the chamber was evacuated down to about 2.67 x $10^{-3}$ Pa. The surface of the target was pre-sputtered in Argon gas prior to deposition to reduce contamination in the vacuum chamber (Khaydukov et al., 2017). Oxygen ($O_2$) gas was introduced into the chamber to develop an Ag-containing ceramic layer on the substrate by reactive magnetron sputtering (Alias et al., 2018). The distance between the substrate and the targets was set at a constant 15 cm. Zero bias voltage was applied to the substrates. The Ta and Ag targets were energized with direct current (DC) and radio frequency (RF) power supply, respectively. The thin film deposition was carried out for 120 mins. For the multilayer Ag/Ag-$Ta_2O_5$ thin films, the Ag interlayer was deposited in the early stage for 20 mins, followed by Ag-$Ta_2O_5$. Once deposition was complete, the specimens were taken out and kept in a dry box for subsequent processing/characterization.

The magnetron sputtering setup for Methods A, B and C is summarized in Table 3.1. The table indicates that with Method A, a single layer of Ag-$Ta_2O_5$ was deposited on "$S_1$". With Method B, multilayer Ag/Ag-$Ta_2O_5$ was placed on "$S_2$" to "$S_5$". Each sample was deposited with a different magnetron sputtering setup (Table 3.1). The effect of the combination of power and argon flow rate on "$S_2$" and "$S_3$" was studied first, followed by the effect of the combination of argon flow rate and substrate temperature on "$S_4$" and "$S_5$". Method C involved depositing multilayer Ag/Ag-$Ta_2O_5$ on "$S_6$" to "$S_{10}$" by considering the power and substrate temperature variables (Table 3.1). The ratio of

Ar:$O_2$ is calculated in terms argon and oxygen flow rate and the measured working pressure is dependent on the argon feeding system.

Table 3.1: Experimental setup (deposition power, gas flow rate, substrate temperature) for Method A, B and C during deposition of single layer (SL) Ag-$Ta_2O_5$ thin film and multilayer (ML) Ag/Ag-$Ta_2O_5$ thin film, at $O_2$ flow rate of 6 sccm

<table>
<tr><th rowspan="2">Method</th><th rowspan="2">Layer</th><th rowspan="2">Sample</th><th colspan="5">PVD operating parameters</th></tr>
<tr><th>Power (W)</th><th>Ar flow rate (sccm)</th><th>Ratio Ar: $O_2$</th><th>Substrate temperature (°C)</th><th>Working Pressure (Pa)</th></tr>
<tr><td>A</td><td>SL</td><td>“$S_1$”</td><td>200</td><td>60</td><td>10.0:1</td><td>140</td><td>1.13</td></tr>
<tr><td rowspan="4">B</td><td rowspan="4">ML</td><td>“$S_2$”</td><td>200</td><td>60</td><td>10.0:1</td><td rowspan="2">140</td><td>1.13</td></tr>
<tr><td>“$S_3$”</td><td rowspan="3">300</td><td>30</td><td>5.0: 1</td><td>0.53</td></tr>
<tr><td>“$S_4$”</td><td>45</td><td>7.5: 1</td><td>250</td><td>0.83</td></tr>
<tr><td>“$S_5$”</td><td>60</td><td>10.0:1</td><td>280</td><td>1.13</td></tr>
<tr><td rowspan="5">C</td><td rowspan="5">ML</td><td>“$S_6$”</td><td>100</td><td rowspan="5">45</td><td rowspan="5">7.5: 1</td><td rowspan="3">250</td><td rowspan="5">0.83</td></tr>
<tr><td>“$S_7$”</td><td>200</td></tr>
<tr><td>“$S_8$”</td><td>300</td></tr>
<tr><td>“$S_9$”</td><td rowspan="2">200</td><td>150</td></tr>
<tr><td>“$S_{10}$”</td><td>Ambient</td></tr>
</table>

### 3.5 Thermal treatment condition of as-deposited thin film

As the thin film deposition by magnetron sputtering was completed, the thermal treatment (annealing) process was carried out with each method. The crystallization of the as-deposited samples morphology was stabilized in a tube furnace chamber (ELITE

Thermal Systems Limited, UK) to improve the adhesion strength between the thin film and SS 316L substrate.

Preliminary studies and published literature on magnetron sputtering deposition with respect to Ag and $Ta_2O_5$ coatings indicate that the coatings have relatively low adhesion strength, high surface roughness and low hydrophobicity properties, which are not applicable for biomedical applications (Chen et al., 2006; Meng & Sun, 2009; Rahmati et al., 2015a; Sarraf et al., 2017). In this study, a thermal treatment annealing process was carried out in atmospheric condition to compensate for such shortcoming. All samples were annealed for one hour and held at 200ºC for 15 mins to attain homogenization. Lastly, the samples were left in the furnace to cool down naturally to room temperature. The details of the thermal annealing conditions for each method are tabulated in Table 3.2. The treatment temperature profile for each method is illustrated in Figure 3.7.

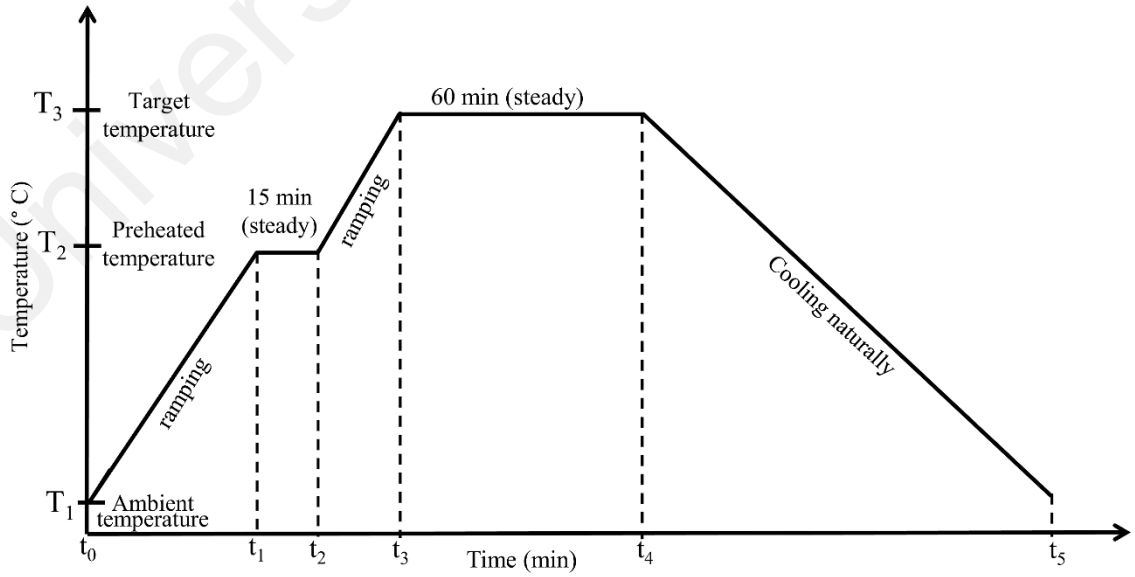


Figure 3.7: Temperature vs. time profile graph of the annealing process for the as-deposited Ag-$Ta_2O_5$ thin film

Table 3.2: Thermal treatment (annealing) parameters of as-deposited $S_1$, $S_4$ and $S_7$ with each Method. The annealing process started at $T_1$ = ambient (° C), $t_0$ = 0 min

| Method & Sample ID | Ramp Rate (°C/min) | Temperature (° C) | Time (min) Δt | | | | |
|---|---|---|---|---|---|---|---|
| | | $T_2$ | Heating | | | | Cooling |
| | | | $t_{(ramping)}$ $t_3$-$t_2$ | $t_{(steady)}$ $t_2$-$t_1$ | $t_{(ramping)}$ $t_3$-$t_2$ | $t_{(steady)}$ $t_4$-$t_3$ | $t_{(cooling)}$ $t_5$-$t_4$ |
| A & "$S_1$" | 5 | 300 | 40 | 55 | 75 | 135 | 175 |
| | | 400 | 40 | 55 | 95 | 155 | 209 |
| | | 500 | 40 | 55 | 115 | 175 | 244 |
| | | 600 | 40 | 55 | 135 | 195 | 278 |
| | 2 | 500 | 100 | 115 | 165 | 225 | 294 |
| B & "$S_4$" | 2 | 400 | 100 | 115 | 215 | 275 | 329 |
| C & "$S_7$" | 2 | 250 | 100 | 115 | 140 | 200 | 233 |
| | | 400 | 100 | 115 | 215 | 275 | 329 |
| | | 550 | 100 | 115 | 290 | 380 | 459 |
| | | 700 | 100 | 115 | 365 | 425 | 522 |
| | | 850 | 100 | 115 | 440 | 500 | 619 |

### 3.6 Characterization

The physicochemical properties (microstructure, elemental composition, hydrophobicity, micro mechanical, topography, phase, crystal structure analysis, and surface chemistry) were characterize by using Field emission scanning electron microscopy (FESEM), Energy dispersive x-ray spectrometry (EDX), Video-based

optical contact angle measuring system, Atomic force microscopic (AFM), X-ray diffraction (XRD), Micro-scratch, Microhardness, Field emission scanning electron microscopy-Focus ion beam (FESEM-FIB), Transmission electron microscopic (TEM), Nano-indenter, and X-ray Photoelectron Spectrometry (XPS).

### 3.6.1 Microstructure and elemental analysis

The microstructural characterization of the developed layers was carried out using FESEM (FEI-QUANTA FEG 650, US & Auriga, ZEISS, Germany) with an acceleration voltage of 1-5 kV. To view the cross-sectional images, the specimens was grinded on edge when holding the sample vertical. When the thickness was measured by SEM, three readings of the cross sections of the specimens were taken into account. The chemical element concentration was determined using FESEM equipped with EDX.

### 3.6.2 Hydrophobicity

The hydrophobicity (surface wettability) of Ag-$Ta_2O_5$ film was examined by measuring the contact angle with a sessile drop of distilled water using a video-based optical contact angle measuring system (OCA 15EC; DataPhysics Instruments GmbH; Germany). The liquid volume and dropping velocity were fixed at 3 µl and 2 µl.s−1, respectively. For surgical tool applications, hydrophobicity is considered a favorable criterion. A water-repellant coating surface can prevent blood, lipids and other liquids from adhering to surgical instruments. This provides surgeons better visibility, prevents excessive patient blood loss, can keep instruments cleaner and prolong their life, and most importantly, it can prevent bacterial attachment (Wendlandt et al., 2016). On the contrary, a hydrophilic surface that forms a low contact angle can be an ideal place for bacteria to grow due to the adherence of fluids. The physical surface features and the surface energy can be specified by the wettability and contact angle of a liquid with the

surface. The contact angle equilibrium of a droplet on a flat surface, $\theta_0$, is given by Young's equation as follows (Suzuki & Ueno, 2016):

$$\theta = \frac{\gamma_{LV} - \gamma_{SL}}{\gamma_{LV}} \quad (3.1)$$

Where $\gamma_{SV}$, $\gamma_{SL}$ and $\gamma_{LV}$ are interfacial tensions per unit length of solid-vapor, solid-liquid and liquid-vapor interfaces, respectively. The surface wettability was analyzed by sessile drop test, which measures the contact angle between the distilled water drop and specimen at the point where the liquid–vapor ($\gamma_{LV}$) interface meets the solid–liquid interface ($\gamma_{SV}$), as shown in Figure 3.8.

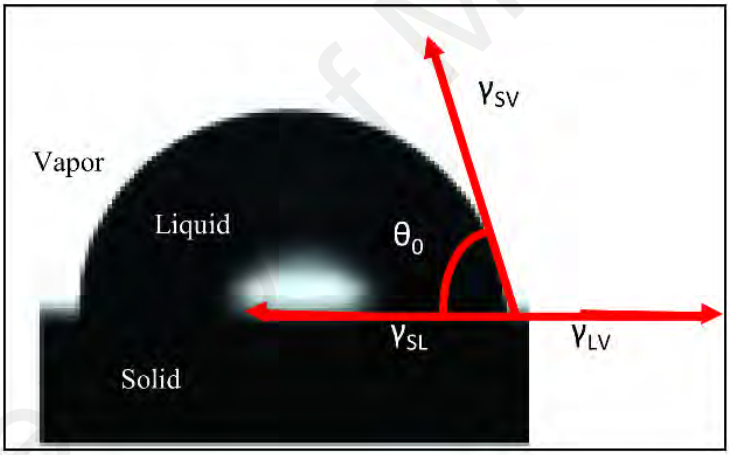


Figure 3.8: Schematic illustration of the wettability study using the ultra-pure double distilled water contact angle

### 3.6.3 Micromechanical analysis

Micro-scratch testing was performed to measure the adhesion strength between the film and substrate using a micro-scratch system (Micro Materials Ltd, Wrexham, U.K.). In general, the most important features of coated surgical instruments are their stability and durability over the long term. For a surgical tool to perform efficiently, it is mandatory that its surface does not spall or leach out particles during operation. Hence,

a strongly adhering layer of an antibacterial agent that can prevent contamination and infection could improve process efficiency significantly (Sharratt, 2006). For this purpose, the thin film-substrate adhesion strength was measured quantitatively with a micro-scratch tester. Thereby, a friction curve and microscopic observations were employed to obtain the critical load ($L_c$) (Othman et al., 2015). Initially, a load of 0 mN was applied with the diamond tip onto the sample. Then the load was gradually increased by 1.5 mN/s at a sliding velocity of 6.0 µm/s until a range of 1500-3500 mN was achieved over a 1000 µm path line. The morphology of the scratch track profile was studied by FESEM. The scratch path line and the damage spot can be measured and directly correlated to the load. The critical loads can be determined from the scratch profile of the load-displacement graph. For all samples, the scratch direction was set from left to right, and three critical loads ($L_{c1}$, $L_{c2}$ and $L_{c3}$) were defined for thin film failure (Hassan et al., 2015). These critical loads are illustrated in Figure 3.9. $L_{c1}$ is a type of cohesive failure characterized by trackside scratches, followed by mild tensile cracking along the scratch path. With a gradual increase in load, delamination was dominant on the trackside and this load was denoted $L_{c2}$. With further load increment, the trackside cracking and delamination became more severe and eventually the thin film completely peeled off the substrate along the scratch path (Stuart et al., 2017). This critical load was expressed as $L_{c3}$.

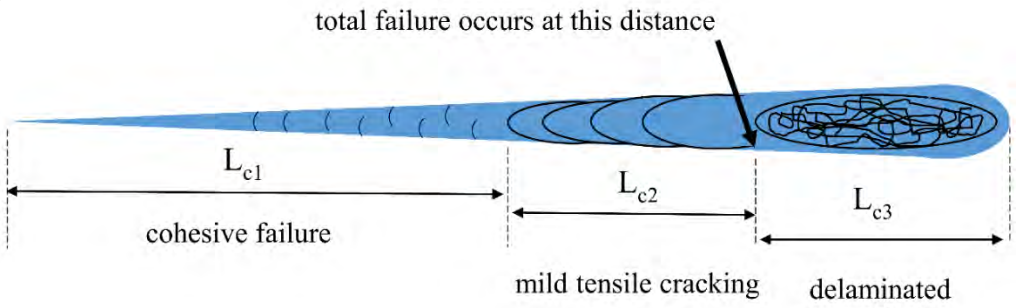


Figure 3.9: Determining $L_{c1}$, $L_{c2}$ and $L_{c3}$ for measuring the adhesion strength

The microhardness was measured with a Vickers microhardness tester (Shimadzu, Japan). Both critical load (adhesion strength) and hardness measurements were repeated three times and the average reading was taken to ensure enhanced accuracy.

### 3.6.4 Topography

The extended surface topography was measured by noncontact AFM (Park NX 10, Korea). AFM allows scanning object surfaces at very high resolution (in the order of a few tenths of a nanometer) and translating into numerical and visual surface data. Here, the roughness average (Ra; the arithmetic average of absolute values) is used.

### 3.6.5 Phase and crystal structure analysis

The phases were identified by XRD (PANalytical Empyrean, Netherlands) with Cu-Kα radiation. The operating voltage and current were set to 40 kV and 40 mA respectively over a 2θ range of 10 º to 90 °.

Crystal structure analysis comprised lamella preparation and selected area electron diffraction (SAED). Focus ion beam (FIB) milling (FEI, Helios NanoLab, G3 UC, Japan) was utilized to prepare very thin lamellae for transmission electron microscopy (TEM). Ion beam platinum (Pt) deposition was performed at 30 kV on the area of interest. The Pt deposition dimensions were 10 x 1.5 x 1 μm and the current was controlled at 1.6–3.2 nA. High current beams of 6.5–32 nA were then applied to mill large amounts of material away from the front and back of the region of interest. The bottom and right edge were cut free, leaving just a tab of material on the left side holding the lamellae. The easy lift needle was attached to the lamellae using Pt deposition, and the sample was lifted out of the bulk material. The lamellae were attached to the Cu Grid. Once the probe was secured to the grid, the probe was milled free from the lamellae. The lamellae were then thinned to <100 nm with 0.79 nA

current. The current was reduced to 80 pA when the thickness approached 100 nm. Finally, low energy milling was used to remove the damaged layer developed by FIB during lamella formation and to further reduce the lamella thickness. The voltage and current used for this milling were 1–5 kV and 100 pA, respectively.

Approximately 60 nm lamellae were used for selected area electron diffraction (SAED). SAED was performed to reveal the phase and crystallinity of the thin film by using a transmission electron microscope (JEOL TEM-2100F HRTEM, Japan) at 200 kV. The value of inter planar spacing ($d_{hkl}$) was determined using equation (3.2) and applied to assign the respective planes as follows:

$$d_{hkl} = \frac{a}{\sqrt{h^2+k^2+l^2}} \tag{3.2}$$

Where 'a' is lattice parameter and, *h, k, l* are plane indices.

### 3.6.6 Nano-Mechanical analysis

Nano-indentation test was performed to measure the film's surface hardness and strength using a Nano indenter Device (Hysitron Ubi TI 750H, US). The experiments were conducted using a Berkovich diamond tip with a radius of 100 nm and constant displacement control depths of 100 nm. The indentation velocity (displacement rate) was 3 nm $s^{-1}$; once the maximum prescribed depth was reached, loading was stopped and the load was kept constant for 10 s. Each indentation was repeated three times and the average value was determined. The elastic modulus was calculated using equation (3.2) according to the data retrieved (Saha & Nix, 2002).

$$\frac{1-{v_s}^2}{E_s} = \frac{1}{E_r} - \frac{1-{v_i}^2}{E_i} \tag{3.2}$$

Where $v_i$ , $E_i$ , $E_r$, $E_s$, and $v_s$ are the Poisson′s ratio of the indenter (0.07), Young's modulus of the indenter (1140 GPa), reduced modulus, Young' modulus of the

sample, and Poisson′s ratio of the sample (0.342), respectively.

### 3.6.7 Surface Chemistry

The exact elemental composition of the developed thin film was determined by X-ray photoelectron spectroscopy (XPS, ULVAC-PHI Quantera II, JAPAN). XPS is an analysis technique to acquire chemical information of the solid materials' surface under study. XPS can determine composition and the chemical state of surface constituents. The material can be characterized by the energy of core electron photoemission as a function of its binding energy and the characteristic of the elements from which it was emitted.

## 3.7 *In vitro* antibacterial activity

The antibacterial activity of the coated thin films (400 °C annealed "$S_1$", 400 °C annealed "$S_7$", 700 °C annealed "$S_7$" and uncoated SS 316L control sample) were tested by halo inhibition zone method. Before the antibacterial activity was performed, the control sample, 400 °C annealed "$S_1$", 400 °C annealed "$S_7$" and 700 °C annealed "$S_7$" were sterilized using 70 % ethanol. The measurement of the inhibition zone diameters across the short axis (A) and long axis (B) are provided in Figure 3.10.

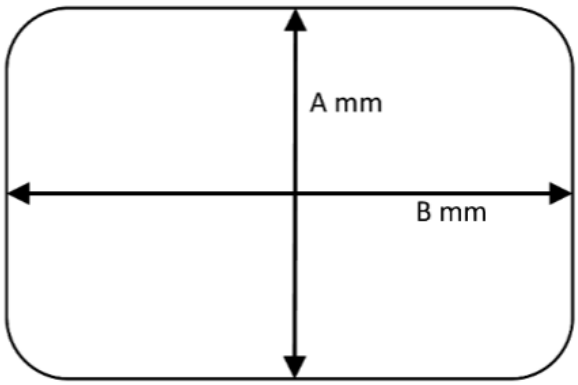


Figure 3.10: Diameter of inhibition zone measured across the short axis (A) and the long axis (B)

### 3.7.1 Evaluation of antibacterial activity in vitro

The antibacterial activity of the 400 °C annealed "$S_1$", 400 °C annealed "$S_7$" and 700 °C annealed "$S_7$" was assessed in comparison to the control sample through halo inhibition zone tests using Gram-negative (Escherichia coli, ATCC 15597) and a Gram-positive (*Staphylococcus aureus*, NCTC 6571) bacteria. Both bacteria were cultured overnight in Luria Bertani (LB) broth at 37 °C with 180 rpm agitation. The bacterial density was adjusted to 1 x $10^5$ colony-forming units per gram (cfu)/ml using LB broth. A sterile cotton swab was used to lawn the bacterial culture on the nutrient agar (NA) plate. The control sample, 400 °C annealed "$S_1$", 400 °C annealed "$S_7$" and 700 °C annealed "$S_7$" were placed face down on the lawn. The samples were then incubated at 37 °C for 17-20 hours and the resulting inhibition zones were measured afterwards. All tests were performed in triplicate.

### 3.7.2 Sterilization

Prior to the evaluating the antibacterial activity, the control sample, 400 °C annealed "$S_1$", 400 and 700 °C annealed "$S_7$" were sterilized using 70 % ethanol. The samples were soaked in 70 % alcohol for 24 hours followed by washing and soaking in sterile distilled water three times for a duration of 4-6 hours each time. The samples were then dried at 70 °C for 24 hours and stored in a desiccator until use.

## 3.8 *In vitro* biocompatibility Test

### 3.8.1 hBMSCs isolation, culture & seeding

The University of Malaya Medical Centre (UMMC) Research Ethics Committee (ethics number 967.10) granted ethical approval to acquire patient bone marrow samples. Human bone marrow aspirate was obtained from subjects (50–70 years old) undergoing total knee replacement. Written informed consent was obtained from the patients prior to acquiring the samples. The hBMSCs (human bone marrow-derived

mesenchymal stromal cells) were isolated as described previously (Bruce et al., 2001). The cells were cultured in low glucose Dulbecco's modified Eagle's Medium (DMEM, Invitrogen, U.S.) supplemented with 10 % fetal bovine serum (FBS, Invitrogen, U.S.), 100 U/mL penicillin (Invitrogen) and 100 mg/mL streptomycin (Invitrogen) in a T75 tissue culture flask at 37 °C in a humidified atmosphere with 5 % $CO_2$. The medium was renewed at three-day intervals. When the cells grew to near confluence (80-90 %), they were detached by trypsin/EDTA (Invitrogen) and then sub-cultured into the next passage. For cell attachment and proliferation analyses, passage 2 hBMSCs were seeded onto all sample groups in 12-well plates with seeding density of $1\times10^6$ cells/ml.

### 3.8.2 Cell attachment analysis

#### 3.8.2.1 Scanning electron microscopy analysis

Scanning electron microscopy (SEM) analysis was performed to observe surface topography of hBMSCs (n=3) seeded on 400 and 700 °C annealed "S7" and uncoated SS 316L (control sample). The samples at day 14 were fixed overnight in 4 % glutaraldehyde in 0.1M cacodylate buffer and post-fixed for 1 h in 1 % aqueous osmium tetroxide. These samples were washed with distilled water in three consecutive steps before dehydration through a graded ethanol series (50, 70, 80, 90, 95 and 100 %). The samples were subsequently critical point-dried with a Bal-Tec CPD030. The samples were mounted on aluminum stubs and sputter coated with gold before examination using a tabletop scanning electron microscope (Phenom proX, Desktop SEM).

#### 3.8.2.2 Confocal microscopy analysis

Confocal laser microscopy analysis was performed to determine the cell density as well as the F-actin remodeling of seeded cells seeded on the material surfaces. The hBMSCs seeded on the 400 °C annealed "$S_7$", 700 °C annealed "$S_7$" and SS 316L (Day 14; n = 3) samples were stained with green-fluorescent Alexa Fluor 488 phallotoxins F-

actin and counterstained with blue fluorescent 460 Hoechst 33342 nucleic acid staining (Invitrogen). The samples were stained according to the protocol provided by the manufacturer. After 20 min of incubation, the samples were washed with phosphate buffer saline (PBS) and observed using an inverted confocal laser microscope (Leica TCS SP8 X, UK).

### 3.8.3 alamarBlue ™ cell viability and proliferation assay

The cell proliferation (n=4) in 400 °C annealed "$S_1$", 400 and 700 °C annealed "$S_7$" and the control sample was assessed using the colorimetric indicator alamarBlue™ assay (Gibco, USA). The assay was carried out based on the percentage of alamarBlue™ (AB) reduction on day 1, 3, 7 and 14. The percentage of AB reduced by the cells was calculated using the formula provided in the manufacturer's protocol (Gibco, U.S.). AB was directly added into the DMEM in all preparations at a final concentration of 10 % and incubated for 10 h. After incubation, 100 µl of medium from each plate were transferred into a 96-well plate in duplicates. AB added to media without cells served as a negative control. The absorbance in each well was measured at 570 and 600 nm (reference wavelength) using a microplate reader (Epoch, U.S.).

# CHAPTER 4: RESULTS & DISCUSSION

This chapter presents the results and a discussion of the as-deposited and annealed single layer (SL) and multilayer (ML) samples of Ag-$Ta_2O_5$ and Ag/Ag-$Ta_2O_5$ thin film. The results are summarized in Table 4.1.

Table 4.1: Summary of as-deposited and annealed samples of Ag-$Ta_2O_5$ and Ag/Ag-$Ta_2O_5$ thin films

| Method | Sample | Preparation |
|---|---|---|
| A | "$S_1$" | SL deposited at 200 W, 60 sscm, 140 °C |
| | 300 °C annealed"$S_1$" | Annealed at 300 °C and 5 °C ramp rate |
| | 400 °C annealed"$S_1$" | Annealed at 400 °C and 5 °C ramp rate |
| | 500 °C annealed"$S_1$" | Annealed at 500 °C and 5 °C ramp rate |
| | 600 °C annealed"$S_1$" | Annealed at 600 °C and 5 °C ramp rate |
| B | "$S_2$" | ML deposited at 200 W, 60 sscm, 140 °C |
| | "$S_3$" | ML deposited at 300 W, 30 sscm, 140 °C |
| | "$S_4$" | ML deposited at 300 W, 45 sscm, 250 °C |
| | 400 °C annealed"$S_4$" | Annealed at 400 °C and 2 °C ramp rate |
| | "$S_5$" | ML deposited at 300 W, 60 sscm, 280 °C |
| C | "$S_6$" | ML deposited at 100 W, 45 sscm, 250 °C |
| | "$S_7$" | ML deposited at 200 W, 45 sscm, 250 °C |
| | 250 °C annealed"$S_7$" | Annealed at 250 °C and 2 °C ramp rate |
| | 400 °C annealed"$S_7$" | Annealed at 400 °C and 2 °C ramp rate |
| | 550 °C annealed"$S_7$" | Annealed at 550 °C and 2 °C ramp rate |
| | 700 °C annealed"$S_7$" | Annealed at 700 °C and 2 °C ramp rate |

Table 4.1 continued: Summary of as-deposited and annealed samples of Ag-$Ta_2O_5$ and Ag/Ag-$Ta_2O_5$ thin films

| | | |
|---|---|---|
| | 850 °C annealed"$S_7$" | Annealed at 850 °C and 2 °C ramp rate |
| | "$S_8$" | ML deposited at 300 W, 45 sscm, 250 °C |
| | "$S_9$" | ML deposited at 200 W, 45 sscm, ambient |
| | "$S_{10}$" | ML deposited at 200 W, 45 sscm, 150 °C |

## 4.1 Method A: "$S_1$" and annealed "$S_1$" of Ag-$Ta_2O_5$ thin films

This section confers the data analysis for the experimental results obtained with Method A. The surface microstructure, element composition, cross-sectional view, surface wettability, adhesion strength evaluation, surface topography and phase analysis of the as-deposited and annealed "$S_1$" samples of single layer Ag-$Ta_2O_5$ thin film are discussed. Later, the microstructures of the focused ion beam (FIB)-milled section and selected area electron diffraction (SAED) of as-deposited "$S_1$" and 400°C annealed Ag-$Ta_2O_5$ thin films are elaborated. The last part addresses an evaluation of the antibacterial test for the control and 400 °C annealed "$S_1$" Ag-$Ta_2O_5$ thin film samples.

### 4.1.1 Surface microstructural analysis of "$S_1$"

The surface of the as-deposited Ag-$Ta_2O_5$ nanocomposite ("$S_1$") appeared shiny black at first. The surface then changed to dull white after annealing, with an increase in brightness by increasing the annealing temperature. Figure 4.1(a) presents the FESEM microstructural analysis of as-deposited "$S_1$" Ag-$Ta_2O_5$ thin film. An even distribution of Ag-$Ta_2O_5$ nanocomposite particles was observed with the presence of a few Ag crystals in the Ag-$Ta_2O_5$ matrix.

.

### 4.1.2 Surface microstructural analysis of "$S_1$" annealed at 5 °C/min

Figure 4.1 (b-f) presents the FESEM microstructural analysis of "$S_1$" Ag-$Ta_2O_5$ thin film annealed at 300–600 °C and a ramp rate of 5 °C/min. Clustering/segregation of Ag initiated in the form of lamellae was observed when the nanocomposite was annealed at 300 ºC. This finding is comparable with Mulligan et al. (2012) work. This is primarily due to the high surface energy of the nanosized Ag particles (Figure 4.1(b)). This kind of Ag segregation on the surface has been observed by several other researchers. For instance, it has been noted that the level of segregation significantly increases with increasing Ag content in the thin film and annealing temperature (Lan et al., 2013; Velasco et al., 2016). At this stage, the surface of the thin film still had some pockets/porosity where the Ag-$Ta_2O_5$ composite was found. Annealing further at even higher temperatures resulted in Ag phase segregation, as seen in Figures 4.1(c-f). The thin film surface was complete covered when these samples were annealed at temperatures beyond 400 ºC. Such entirely segregated Ag layer with an underlying Ag-depleted layer has been reported in several ceramic-Ag systems (e.g. CrNAg and YSZAgMo) due to the low reactivity of Ag with other constituents and high surface energy of AgNPs (Hu et al., 2007; Incerti et al., 2011; Muratore et al., 2005). The effect of annealing temperature on the segregation of Ag on the thin film surface was confirmed with the help of EDX, as presented in Table 4.1.

### 4.1.3 Elemental analysis (EDX) of "$S_1$" and "$S_1$" annealed at 5 °C/min

The EDX result of the as-deposited layer shows quite similar contents of Ag and Ta with the presence of some oxygen. When the sample was annealed at 300 ºC, two distinct phases appeared, as seen in Figure 4.1(b). The island regions are Ag segregates and the remaining region is slightly leaner in Ag content compared to the unannealed sample. Upon annealing at temperatures higher than 300 ºC (i.e. 400, 500, and 600 ºC),

a continuous homogenous layer of Ag segregated on the surface (Figures 4.1(c-f)). This layer acts as a barrier preventing the electron beam from accessing the underlying Ta and O. Hence, the EDX detector collects minimal (or no) signals from these elements. The segregation of Ag as a result of the thermal treatment of the ceramic-Ag layer and its morphology were reviewed in detail by (Velasco et al., 2016).

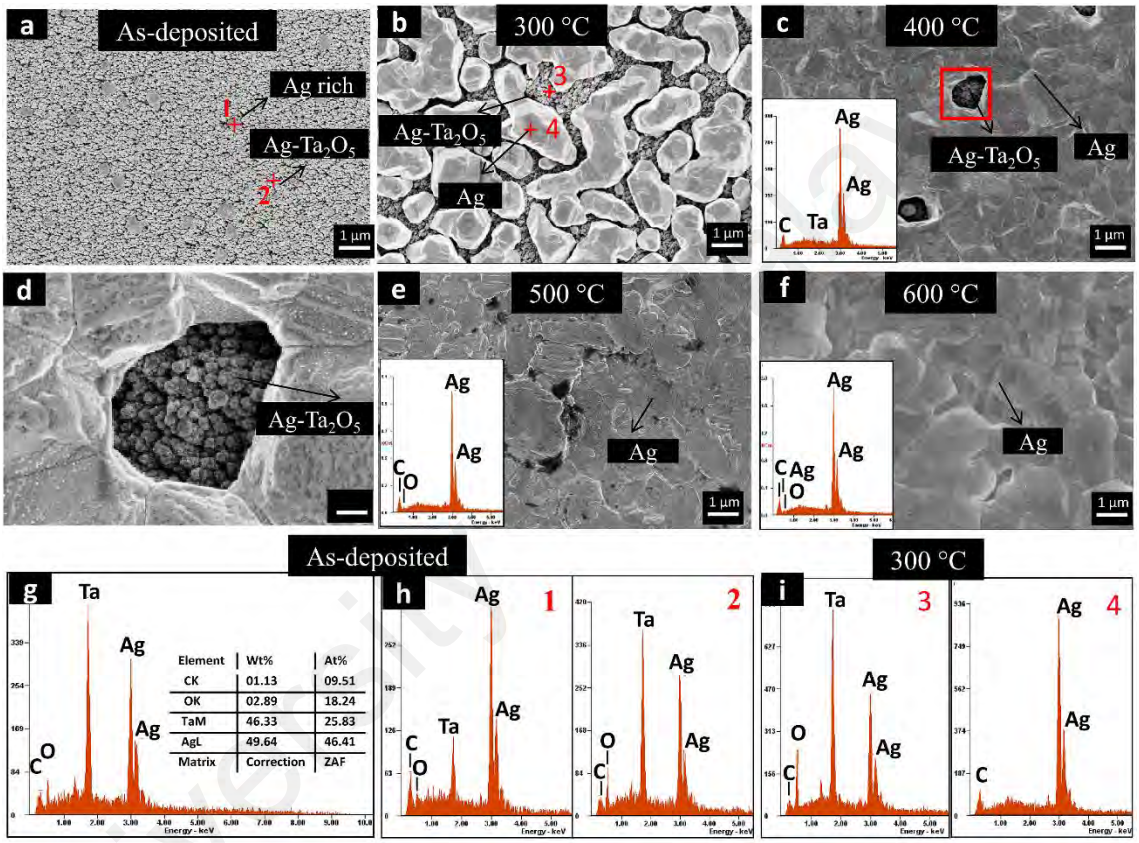


Figure 4.1: FESEM surface morphology of Ag-$Ta_2O_5$ thin film.

(a) as-deposited "$S_1$", (b) Ag segregation resulting from annealing the as-deposited "$S_1$" at 300 °C, (c) image of the 400 °C annealed "$S_1$" and it EDX, (d) magnified image of the part highlighted in (c), Ag segregated surface and chemical composition of "$S_1$" annealed at (e) 500 °C and (f) 600 °C; EDX of as-deposited "$S_1$": (g) entire image, (h) point 1 and 2, and (i) 300 °C annealed "$S_1$" at point 3 and 4

Table 4.2: Elemental analysis of as-deposited "$S_1$", and annealed combination of Ag-$Ta_2O_5$ thin film corresponding to FESEM surface microstructure in Figure 4.1

| Samples | Weight percentage (%) | | |
|---|---|---|---|
| | Ag | Ta | O |
| As-deposited | 46.92 | 49.30 | 2.64 |
| As-deposited (point 1) | 76.25 | 17.89 | 3.45 |
| As-deposited (point 2) | 47.26 | 47.92 | 3.71 |
| 300 °C (point 3) | 42.57 | 49.27 | 6.95 |
| 300 °C (point 4) | 98.44 | | |
| 400 °C | 96.55 | 1.93 | |
| 500 °C | 97.00 | | 1.29 |
| 600 °C | 97.89 | | 0.63 |

### 4.1.4 Cross sectional view of "$S_1$" and "$S_1$" annealed at 5 °C/min

Cross-sectional FESEM micrographs of the developed layers are shown in Figures 4.2 (a-d), while parts (e-f) depict the Ag segregation mechanism schematically. The cross section of the as-deposited Ag-$Ta_2O_5$ exhibits homogeneous morphology throughout the film thickness, as shown in Figure 4.2(a). The thermal treatment triggered the diffusion of Ag atoms from the thin film nanocomposite to the surface of the specimen. The thermal treatment energy was sufficient for Ag to diffuse but not enough for $Ta_2O_5$ to fill in the gaps (vacancies) generated by the thermal migration and solid-state diffusion of silver atoms (Hu et al., 2007). Actually, the annealing temperature was far below the melting point of any of these composite components. The generation of porosity as a result of Ag migration from the underlying layer was also reported in a previous study (Mulligan et al., 2012). Due to the relatively low reactivity

of Ag, almost no intermetallic phase or compound formed between Ag and the other constituents, which also led to greater mobility of the Ag atoms (Velasco et al., 2016). The XRD and TEM analyses support this argument, as discussed in the subsequent section. The thermal treatment increased the thin film thickness because of the porosity developed and the stress relief for the constituents of the lower layer. The porosity and thin film thickness of the annealed samples increased with the rise in annealing temperature (Figures 4.2(b-d)). Samples "$S_1$" annealed at 300, 500 and 600 °C had thicknesses of 5.49±0.02, 6.81±0.17, 7.97±0.14 and 8.86±0.05 μm, respectively.

.

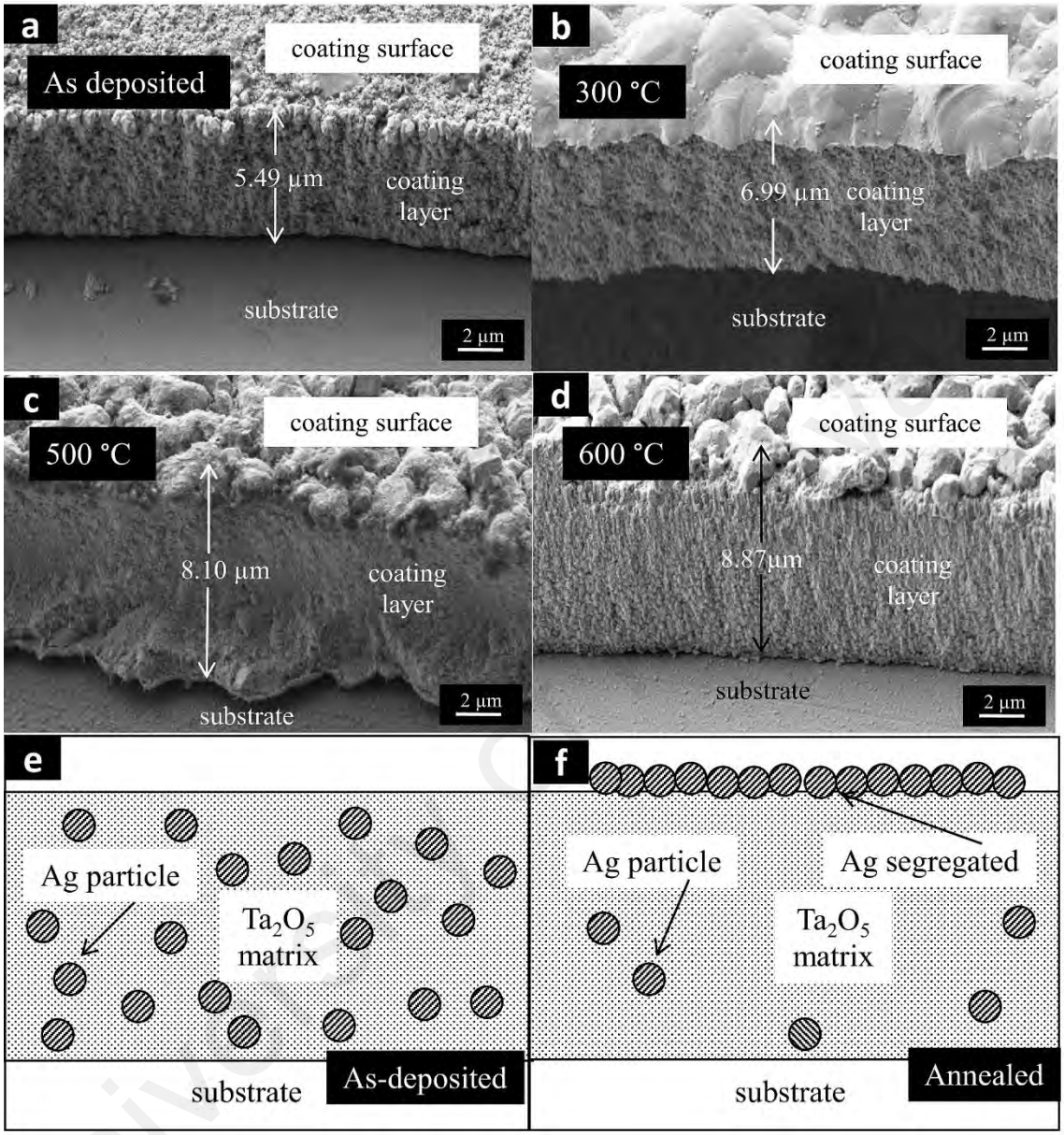


Figure 4.2: FESEM cross section view of (a) as-deposited "$S_1$", (b) "$S_1$" annealed at 300, (c) 500, (d) 600 °C, schematic of Ag particle mobility (e) as-deposited and its segregation of (f) annealed sample

### 4.1.5 Surface microstructural and EDX analyses of "$S_1$" annealed at 500 °C and 2 °C/min

Figure 4.3(a-b) presents the FESEM surface morphology and EDX analyses followed by the cross sectional microstructure of as-deposited "$S_1$" annealed at 500 °C using ramp rate of 2 °C/min. After annealing, Ag apparently segregated in the subsurface as depicted in Figures 4.3(c & e), similar to the case of 5 °C/min ramp rate in Figure 4.1.

However, annealing this nanocomposite at different temperature and time (ramp rate) increments displayed distinct surface morphology, elemental composition and film thickness results. The effect of ramp rate on the segregation of Ag on the thin film surface was confirmed with the help of EDX. Annealing at 2 °C/min showed that the thin film still has some morphology (pocket-shaped regions) where Ag-$Ta_2O_5$ composite was present (Figure 4.3(c)). During ramping, the annealing temperature encouraged the Ag nuclei to migrate and coalesce with each other, forming larger Ag particles (solid-state diffusions). Figure 4.3(c) indicates that the slower 'Ostwald ripening' rate facilitated the appearance of Ag-$Ta_2O_5$ composite pockets.

In contrast, at a higher ramp rate (5 °C/min) the Ag coalesced faster. Despite the segregated Ag being able to cover the film surface at a higher ramp rate, such ramp rate could shorten the coalescence time. Since Ag did not have enough time to prolong the particle growth, relatively smaller segregated Ag particles are observed, as per Figure 4.1(e). But Figure 4.3(a) signifies that a lower ramp rate provided Ag sufficient time to build relatively bigger segregated particles (Wuu et al., 2000). Accordingly, incrementing thin film thickness (7.62±0.02 μm) with microstructure porosity in "$S_1$" annealed at 500 °C and 5 °C/min ramp rate is also noted in "$S_1$" annealed at 500 °C but at 2 °C/min ramp rate. The thickness increment of "$S_1$" annealed at 500 °C and 2

°C/min was 4.6 % lower than "$S_1$" annealed at 500 °C and 5 °C/min to the slower Ag coalescence process.

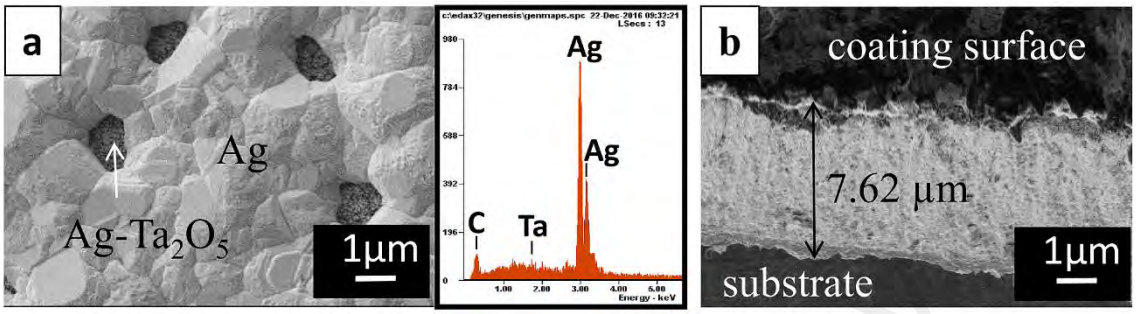


Figure 4.3: FESEM surface morphology of Ag-$Ta_2O_5$ thin film and its EDS followed by cross section views of (a,b) "$S_1$" annealed at 500 °C and 2 °C/ min

### 4.1.6 Surface wettability of "S1" and annealed "S1"

Figure 4.4 exhibits an increasing trend in the contact angle as a function of annealing temperature, suggesting the suitability of annealing treatment for Ag-$Ta_2O_5$ thin films. The contact angle of the as-deposited "$S_1$" was 55.8±1.7 °. This low contact angle is due to the distribution of Ag-$Ta_2O_5$ nanocomposite particles size on the surface. However, the angle enlarged upon annealing at 300 °C (58.6±5.0 °), 400 °C (62.3±1.0 °), 500 °C (75.4±2.3 °) and 600 °C (91.6±0.8 °). This is positively correlated with the Ag particle size which progressively segregated after the annealing thermal treatment.

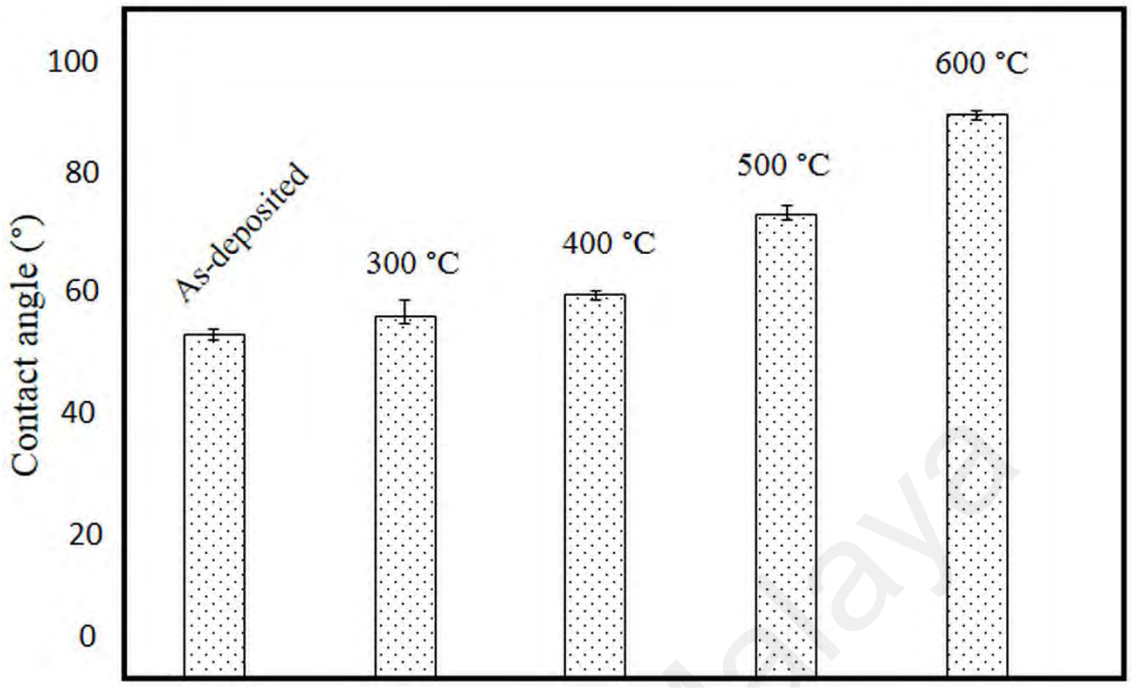


Figure 4.4: Contact angle on as-deposited "$S_1$" and "$S_1$" annealed at 300, 400, 500 and 600 °C of Ag-$Ta_2O_5$ thin films

### 4.1.7 Adhesion strength of "$S_1$" and "S1" annealed at 5 °C/min

Table 4.3 tabulates the thin film adhesion and hardness results of as-deposited "$S_1$" and the samples subsequently annealed at 300–600 °C and 5 °C/min ramp rate. The test signified that Ag-$Ta_2O_5$ nanocomposite thin film "$S_1$" annealed at 400°C achieved the strongest adhesion strength. The as-deposited "$S_1$" exhibited the highest microhardness value. The microhardness decreased with an increase in annealing temperature and it became constant after the significant Ag segregation on the surface at 400 °C. The decreased in microhardness after annealing temperature is attributed to the significant change in surface morphology as affirmed in FESEM microstructural and will elaborated further in the surface topography section.

Table 4.3: Thin film adhesion strength and hardness values of as-deposited "$S_1$" and "$S_1$" annealed Ag-$Ta_2O_5$ thin films

| Samples | Critical load (mN) | Hardness ($Hv_{0.3}$) |
|---|---|---|
| As-deposited | 728 ±20 | 178 ±1 |
| 300 °C annealed | 2105 ±25 | 156 ±2 |
| 400 °C annealed | 2927 ±84 | 148 ±0 |
| 500 °C annealed | 2259 ±60 | 148 ±1 |
| 600 °C annealed | 946 ±141 | 148 ±2 |

Figure 4.5 represents the corresponding adhesion strength analysis graphs of depth (I), load (II) and friction (III) versus distance for (i) as-deposited "$S_1$" and (ii) sample subsequently annealed at 400 $^oC$ (with the highest adhesion strength). The failure points on the thin films are marked. The scratch distance denotes the total distance required for the scratch track to remove the thin film layer (Blees et al., 2000). The critical load determines the amount of load that the thin film layer can withstand before substrate-thin film transition (failure) occurs to provide the adhesion strength value.

In order to determine the actual failure point on the coated thin film accurately, FESEM images and EDX analysis were employed. In Figure 4.5(a), as the load increased progressively abrasion signs were noticed before full failure occurred at a distance of 462 μm (SEM micrograph in Figure 4.5(b)) from the circular mark. A load of 738 mN was required to remove the as-deposited "$S_1$" thin film. According to Figure 4.5(c), the scratch progression started with chipping at both edges of the scratch track. Point P5 signified the actual failure point where a distance of 822 μm and load of about

3000 mN were needed until the substrate was totally exposed (Figure 4.5(d)). The 3000 mN load value is significantly higher than in any earlier reports. The enhanced adhesion strength was achieved on account of the anchoring effect between the thin film coating and substrate. Similar findings have been established in other studies on thin films (Arslan et al., 2010; Jingjing et al., 2015; Jocham et al., 2011; Xu et al., 2015). It is highly possible that solid-state diffusion followed the thermal treatment, which resulted in high adhesion strength.

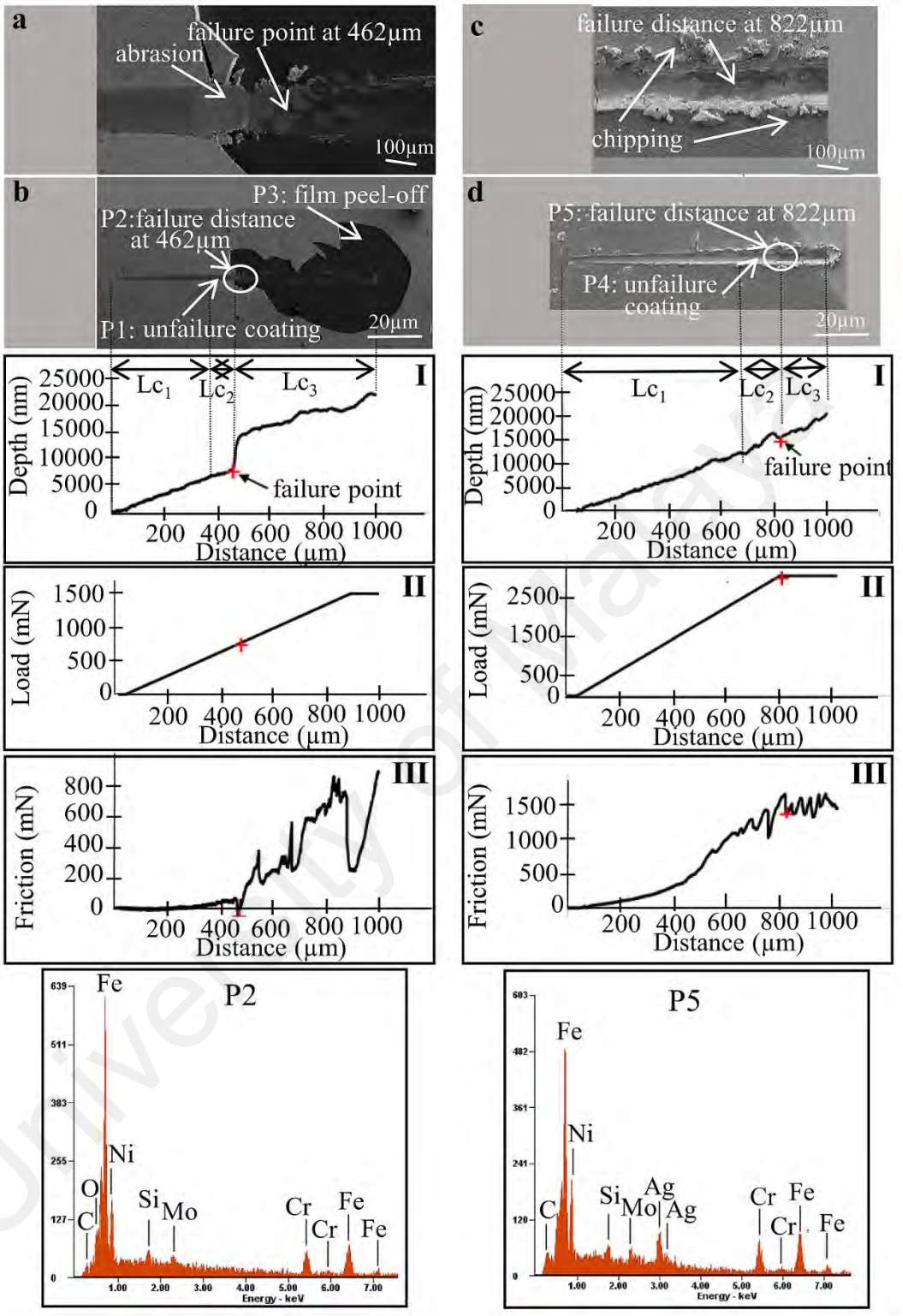


Figure 4.5: FESEM images of scratch test on as-deposited "$S_1$" Ag-$Ta_2O_5$ layer (a,b) and 400 °C annealed "$S_1$" (c,d) followed by respective adhesion strength analysis (depth and load versus distance graph) and EDX analysis

Table 4.4 summarizes the elemental analysis of 5 points on the scratches in Figures 4.5(i) as-deposited "$S_1$" and ii) sample subsequently annealed at 400 $^oC$. At point P1, EDX revealed about 60.7, 32.2 and 5.2 % Ag, Ta and O in the thin film, respectively. At point P2, EDX primarily identified substrate elements that suggest complete thin film removal. Point P2 clearly shows the actual failure point at a scratch distance of 512 μm with 738 mN adhesion strength. At point P4, EDX revealed only Ag-$Ta_2O_5$ elements (40.5 % Ag, 41.2 % Ta) and small concentrations of C (2.8 %) and Fe (1.9 %) similar to the untreated sample. However, at P5 only 8.1 % Ag was present with dominant substrate elements, suggesting complete thin film delamination. Figure 4.5(b) suggests a combination of ductility from Ag and hardness from the $Ta_2O_5$ layers in section Lc3 corresponding to the Ag-$Ta_2O_5$ rich layer, which is in agreement with the microstructural findings.

Table 4.4**:** Elemental analysis of five points corresponding to FESEM surface scratch image of as-deposited "$S_1$" and 400 °C annealed "$S_1$" of Ag-$Ta_2O_5$ thin film

| Spectrum | Element composition (weight %) | | | | | | | | | |
|---|---|---|---|---|---|---|---|---|---|---|
| | Thin film elements | | | Substrate elements | | | | | | |
| | Ag | Ta | O | Fe | Cr | Ni | C | Mo | F | Si |
| P1 | 60.7 | 32.2 | 5.2 | | | | | | | |
| P2 | | | | 66.8 | 16.3 | 13.8 | | 2.3 | | 0.8 |
| P3 | | | | 63.8 | 15.9 | 14.2 | 2.1 | 1.9 | 1.6 | 0.7 |
| P4 | 40.5 | 41.2 | 8.3 | 1.9 | | | 2.8 | | | |
| P5 | 8.1 | | | 58.6 | 14.8 | 9.1 | 3.1 | 1.6 | | |

### 4.1.8 Adhesion strength of "$S_1$" annealed at 500 °C and 2 °C/min

Figure 4.6 represents the corresponding graphs of depth (I), load (II) and friction (III) versus distance for the Ag-$Ta_2O_5$ sample "$S_1$" annealed at 500 °C and 2 °C/min ramp rate. By comparing Figure 4.6(a) and (b), as the load increased progressively chipping noticed at distance of 380 µm in (a) and 230 µm (b) suggesting that "S1" annealed at 500 °C and 2 °C/min is more resistant to the scratch. The failure points on the thin films are marked. As seen in Figure 4.6(a), the failure point on "$S_1$" annealed at 500 °C and 2 °C/min occurred at 726 µm and about 2700 mN of load. Moreover, after the failure point, the delamination on "S1" annealed at 500 °C and 2 °C/min was less severe. It is shown that the adhesion strength of this sample (2701±50.74 mN) overrides the sample annealed at 500 °C and 5 °C/min ramp rate (Figure 4.6(a)).

.

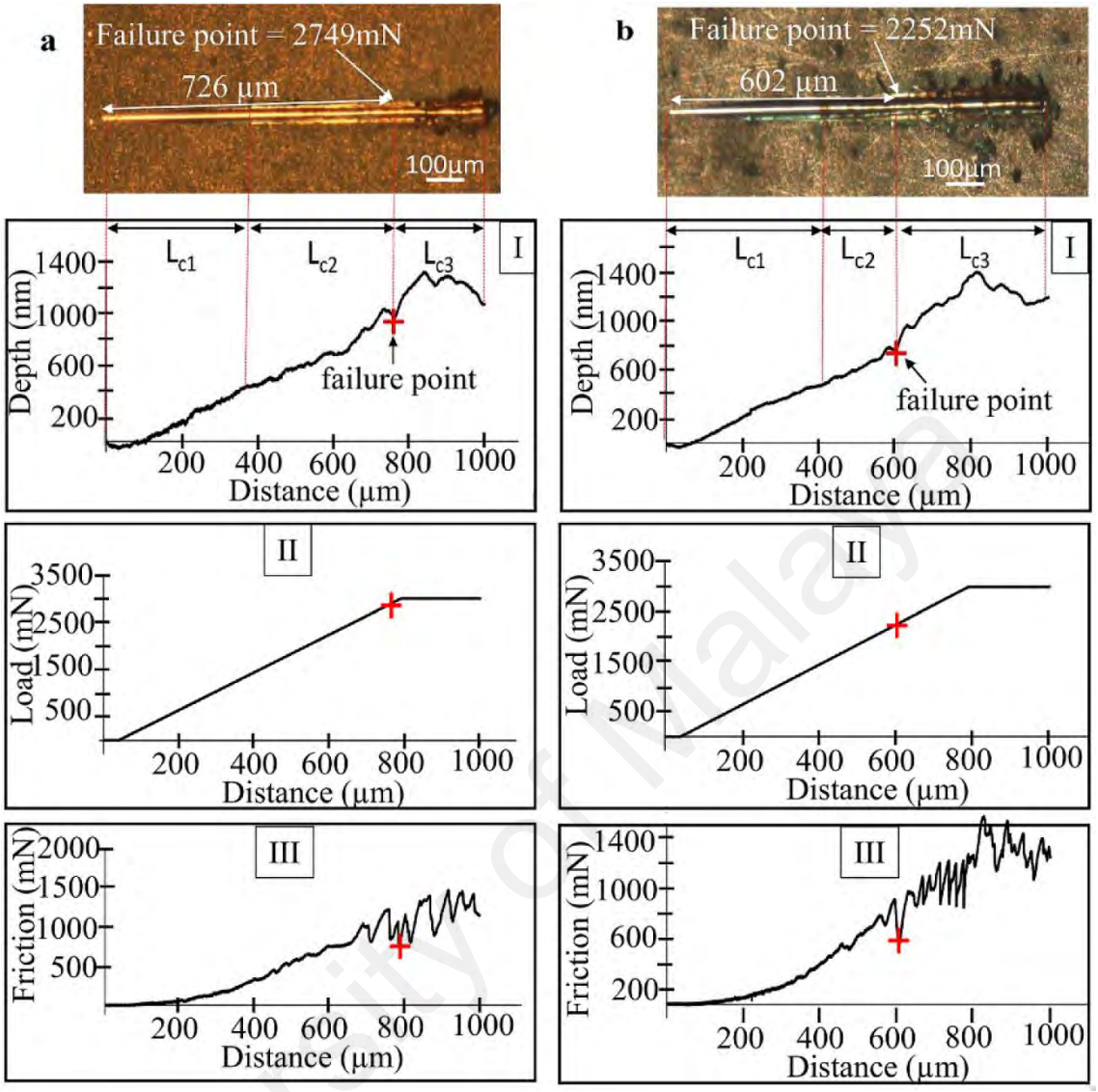


Figure 4.6: FESEM image of scratch test on "$S_1$" annealed at 500 °C and (a) 2 °C/ min and (b) 5 °C/ min followed by respective adhesion strength analysis (depth and load versus distance graph)

### 4.1.9 Surface topography of "$S_1$" and annealed "$S_1$"

The surface topography of all layers developed was analyzed via the atomic force microscopy (AFM) measurements. Figures 4.7(a-f) illustrate the AFM views of as-deposited "$S_1$" and the annealed Ag/Ag-$Ta_2O_5$ thin film sample "$S_1$". The AFM surface topography is very much in agreement with the topographic features visible in the FESEM image in Figure 4.1. Figure 4.7(a) exhibits low surface roughness with several

hills and valleys (similar to Figure 4.1(a), which is a characteristic feature of the as-deposited "$S_1$" layers. Upon exposure to heat during annealing at 300 ºC, the peak height and surface roughness increased owing to the Ag segregation (Figure 4.7(b)).

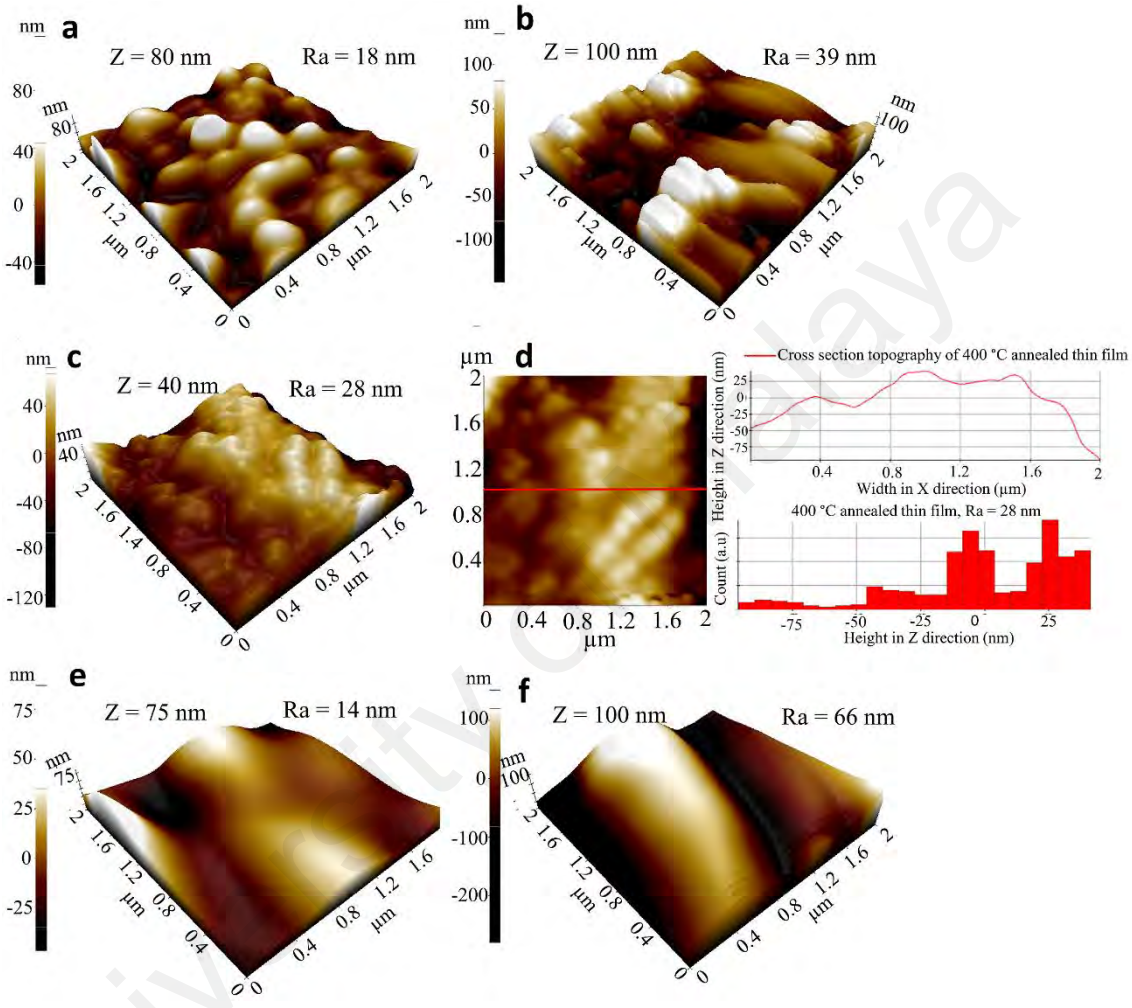


Figure 4.7**:** AFM view, grain height in Z direction and surface roughness value (RMS)

(a) 3 D view of the as-deposited "$S_1$", (b) 3 D view of the 300 °C annealed "$S_1$" , (c) 3 D view of the 400 °C annealed "$S_1$" (d) 2 D view of the 400 °C annealed "$S_1$" with cross sectional topography and height distribution of grain size in Z direction, (e) 3 D view of the 500 °C annealed "$S_1$" , (f) 3 D view of the 600 °C annealed"$S_1$".

With a further increase in annealing temperature (to 400 ºC), significant Ag segregation started. Thus, Ag did not cover the whole surface, leaving a few pockets and exposing the nanocomposite (Figure 4.7(c)). This segregation yielded the lowest combination of peak height and roughness primarily due to the fine grain size of the segregated Ag crystals. Further annealing at higher temperatures (500 and 600 ºC) resulted in Ag segregation lamellae with larger crystallite size due to the Ostwald ripening effect (Velasco et al., 2016). The excessive crystallization was responsible for the high variance in peak height and roughness observed in Figures 4.7(e & f).

Table 4.5 compares the surface roughness and contact angle values of all samples. The observations indicate that increasing the annealing temperature of as-deposited Ag-$Ta_2O_5$ ("$S_1$") from 300 to 600 °C resulted in a linear increase in contact angle. Due to the homogenous sputtering, the roughness of as-deposited "$S_1$" was very low, but it increased drastically because hill and valley-like structures developed due to the partial agglomeration of Ag particles when annealing at 300 °C (Figure 4.7(b)).

Table 4.5: Comparison of surface roughness and contact angle values of as-deposited "$S_1$" and annealed "$S_1$" Ag/Ag-$Ta_2O_5$ thin films

| Samples | Surface roughness (nm) | Contact angle (°) |
|---|---|---|
| As-deposited | 18 | 55.8±1.7 |
| 300 °C | 39 | 58.5±5.0 |
| 400 °C | 28 | 62.3±1.0 |
| 500 °C | 14 | 75.4±2.3 |
| 600 °C | 66 | 91.6±0.8 |

### 4.1.10 Phase analysis of "$S_1$" and "$S_1$" annealed at 5 °C/min

Structural analysis of the developed composite layers was carried out using XRD and SAED. The as-deposited Ag-$Ta_2O_5$ "$S_1$" layer displayed only the presence of Ag (ICSD No. 98-002- 4387) on the surface due to the amorphous nature of as-developed TaO. According to the X-ray diffraction pattern, $Ta_xO_x$ crystallizes at temperatures above 600 ºC, which conforms with other findings (Zhabrev et al., 2004).

The XRD pattern of the as-deposited "$S_1$" exhibited significant noise, denoting the presence of amorphous content in the layer. Annealing the coated samples at 300 ºC and above presented excessive Ag segregation and crystallization on the surface, which exposed only Ag to the X-rays, resulting in peak intensity enhancement. In the sample annealed at 500 ºC (sufficiently high temperature), Ag near the surface reacted with $Ta_2O_5$ to form $AgTaO_3$ (ICSD No. 98-004-0830). Very low intensity peaks for this new phase appeared at this temperature, but the peaks significantly strengthened for the sample annealed at 600 ºC (Figure 4.8).

Upon annealing at higher temperatures, the individual islands joined together, resulting in decreased surface roughness that continued to decrease at 500 ºC annealing due to further grain growth (Figures 4.7(c, e)). Annealing at 600 ºC stabilized the newly developed $AgTaO_3$ phase, which is evident in the XRD pattern in Figure 4.8. This new phase (rhombohedral crystalline structure) was probably responsible for the greater roughness of the sample due to the different crystalline morphologies of Ag (face centered cubic).

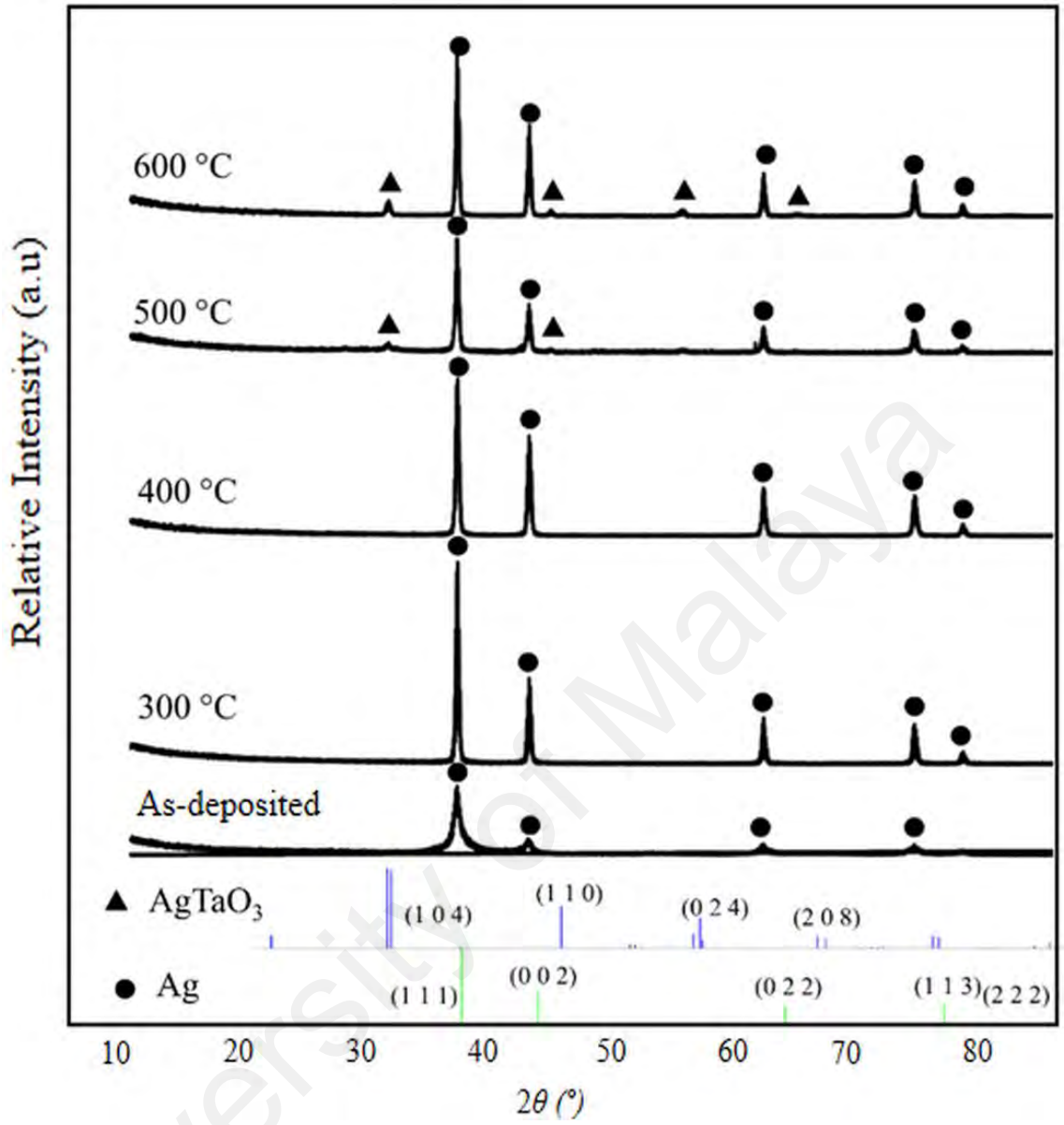


Figure 4.8: XRD patterns of nanocomposite Ag-$Ta_2O_5$ thin film of as-deposited "$S_1$" and after annealing at 300, 400, 500 and 600 °C

### 4.1.11 Phase analysis of "$S_1$" annealed at 500 °C and 2°C/min

Figure 4.9 shows the XRD patterns of 500 °C annealed "$S_1$"of Ag-$Ta_2O_5$ prepared at 2 °C/min and 5 °C/min ramp rate. "$S_1$" annealed at 2 °C/min ramp rate had greater Ag peak intensity than the sample annealed at the same temperature and 5 °C/min ramp rate. This result is correlated with the bigger segregated Ag particles (Figure 4.3(a)). In

addition, the slower coalescence suggests that the stability of Ag during migration prevented the reaction with $Ta_2O_5$ from forming $AgTaO_3$ (ICSD No. 98-004-0830).

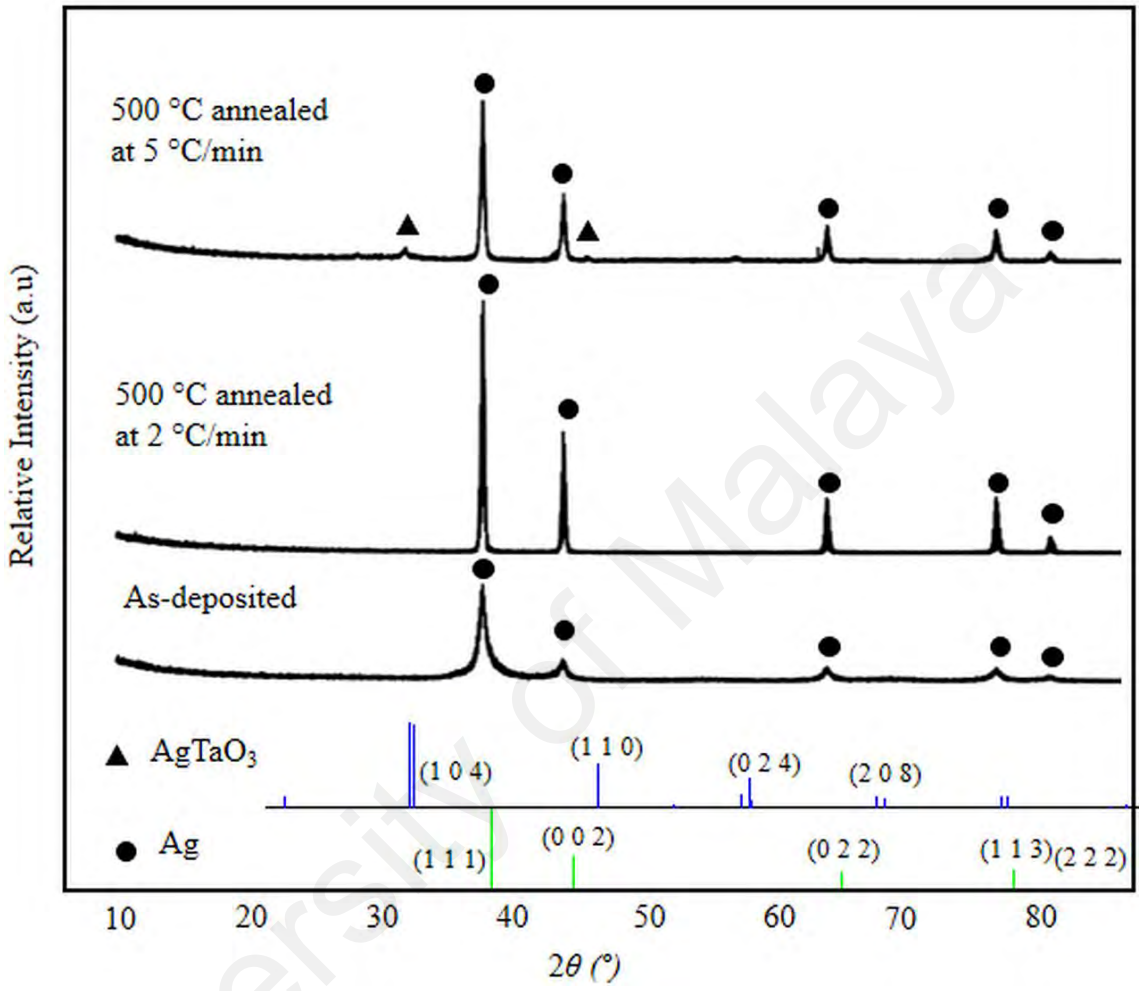


Figure 4.9: (a) XRD patterns of 500 °C annealed "$S_1$"prepared at 2 °C/ min and 5 °C/min of Ag-$Ta_2O_5$ thin film

### 4.1.12 Microstructure of FIB milled section of "S1" and 400 °C annealed "$S_1$"

An FESEM analysis of the FIB-milled section is presented in Figure 4.10. The FIB cross section of the as-deposited "$S_1$" layer is shown in Figure 4.10(b) and that of the 400 ºC annealed "$S_1$" layer of Ag-$Ta_2O_5$ is shown in Figure 4.10(d). Figure 4.10(b) suggests a homogeneously deposited layer throughout the thin film thickness. The sections highlighted in Figures 4.10(b) and (d) were selected for SAED analysis, which

is displayed in Figure 4.11. Three (3) regions are recognized in Figure 4.10(d). The bottom region is brighter, where Ag was depleted due to the migration of Ag towards the surface. The middle region with a contrast still contained some Ag due to the lower annealing temperature (400 ºC). The top lamellae denote pure segregated Ag that migrated from the bottom due to its lower reactivity and higher surface energy, as discussed in earlier sections.

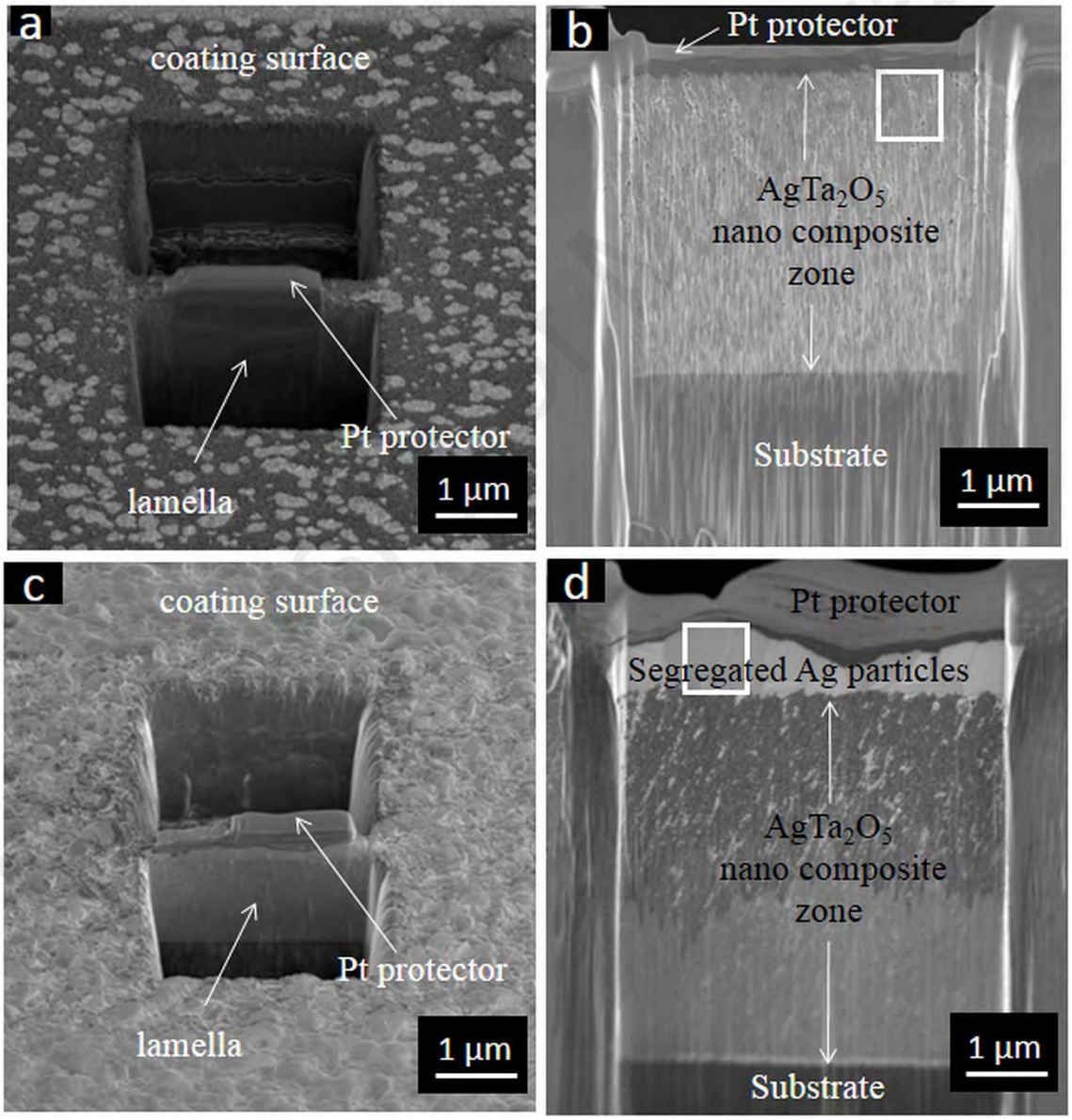


Figure 4.10: FESEM image of FIB section, (a,b) as-deposited "$S_1$" layer, (c,d) 400 °C annealed "$S_1$"

### 4.1.13 TEM-SAED analysis of "S1" and 400 °C annealed "S1"

Figure 4.11 presents the SAED analysis of selected sections on the Ag-$Ta_2O_5$ thin film as-deposited "S1" (a-c) and the 400 °C annealed "S1" (e-f). The zone highlighted in Figure 4.11(a) was targeted for high-resolution TEM imaging, after which the SAED pattern was determined as shown in Figure 4.11(b).

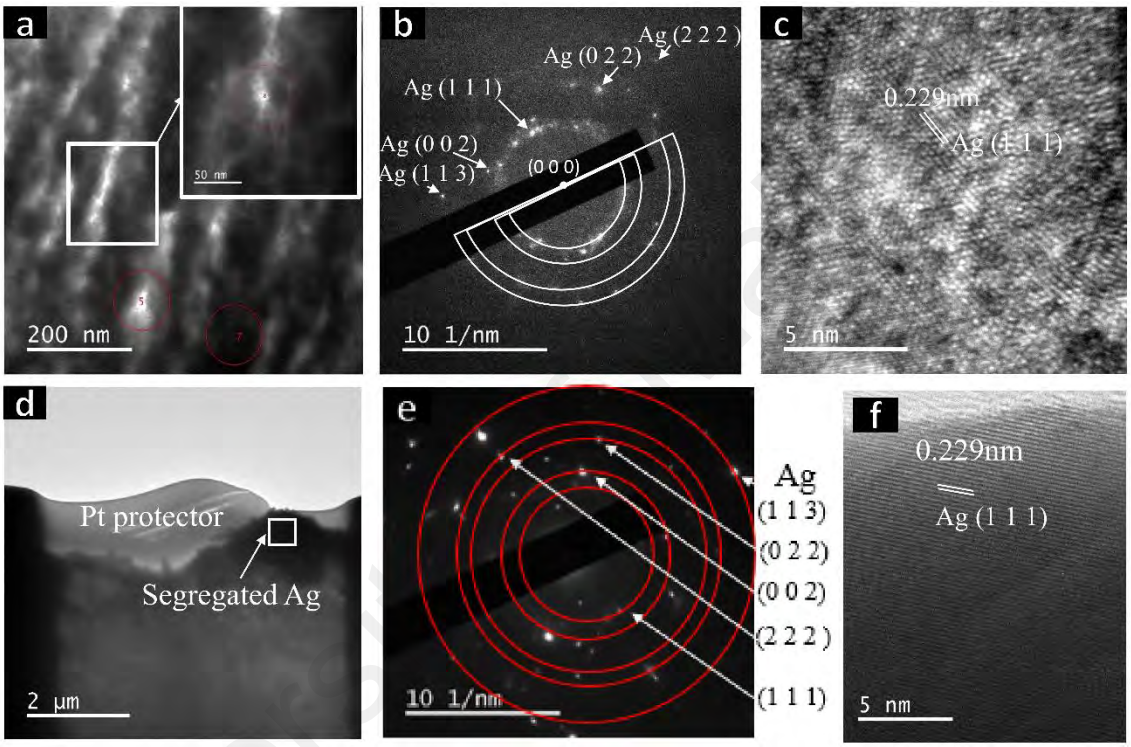


Figure 4.11: TEM image of targeted section in b (a), SAED ring pattern of targeted region in a (b), lattice image of the Ag (1 1 1) plane of the as-deposited "$S_1$" (c), TEM image of 400 °C annealed "S1" (d), SAED ring pattern of targeted region in d, and (e) lattice image of the Ag (1 1 1) for 400 °C annealed "$S_1$"

The SAED pattern of the as-deposited "$S_1$" layer confirms the presence of polycrystalline, unreacted, pristine Ag in the layer, as affirmed earlier by the XRD analysis. From the d-spacing calculation the diffraction rings can be indexed as (1 1 1), (0 0 2), (0 2 2), (1 1 3) and (2 2 2) for Ag. The lattice fringes of polycrystalline fcc Ag showing the lattice parameter of the Ag (111) plane can be seen in Figure 4.11(c). Due

to the amorphous nature of $Ta_2O_5$, its diffraction pattern could not be achieved. Similarly, a TEM image targeting the segregated Ag zone is presented in Figure 4.11(d). The SAED ring patterns of the targeted region are indexed as (1 1 3), (0 2 2), (0 0 2), (2 2 2) and (1 1 1) Ag planes. The same (1 1 1) plane for fcc Ag with the lattice parameter 0.229 nm is highlighted in Figure 4.11(f).

### 4.1.14 *In-vitro* antibacterial activity of 400 ºC annealed "$S_1$"

The antibacterial activity of the 400 ºC annealed "$S_1$" of Ag-$Ta_2O_5$ thin film was also examined. This sample demonstrated a halo inhibition zone around both *S. aureus* and *E. coli* as opposed to the uncoated SS 316L (control sample) with no halo inhibition zone (Figure 4.12). Measurements of the inhibition zone diameters across the short axis (A) and long axis (B) are given in Table 4.5. The 400 ºC annealed "$S_1$" results are (A: 13.33±0.58; B: 23.67±0.58) for *S. aureus* and (A: 12.33±1.15; B: 22.00±0.00) for *E. coli*.

.

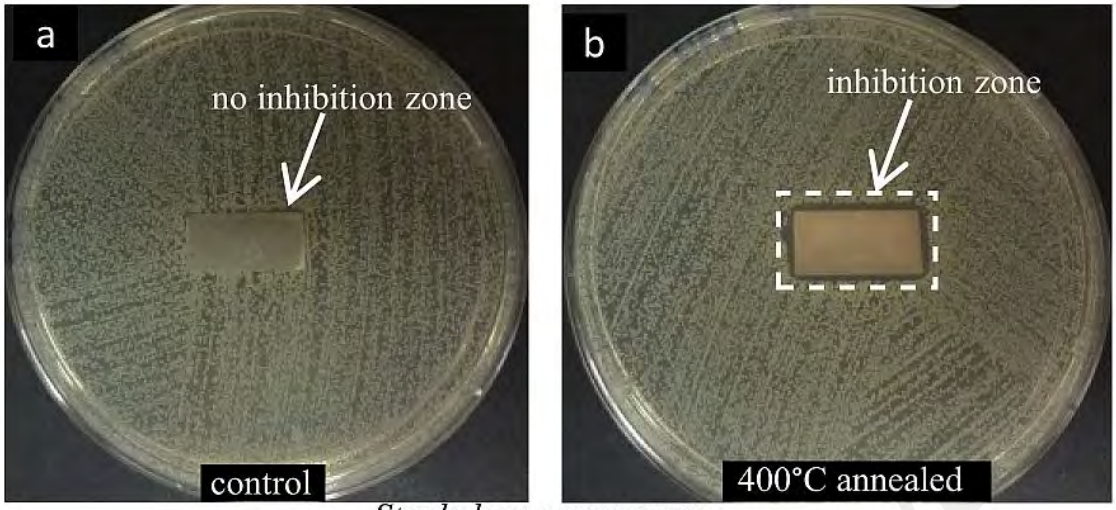


*Staphylococcus aureus*

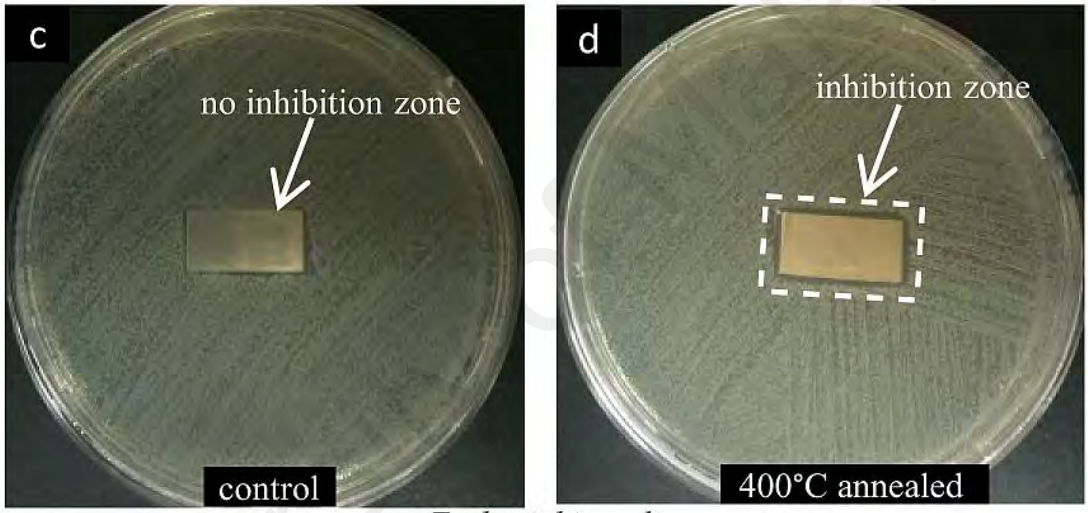


*Escherichia coli*

Figure 4.12: Halo inhibition test showing a (a,c) survived colonies of *S. aureus* and *E.coli* on the control sample, (b,d) zone of growth inhibition of of *S. aureus* and *E.coli* by 400 $^{o}$C annealed "$S_1$". The images are representative of three replicates

Table 4.6: Average inhibition zone diameter of 400 °C annealed "$S_1$" and control sample against *S.aureus* and *E.coli.*

| Test bacteria | Average inhibition zone diameter (mm) | | | |
|---|---|---|---|---|
| | Control sample (mm) | | 400 °C annealed "$S_1$" (mm) | |
| | A | B | A | B |
| Staphylococcus aureus (NCTC 6571) | No inhibition | No inhibition | 13.00 ±1.00 | 12.33 ±1.15 |
| Escherichia coli (ATCC 15597) | No inhibition | No inhibition | 23.67 ±0.58 | 22.00 ±0.58 |

### 4.1.15 Summary

The as-deposited "$S_1$" nanocomposite layer exhibited low adhesion strength and higher wettability. The annealing process improved its mechanical stability significantly. Annealing resulted in significant Ag segregation at the surface, enhanced thin film adhesion strength and limited wettability. However, the best thin film adhesion strength was achieved by annealing the as-deposited "$S_1$" at 400 °C, which may have resulted due to a compromise between excessive Ag segregation and grain growth at 500 and 600 °C. Moreover, the new phase ($AgTaO_3$) that precipitated in the "$S_1$" samples annealed at 500 and 600 °C and 5 °C/min ramp rate may have been responsible for the reduced surface integrity. However, in the 500 °C annealed "$S_1$" no $AgTaO_3$ compound formed at 2 °C/min. Unlike the control sample, the 400 °C annealed "$S_1$" acted as an antibacterial agent against the *S. aureus* and *E.coli* pathogen.

## 4.2 Method B: "$S_2$" to "$S_5$" and 400 °C annealed "$S_4$" of Ag/Ag-$Ta_2O_5$ thin films

This section represents the data analysis of the experimental results obtained with Method B. The effects of deposition power and argon flow rate, argon flow rate and substrate temperature, and thermal treatment on the microstructure of the as-deposited samples are discussed first. In the second part, the elemental composition, surface wettability, adhesion strength and phase analyses of the as-deposited samples and 400 °C annealed "$S_4$" are detailed.

### 4.2.1 The effect of power and argon flow rate on the microstructure of "$S_2$" and "$S_3$"

FESEM microstructural and elemental analyses were performed to compare the characteristics of as-deposited ("$S_2$" to "$S_5$") and annealed "$S_4$" of Ag/Ag-$Ta_2O_5$ in terms of morphology and composition. Figures 4.13(a-h) illustrate the surface morphology and cross-sectional views of the as-deposited thin film samples in different magnetron sputtering conditions. As listed in Table 3.1, in the first case "$S_2$"and "$S_3$" were prepared with different combinations of deposition power and Ar:$O_2$ gas flow rate ratio. The effects of these combinations on the surface morphology and cross-sectional microstructure were studied. A constant substrate temperature of 140 °C was used during magnetron sputtering deposition.

Sample "$S_2$", which was deposited at 200 W and Ar: $O_2$ flow rate ratio of 10:1, exhibited a homogenous distribution of Ag-$Ta_2O_5$ composite particles with the presence of irregular 0.5–20 μm bumps on the as-deposited thin film surface (Figure 4.13a). It is observed that Ag-$Ta_2O_5$ nanocomposite particles with average size of 30 nm were deposited on the surface, as shown in the magnified image in Figure 4.13(a). According to the cross-sectioned view in Figure 4.13(b), the high ratio of Ar:$O_2$ (10:1) is believed to have been accounts for the formation of a tilted columnar microstructure with

randomly arranged geometry at the very top surface of the film. The high Ar flow rate may be attributed to the higher sputtering rate due to the high ionization fraction (Stan et al., 2010). Thus, it is proposed that the energetic ion fraction promoted the imbalance of incoming particles as a result of the super high kinetic energy and consequent glancing angle of the particles (Dervaux et al., 2017; Loch & Ehiasarian, 2016). In this way, the 60 ° tilted columnar morphology grew (Figure 4.13(b)).

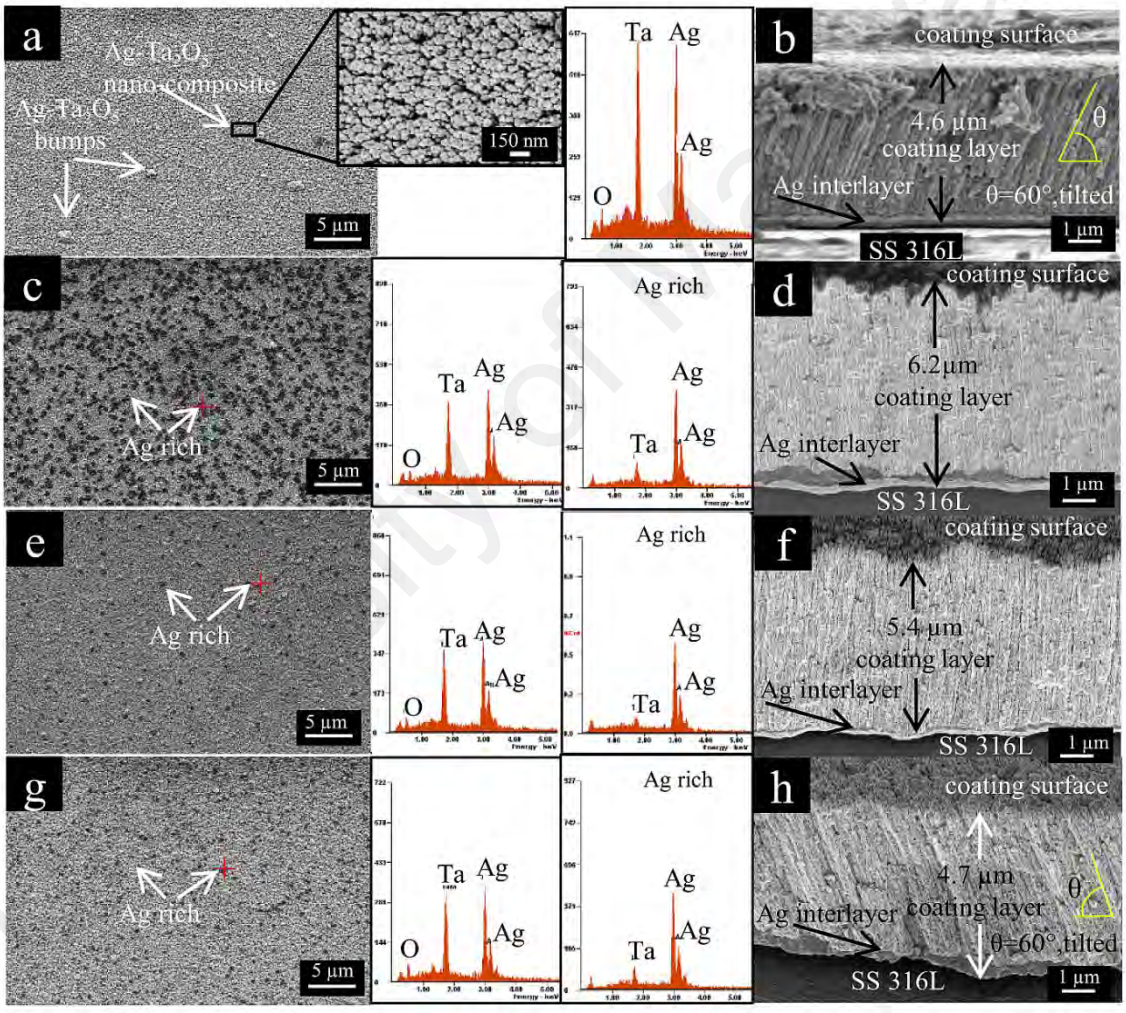


Figure 4.13**:** (a, b) FESEM surface morphology, EDX and cross-section views of as-deposited "$S_2$"; (c, d) "$S_3$" ; (e, f) "$S_4$"; and (g, h) "$S_5$", respectively, of Ag/Ag-$Ta_2O_5$ thin film

For "$S_3$" exposed to DC/RF of 300 W and Ar:$O_2$ flow rate ratio of 5:1, Ag particle segregation became dominant. Ag particles strongly tended to segregate on the composite surface because Ag has a higher deposition rate than Ta. Figure 4.13(c) shows that the increasing deposition power facilitated microstructural change. During equilibrium deposition, the Ag and Ta particles were continuously depositing. But towards the end of the deposition process, Ag mobility was unrestricted and continued moving over the surface as agglomerated Ag (Velasco et al., 2016). As observed in Figure 4.13(d), the cross-sectional image of "$S_3$" indicates a perpendicular columnar pattern along the coating layer that resulted from the low ratio of Ar:$O_2$ (5:1). This first case shows that the deposition power affected the surface morphology and the Ar:$O_2$ ratio was more significant.

### 4.2.2 The effect of Ar:$O_2$ flow rate ratio and substrate temperature on the microstructure of "$S_4$" and "$S_5$"

Since "$S_3$" exhibited uniform surface morphology, the deposition power was kept at 300 W for the second case as well. The Ar:$O_2$ gas flow rate ratio and substrate temperature of "$S_4$" and "$S_5$" were varied (Table 3.1) in order to observe their effects on surface morphology and cross-sectional microstructure. As shown in Figures 4.13(c, e & g), the compactness pattern of the surface morphology increased with increasing substrate temperature. The highest substrate temperature induced the volatilization of the arriving sputtered particles. Hence, these particles acquired enough energy to diffuse into the substrate (Li et al., 2009). Moreover, the Ag particles appeared in all sets of as-deposited "$S_3$", "$S_4$" and "$S_5$" samples with 6.2±0.3, 5.5±0.3 and 4.7±0.2 µm thickness, respectively, and which were deposited at a constant 300 W. In addition, a finer columnar structure that formed perpendicular to the substrate's surface was generated on "$S_3$" and "$S_4$" at low and medium (5.0:1 and 7.5:1) Ar:$O_2$ flow rate ratios. The

perpendicular coating growth on the top surface was instigated by the lower mobility of the arriving particles. The particles were not as mobile as the particles in $S_2$, which yielded a stable motion of arriving particles along the sputter flux (Loch & Ehiasarian, 2016). According to Figure 4.13(h) corresponding to "$S_5$", the 60 ° tilted columnar microstructure was influenced by the high Ar content. This result is similar to the "$S_2$" surface obtained with Ar flow rate of 60 sccm and 200 W in Figure 4.13(b). For this second case it can be concluded that the substrate temperature has a significant effect on surface morphology, while the Ar:$O_2$ ratio has an effect similar to the first case.

### 4.2.3 The effect of thermal treatment on the microstructure of "$S_4$"

After annealing the as-deposited "$S_4$" at 400 °C (400 °C annealed $S_4$), Ag segregation and agglomeration were distinguishable at the surface of the Ag/Ag-$Ta_2O_5$ nanocomposite film. This kind of Ag segregation resembles the so-called land-lake shape (Figures 4.14(a-c)). The thermal temperature supplied in the annealing process was sufficient to enhance the kinetic energy of the Ag particles, which was responsible for diffusing Ag to the surface and crystallizing the segregated Ag particles. However, although this energy state was not adequate for $Ta_2O_5$ migration, it still triggered the diffusion of Ag particles to the surface. The Ag particles diffused to the surface also on account of the chemical potential, surface energy and strain energy (Velasco et al., 2016). The low reactivity of Ag with the $Ta_2O_5$ ceramic in the as-deposited "$S_4$" yielded poor Ag-$Ta_2O_5$ bonds. This type of relation is potentiated by the columnar morphology of PVD films and the mismatch of thermal expansion between film and substrate, thus allowing Ag diffusion and influencing segregation (Bunting & Cheung, 2016).

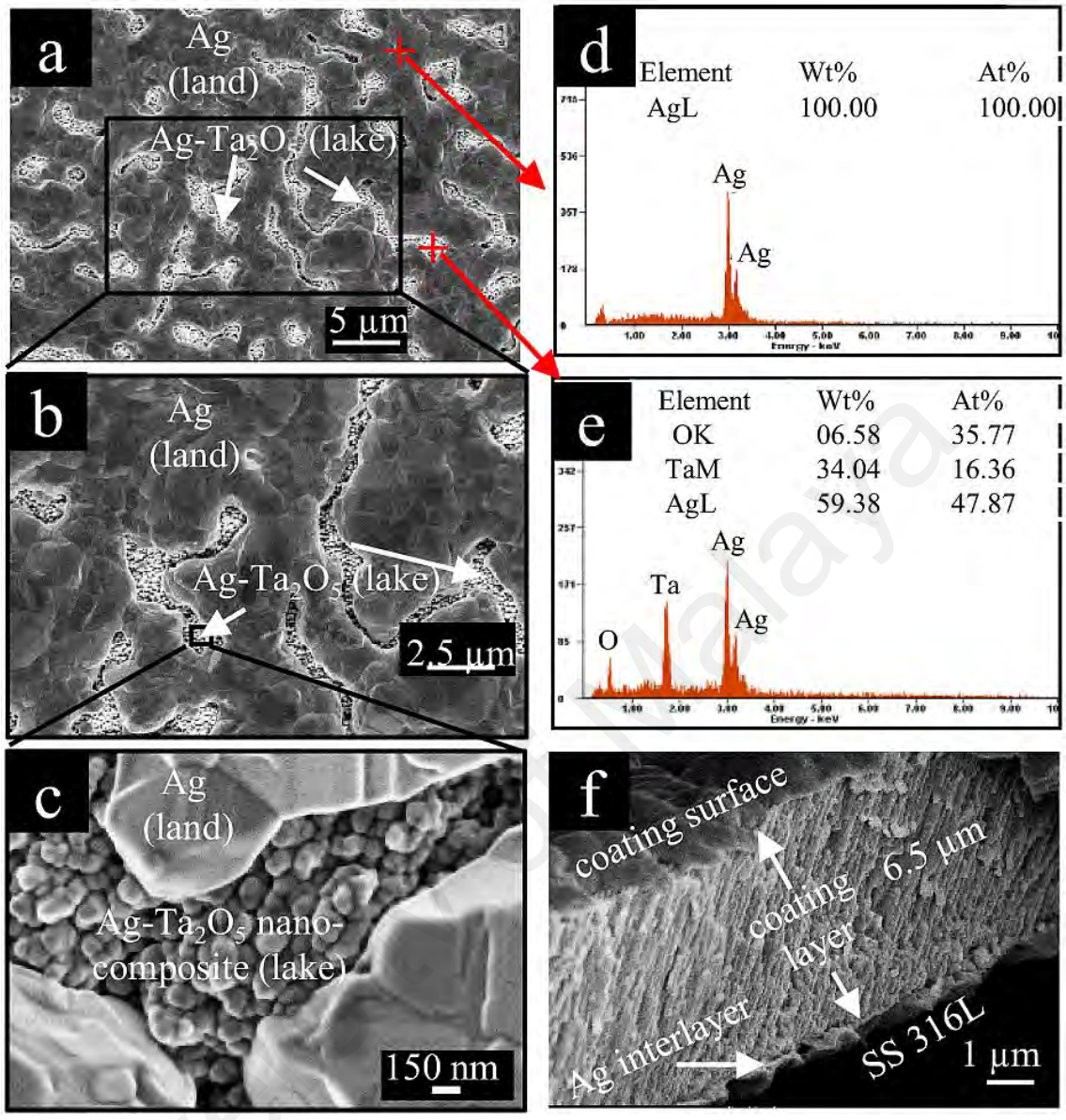


Figure 4.14**:** (a) FESEM surface morphology, (b) magnified view of square box from (a), (c) nano particle size of magnified view of square box from (b), (d) EDS spectrum at point 1 of land area (e) EDS spectrum at point 2 of lake area (f) cross sectional view of 400 °C annealed "$S_4$"

The columnar-like morphology facilitated a smooth path, while the thermal expansion mismatch incorporated the strain energy into the film system. This combination induced the Ag segregation process. The annealing treatment changed the coating thickness to 6.5±0.1 µm due to the formation of porosity in the layer below. The magnified square

box of the lake shape in Figure 4.14(b) revealed that 50–80 nm Ag-$Ta_2O_5$ nanocomposite assembled on the surface of the 400 °C annealed "$S_4$" as shown in Figure 4.14(c). The nanosize Ag-$Ta_2O_5$ composite at the surface of the as-deposited "$S_4$" and 400 °C annealed "$S_4$" is highly favorable for interaction with micron-size bacteria.

### 4.2.4 EDX of "$S_2$" to "$S_5$" and 400 °C annealed "$S_4$"

The EDX measurements of the surfaces of all as-deposited Ag/Ag-$Ta_2O_5$ thin films indicate that Ag, Ta and O were successfully deposited, with Ag as the major element (Table 4.6). This indicates the absence of contamination during PVD and annealing. In the case of the 400 °C annealed "$S_4$", 100 % of the Ag element was observed in the "land" area, confirming Ag segregation on the surface. In the "lake" area, the oxygen percentage as an indication of an oxide layer increased up to 6.58 %, which suggests the occurrence of oxidation due to the residual $O_2$ in the annealing furnace.

Table 4.7: EDX of multilayer as-deposited samples as well as 400 °C annealed "$S_4$"

| Samples | | Elemental composition (weight %) | | |
|---|---|---|---|---|
| | | Ag | Ta | O |
| "$S_2$" | | 55.1 | 42.29 | 2.61 |
| "$S_3$" | | 60.11 | 37.00 | 2.89 |
| "$S_3$" | Ag rich | 85.03 | 14.97 | |
| "$S_4$" | | 58.65 | 39.01 | 2.34 |
| "$S_4$" | Ag rich | 90.31 | 9.69 | |
| "$S_5$" | | 54.99 | 41.93 | 3.08 |
| "$S_5$" | Ag rich | 86.39 | 13.61 | |

Table 4.7 continued: EDX of multilayer as-deposited samples as well as 400 °C annealed "$S_4$"

| | | | | |
|---|---|---|---|---|
| 400 °C annealed "$S_4$" | Land area | 100 | - | - |
| 400 °C annealed "$S_4$" | Lake area | 59.38 | 34.04 | 6.58 |

### 4.2.5 Surface wettability of "$S_2$" to "$S_5$" and 400 °C annealed "$S_4$"

Figures 4.15 indicate that the contact angles of SS 316L and as-deposited "$S_2$" to "$S_5$" were 41.5±3.2 °, 45.6±1.1 °, 45.7±3.5 °, 43.4±3.3 ° and 68.1±0.7 ° respectively. The contact angle increased drastically to 101.2±0.9 ° after heat treating the "$S_4$" thin film. This suggests that surface wetting after deposition and annealing was more favorable, whereby the hydrophobic properties of the crystallized Ag/Ag-$Ta_2O_5$ coating improved more than two-fold those of SS 316L.

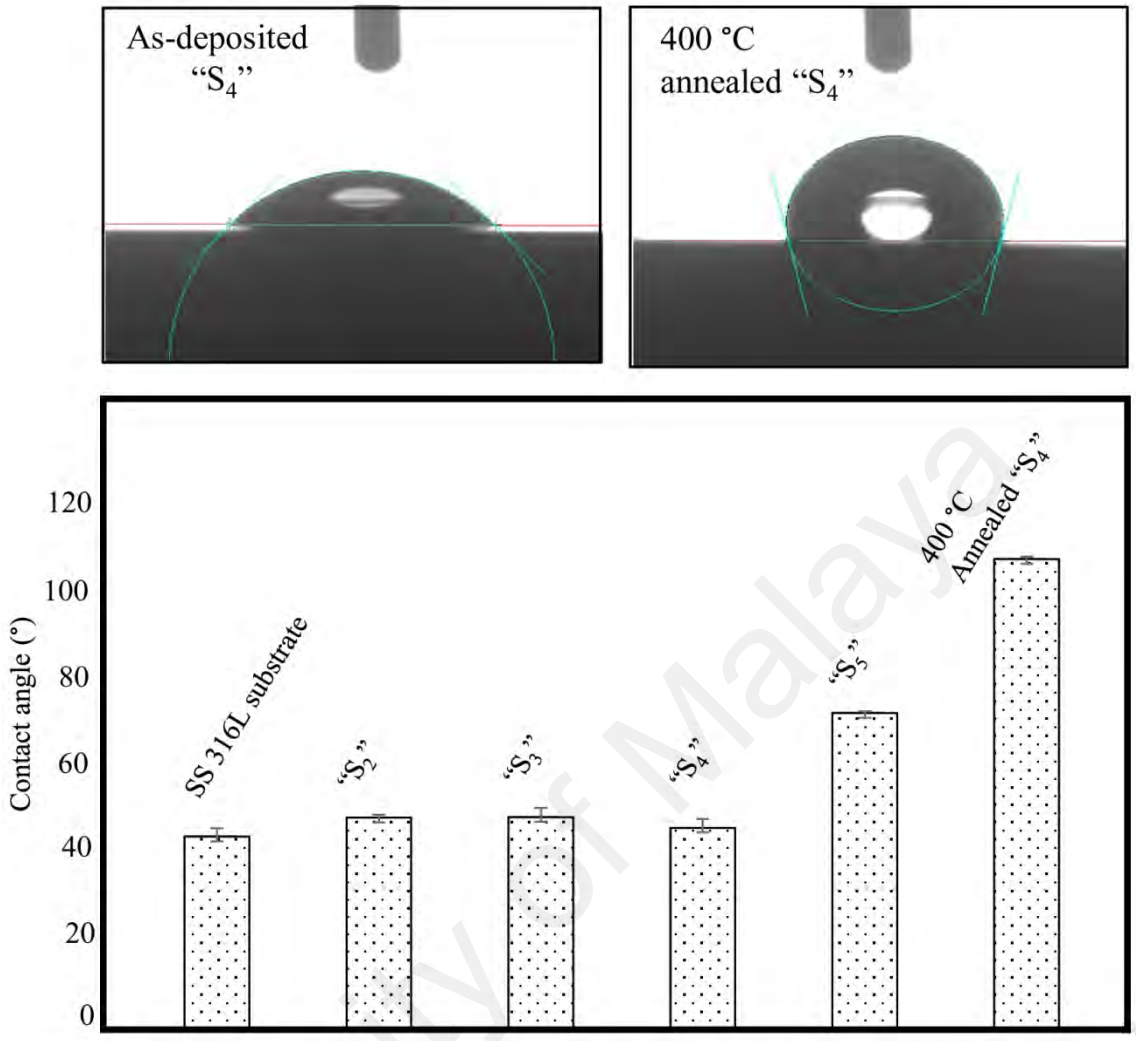


Figure 4.15: Contact angle on the SS 316L bare substrate, as-deposited "$S_2$" to "$S_5$" and 400 °C annealed "$S_4$" of Ag/Ag-$Ta_2O_5$ thin film

### 4.2.6 Adhesion strength and hardness of "$S_2$" to "$S_5$" and 400 °C annealed "$S_4$"

Table 4.8 summarizes the thin film adhesion and hardness results of as-deposited "$S_2$" to "$S_5$" and 400 °C annealed "$S_4$". Sample "$S_4$" was selected for annealing at 400 °C due to its comparatively better adhesion strength.

Table 4.8: Thin film adhesion strength and hardness values of as-deposited samples and 400 °C annealed "$S_4$" of Ag/Ag-$Ta_2O_5$ thin films

| Samples | Critical load (mN) | Hardness ($Hv_{0.3}$) |
|---|---|---|
| "$S_2$" | 777 ±37 | 129 ±1 |
| "$S_3$" | 1022 ±75 | 146 ±0 |
| "$S_4$" | 1159 ±126 | 145 ±0 |
| "$S_5$" | 916 ±128 | 151 ±0 |
| 400 °C annealed "$S_4$" | 2916 ±147 | 156 ±1 |

According to the adhesion strength results of as-deposited "$S_2$" to "$S_5$" with different magnetron sputtering parameters, the optimum combination of 300 W DC and RF, 7.5:1 argon-oxygen flow rate ratio and 250 °C substrate temperature yielded the highest adhesion strength of 1159 ±126 mN ("$S_4$"). The adhesion strength in this study was significantly higher than that in a study by Rahmati et al. (2015b), who reported 713 mN for as-deposited Ta/TaO thin film coated on titanium alloy. In the present study, the improved adhesion strength can be attributed to the multilayer Ag-$Ta_2O_5$ nanocomposite's intrinsic behavior. The optimum adhesion result achieved for $S_4$ shows that the ideal combination of parameters is key to enhanced adhesion strength (Bushroa et al., 2011; Sarraf et al., 2016). After annealing the "$S_4$" at 400 °C annealing temperature, the adhesion strength increases up to 2916 ±147 mN.

The corresponding graphs of depth (I), load (II) and friction (III) versus distance as well as the sample's failure points during the scratch experiments are presented in Figure 4.16. The failure points of the as-deposited "$S_4$" and 400 °C annealed "$S_4$" are labelled accordingly in the figure.

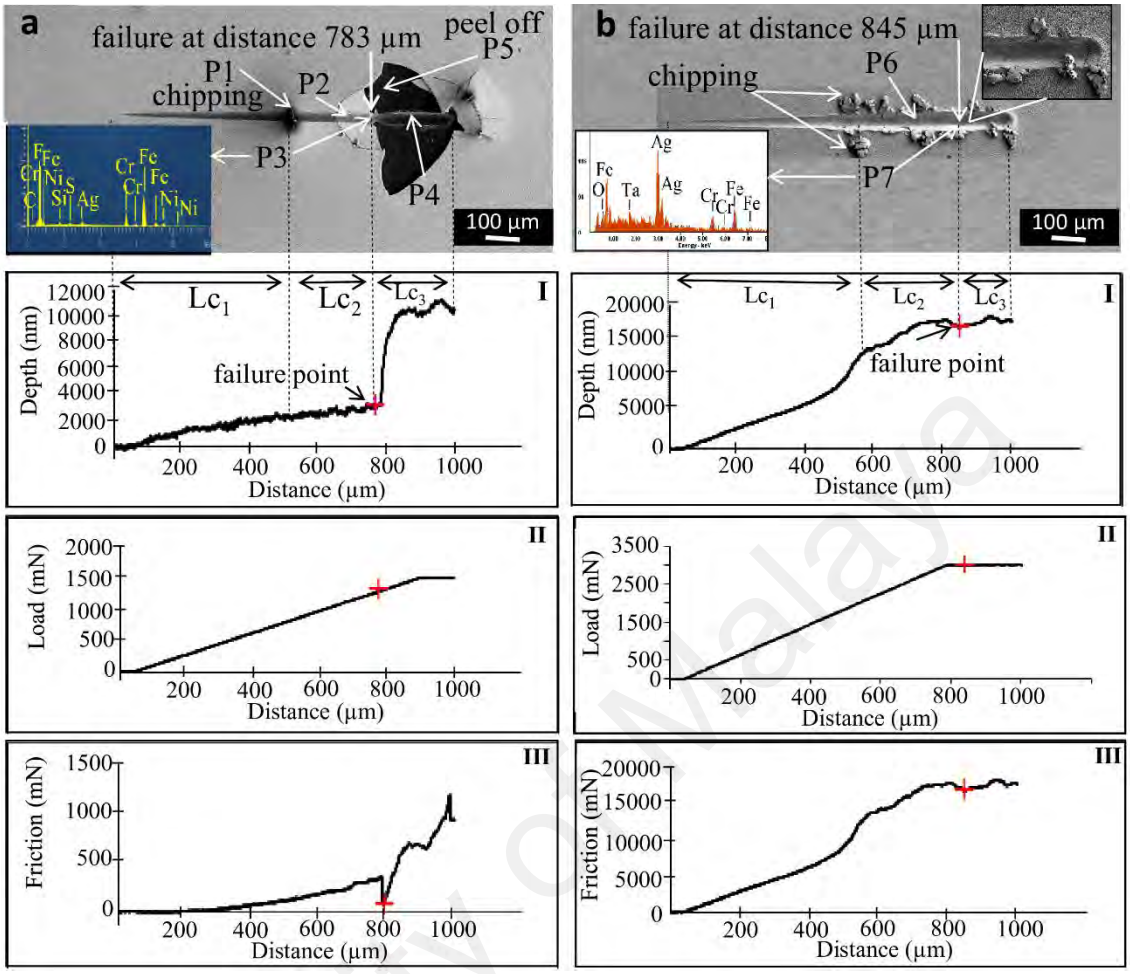


Figure 4.16: FESEM images from scratch testing and EDX analysis of (a) as-deposited "$S_4$" and (b) 400 °C annealed "$S_4$" followed by the respective adhesion strength analyses (depth and load versus distance graphs)

According to Figure 4.16(a), when the load was gradually increased, chipping of the coating was observed before failure at a distance of 783 µm. At this point, it took a load of 1300 mN to delaminate the coating layer from the 316L stainless steel substrate. Because such extensive load can cause the coating to peel off from the substrate, the steel substrate surface will be exposed at the end of the scratch track. In the 400 °C annealed "$S_4$", failure was initiated when chipping appeared on both tracksides. When the load was increased, the thin film delaminated from the substrate at a distance of 845 µm. It is determined in this study that failure is inevitable when the load reaches 3001

mN. The elemental analysis (wt.%) of seven spectra corresponding to the FESEM micrograph images of the surface scratches on as-deposited "$S_4$" and 400 °C annealed "$S_4$" is summarized in Table 4.9.

Table 4.9: Elemental analysis of seven point corresponding to FESEM surface scratch images (Figure 7) of as-deposited "$S_4$" (P1- P5) and 400 °C annealed "$S_4$" (P6-P7)

| Point | Elemental composition (weight %) | | | | | | | | | |
|---|---|---|---|---|---|---|---|---|---|---|
| | Coating elements | | | Substrate elements | | | | | | |
| | Ag | Ta | O | C | Fe | Cr | Ni | Mo | S | Si |
| P1 | 65.7 | 27.1 | 3.8 | - | - | - | - | - | - | - |
| P2 | 65.5 | 29.5 | 2.0 | 3.0 | - | - | - | - | - | - |
| P3 | - | - | - | 3.4 | 67.2 | 17.2 | 9.7 | 2.5 | - | - |
| P4 | 4.5 | - | - | 3.4 | 62.3 | 16.0 | 10.8 | 1.8 | 0.5 | 0.8 |
| P5 | - | - | - | | 65.9 | 17.6 | 8.7 | 2.0 | 1.9 | 0.5 |
| P6 | 60.96 | 34.93 | 4.11 | - | - | - | - | - | - | - |
| P7 | 41.81 | 3.15 | - | - | 40.60 | 14.44 | - | - | - | - |

At the chipping area (site) designated as point P1, the EDS analysis revealed the absence of substrate elements but the coating contained 65.7 % Ag, 27.1 % Ta and 5.2 % O. Due to chipping, 3 % C was detected at P2, which marked the initiation of coating removal. Point P3 is recognized as the point where failure began after applying a scratch distance of 783 μm, which is equivalent to a critical load of 1300 mN. However, the EDS of P4 shows the presence of 4.5 % Ag because the Ag interfacial layer was not completely removed under 1300 mN load. A minor balance of Ag element at P4

suggests that the bond between the Ag interlayer and Ag-$Ta_2O_5$ coating layer was not as strong as the bond between the Ag interlayer and 316L stainless steel substrate. In terms of ionic or covalent chemical bonds, it is known that the atomic bond configuration of ceramic is different from metal. The outermost electron configuration of ceramic material is extremely stable compared to that of metallic material. Therefore, it is not surprising that it is difficult to achieve stable bonding between ceramic and metallic atoms (Uday et al., 2016). At this point, the entire Ag/Ag-$Ta_2O_5$ coating was completely removed.

For the 400 °C annealed "$S_4$", the elemental analysis in Table 4.9 reveals that the coating elements at spectrum P6 comprised 60.96 % Ag, 34.93 % Ta and 4.11 % O. The absence of substrate elements indicates that coating failure had not yet occurred. Point P7 reflects that actual failure took place at a distance of 845 μm and load of 3001 mN, where the annealed coating was delaminated. At this particular point, traces of Fe and Cr from the substrate and Ag and Ta elements from the coating were detected. However, 42.53 % Ag, 3.94 % and 1.7 2% Ta were still detected in the coating's scratch track. This could be attributed to the fact that heat treatment promoted the diffusion of coating elements into the substrate surface, which inevitably improved the magnitude of adhesion (Stan et al., 2009; Stan et al., 2013). where heat treatment affected the adhesion strength of the Ag/Ag-$Ta_2O_5$ coating. Annealing at 400 °C yielded the best coating characteristics suitable for target applications.

### 4.2.7 Phase Analysis of "$S_2$" to "$S_5$" and 400 °C annealed "$S_4$"

Figure 4.17 illustrates the XRD pattern of the as-deposited multilayer Ag/Ag-$Ta_2O_5$ thin film samples referred to as-deposited "$S_2$" to "$S_5$" as well as the 400 °C annealed "$S_4$". All four as-deposited thin films displayed a similar Bragg diffraction angle position for each noticeable peak. No peak shift was observed due to the equal lattice parameter size

in the crystallographic system of all thin film samples (Chuang et al., 2017). Ag peaks appeared at position $2\theta$ of 38.12, 44.40, 64.51, 77.36 and 81.55 °. Meanwhile, the orientations of the associated cubic crystal planes were identified as (1 1 1), (0 0 2), (0 2 2), (1 1 3) and (2 2 2), respectively, consistent with the standard data file ICSD No. (98-004- 4387).

By observing the diffracted peaks at $2\theta$ of 38.12 to 81.55 ° for all as-deposited thin film samples, it is evident that both Ag and $Ta_2O_5$ ceramic phases in the thin film crystalized poorly (Figure 4.17**).** Other studies support this finding (Chiu et al., 2014; Varlashkin, 2011).

The Ag particles segregated at the surface and crystallization was achieved after annealing. Consequently, the Ag peak changed abruptly to a sharper and narrower diffraction peak. The significant increase in the XRD pattern peak intensity for the 400 °C annealed "$S_4$" (Figure 4.17) suggests the highest adhesion strength. This indicates the segregation of Ag particles, which is further verified by the FESEM surface microstructure in Figure 4.13(a).

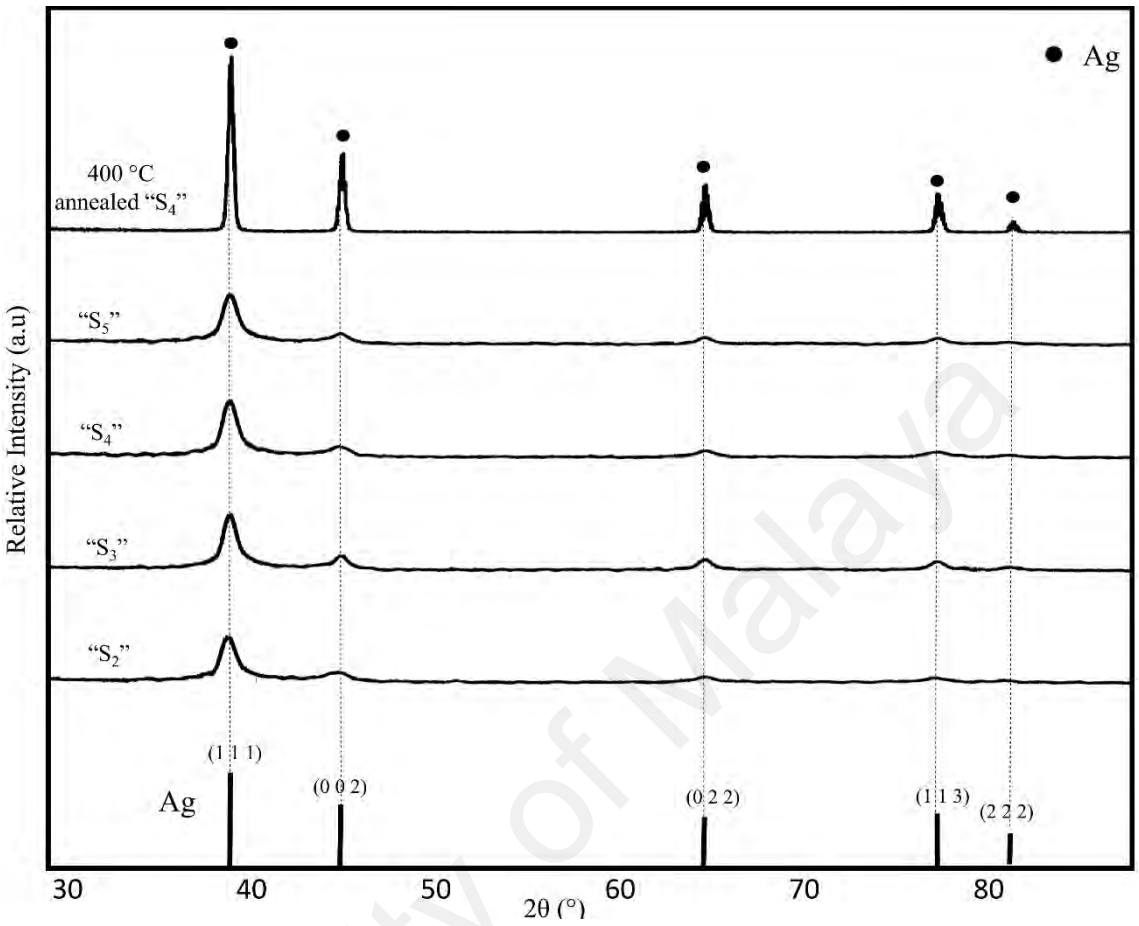


Figure 4.17: XRD diffraction patterns of Ag/Ag-$Ta_2O_5$ thin film as-deposited and 400 °C annealed "$S_4$"

### 4.2.8 Summary

The power, argon flow rate and substrate temperature affected the thin film morphology in terms of Ag distribution, cross-sectional structure and compactness, respectively. The optimum conditions for the morphology of as-deposited PVD multilayer Ag/Ag-$Ta_2O_5$ on SS 316L yielded an adhesion strength of 1159±126 mN (as-deposited "$S_4$"). The bonding between the amorphous structure and SS 316L substrate improved extensively (by about 152 %) up to 2916±147 mN after annealing at 400 °C. It was found that the optimal coating surface provided a relatively homogenous annealing microstructure. Ag

segregation, phase transformation and wettability improved by the as-deposited "$S_4$". Segregated Ag and a coarser coating structure were observed in the crystalized sample.

### 4.3 Method C: "$S_6$" to "$S_{10}$" and annealed "$S_7$" of Ag/Ag-$Ta_2O_5$ thin films

This section presents the data analysis of the experimental results obtained with Method C. The surface microstructure, cross-sectional microstructure, surface wettability, adhesion strength and phase analysis of as-deposited "$S_6$" to "$S_{10}$" and annealed "$S_7$" (250-850 °C) thin films are evaluated. Then the nanoindentation test of the as-deposited "$S_7$" and annealed "$S_7$" samples is elaborated. The surface chemistry of as-deposited "$S_7$" and 400 °C annealed "$S_7$" is subsequently discussed. The antibacterial performance and biocompatibility roperties of the 400 and 700 °C annealed "$S_7$" samples is discussed in the last part.

#### 4.3.1 Surface and cross-sectional microstructure analysis of "$S_6$" to "$S_{10}$"

Figures 4.18(a-f) show images of the surface morphology and cross-sectional views of the as-deposited "$S_6$" to "$S_8$" sputtered at 100-300 W deposition power.

It is evident sputtering power affected the films' surface morphology significantly (Figures 4.18(a, c & e)). According to Figure 4.18, both deposited particle size and film roughness increased with increasing deposition power. "$S_6$", "$S_7$" and "$S_8$" all exhibited homogenous surface morphology. "$S_6$", which was deposited at 100 W, exhibited a small individually Ag and $Ta_2O_5$ nanoparticles at the thin film surface (Figure 4.18(a)).

When the DC and RF were increased to 200 and 300 W, the surface roughness increased and the particles deposited on the surface of "$S_7$" and "$S_8$" were larger (Figures 4.18(c & e)). It is speculated that increasing the deposition power from 200 to 300 W provided the deposition particles more kinetic energy. These particles had a better opportunity to arrive and deposit on the substrate, and a non-equilibrium process

of arrival ensued, which led to larger deposited particles (Lu et al., 2001; Waykar et al., 2016). Furthermore, in Figures 4.18(c,e) it is evident that the film compactness also increased with rising deposition power, especially when comparing "$S_7$" and "$S_8$" (Figure 4.18(a)).

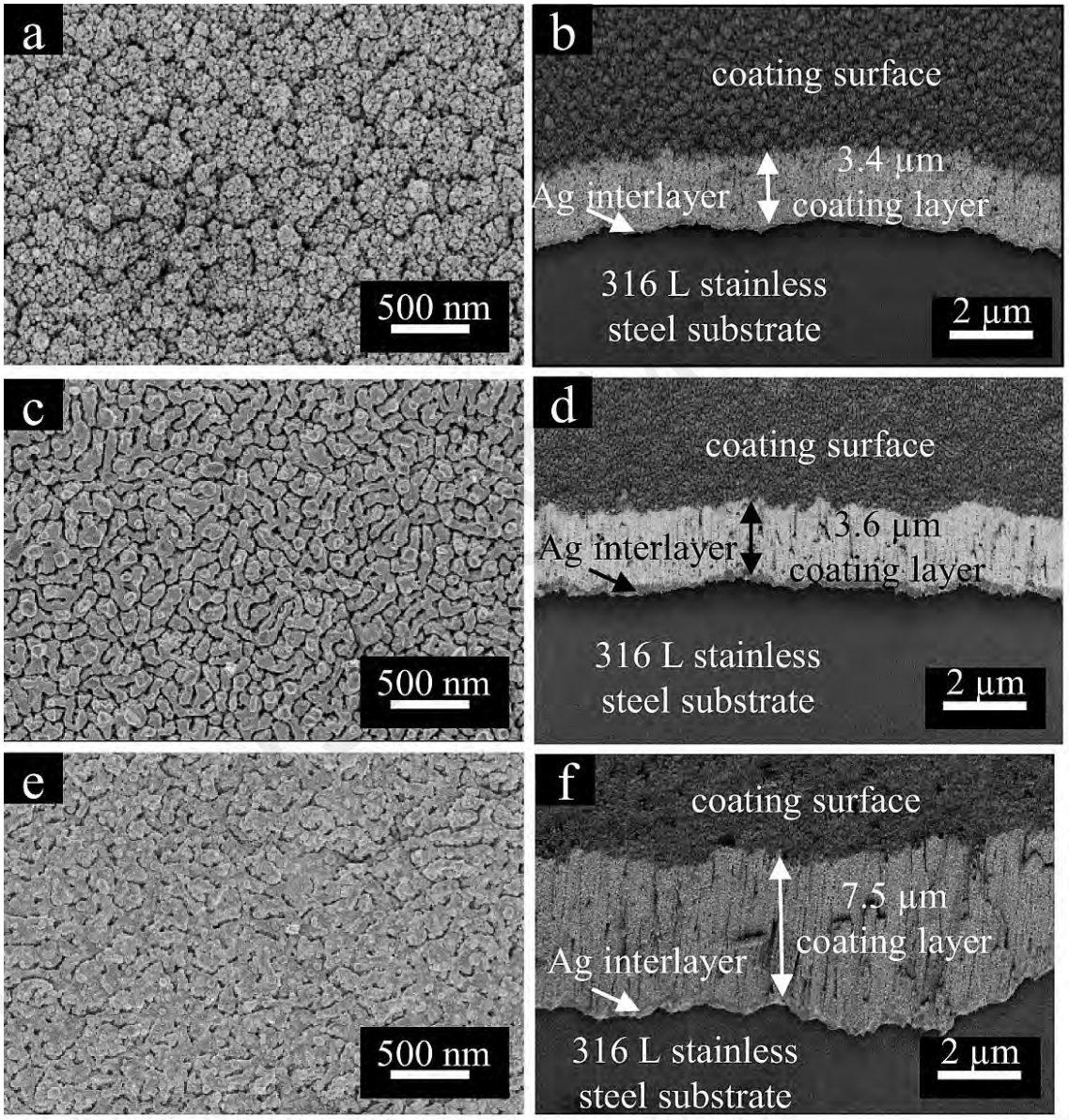


Figure 4.18**:** FESEM surface morphology and cross sectional views of as-deposited films sputtered with power of (a,b) 100 W ("$S_6$"), (c,d) 200 W ("$S_7$"), (e,f) 300 W ("$S_8$")

The increased deposition rate as a consequence of greater deposition power generated a higher ionization fraction. Accordingly, film densification ensued from the energized particles' competition to reach the substrate (Lin et al., 2004; Loch & Ehiasarian, 2016).

The cross-sectional morphology of as-deposited "$S_6$" to "$S_8$" shown in Figures 4.18(b, d & f) indicates an increasing trend in the columnar structure, columnar compactness and coating thickness (3.4±0.2, 3.5±0.1, 6.8±0.7 μm respectively) due to the high deposition rate as explained previously.

The wide range of change in substrate temperature was responsible for the typical morphologies of "$S_9$" to "$S_{10}$" (Figure 4.19). In ambient condition, 30-50 nm Ag particles distributed on the less adherent textured film surface. Figure 4.19(a) reflects the lowest adhesion strength for $S_9$, which is also given in Table 4.9. This kind of surface morphology forms due to the poor volatilization of particles arriving without heat (Li et al., 2009). This notion is in agreement with the loose cross-sectional morphology seen in Figure 4.19(b).

With the substrate temperature increasing to 150 °C, the deposited particles had enough energy to diffuse, resulting in the formation of a more compact film (Figure 4.19(c)). In addition, adequate movement of the deposited particles was important for nucleation repetition to form smaller granular particles, as FESEM revealed. However, as the substrate temperature was further increased to 250 °C, the particles' mobility amplified. The deposited particles tended to aggregate due to the higher nucleation rate. Thus, it is speculated that the nuclei grew in response to the higher nucleation rate and larger spherocylinder-shape particles (Figure 4.19(d)) (Kumar et al., 2017b; Liu & Xiang, 2014).

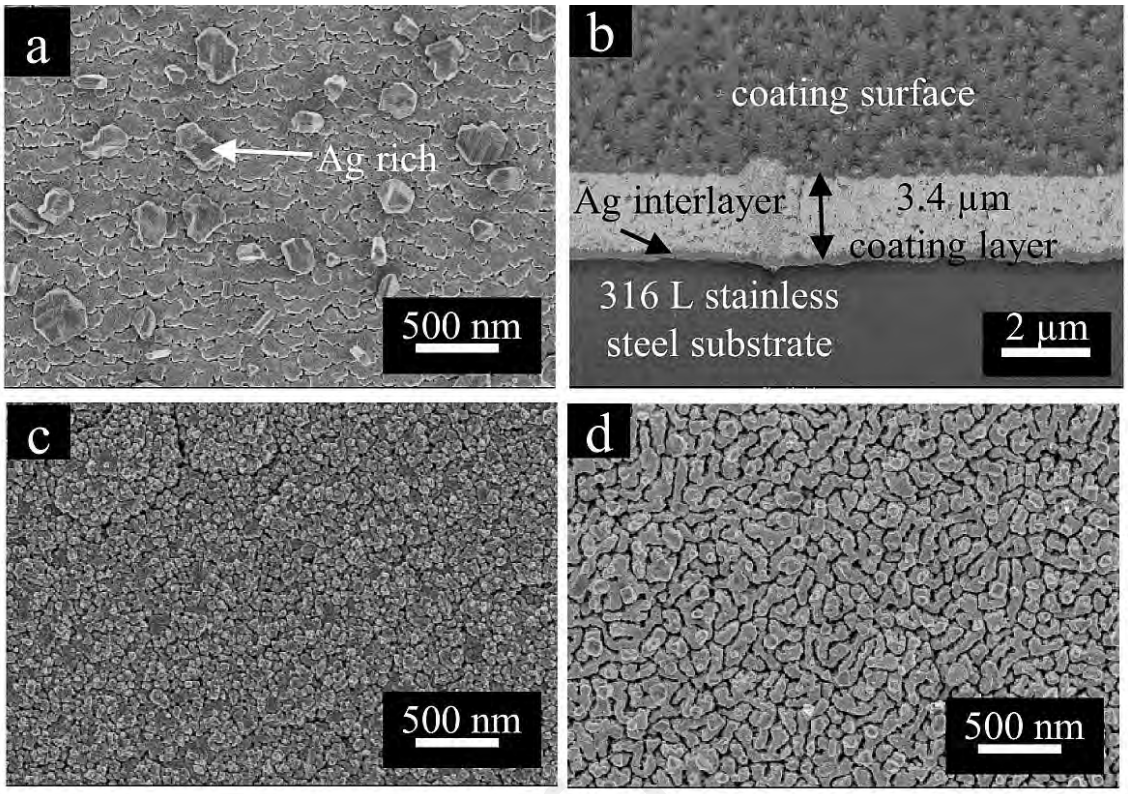


Figure 4.19: FESEM surface morphology of as-deposited films at substrate temperature (a) "$S_9$" (ambient), with its (b) cross sectional views (c) "$S_{10}$" (150 °C) and (d) "$S_7$" (250 °C)

### 4.3.2 Evolution of surface and cross-sectional morphology of "$S_7$" as a function of annealing temperatures

Figure 4.20 illustrates the evolution of surface morphology of as-deposited "$S_7$" (a) and when annealed from 250 – 850 °C (b-i).

Figure 4.21 presents the cross-sectional morphology of as-deposited "$S_7$" (a) and annealed "$S_7$" (b-f). It is noted that the coating layer thickness increased as a function of annealing temperature. The thicknesses of "$S_7$" annealed at 250, 400, 550, 700 and 850 °C were 3.5±0.1, 6.5±0.2, 7.8±0.1, 9.4±0.9, 9.7±1.0 and 12.0±1.0 µm, respectively.

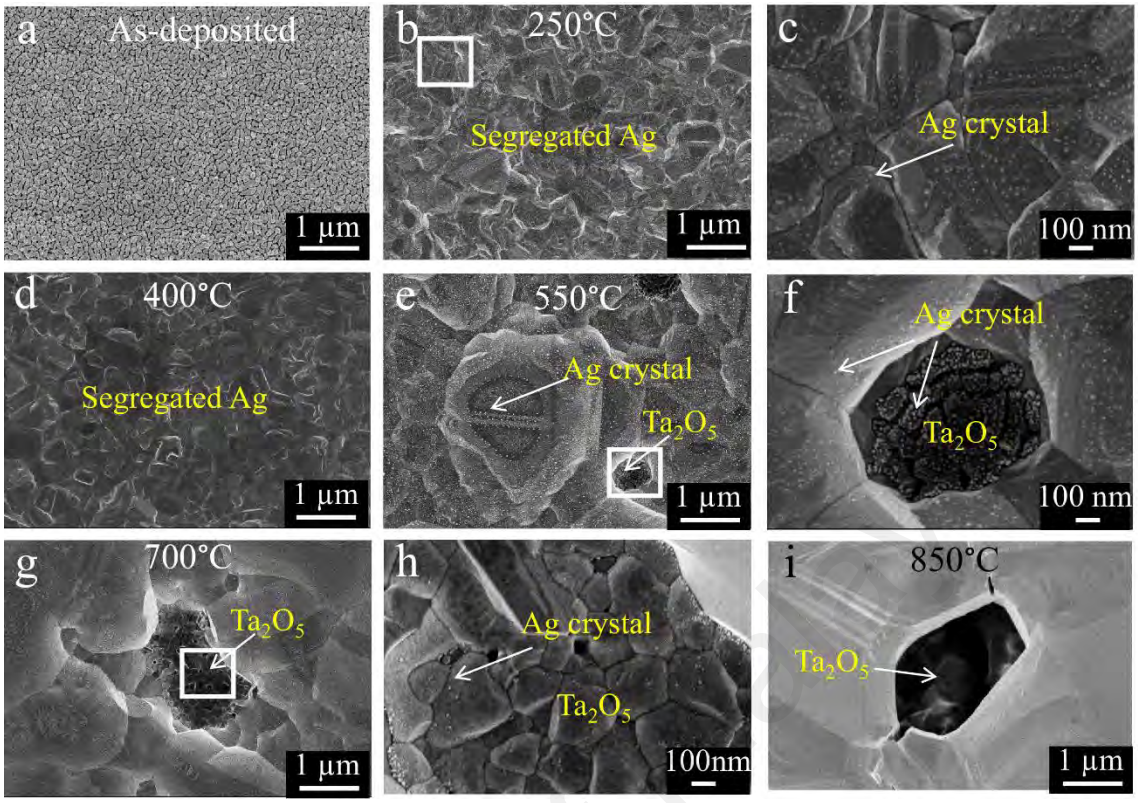


Figure 4.20: FESEM surface morphology of Ag/Ag-$Ta_2O_5$ thin film sample "$S_7$" (a) as-deposited; and annealed at (b) 250, (c) magnified view of square box from b,(d) 400, (e) 550, (f) magnified view of square box from e (g) 700, (h) magnified view of square box from g and (i) 850 °C

The FESEM morphological analysis in Figure 4.20(a) reveals a homogenously distributed nanocomposite film over the as-deposited specimen surface. At 250 °C, the thermal energy was sufficient to trigger AgNPs diffusion. The AgNPs that have low reactivity with the bulk exhibited enhanced diffusion to the surface. Moreover, the higher surface energy of the AgNPs influenced the mobility of these particles, which segregated to the surface (Figure 4.20) and aided the columnar structure (Figure 4.21(a)). The highlighted section in Figure 4.20(b) was selected to present the high-magnification FESEM view in Figure 4.20(c). The prominent AgNPs islands were distributed over the Ag-segregated surface. The AgNPs indicate that crystal nucleation

occurred. This segregation consequently interrupted the columnar growth (Figure 4.21(b)). However, upon annealing at 400 °C, all AgNPs islands that coalesced at the surface (Figure 4.20(d)) formed an entirely segregated Ag surface.

As the temperature was increased to 550 °C, the particles coarsened (Figure 4.20(e)), which is an enhanced Ostwald ripening process. The appearance of AgNPs strengthens the idea that Ag actively migrated from the bulk. This enabled potential grain boundary diffusion and recrystallization to occur at this annealing temperature. In a recent study, a significant morphological evolution was observed when the AgNPs were annealed up to 550 °C (Pandey et al., 2018). According to Figure 4.20(e) the $Ta_2O_5$ had potential to escape to the surface due to the increased kinetic energy in the entire coating. In addition, the availability of diffusion paths created by the previously diffused AgNPs enhanced the migration of the residual AgNPs (in the bulk coating) and $Ta_2O_5$ to the surface. The migration is also visible in the cross-sectional view in Figure 4.21(d). The majority of $Ta_2O_5$ segregated in the region near surface, while the remaining $Ta_2O_5$ successfully escaped to the surface. Figure 4.21(c) shows there was no $Ta_2O_5$ migration, reflecting insufficient thermal supply. The highlighted section in Figure 4.20(e) of $Ta_2O_5$ morphology was selected for the high-magnification FESEM view presented in Figure 4.20(f). It is obvious that the AgNPs preferred to distribute on the $Ta_2O_5$ surface to release the greater surface energy.

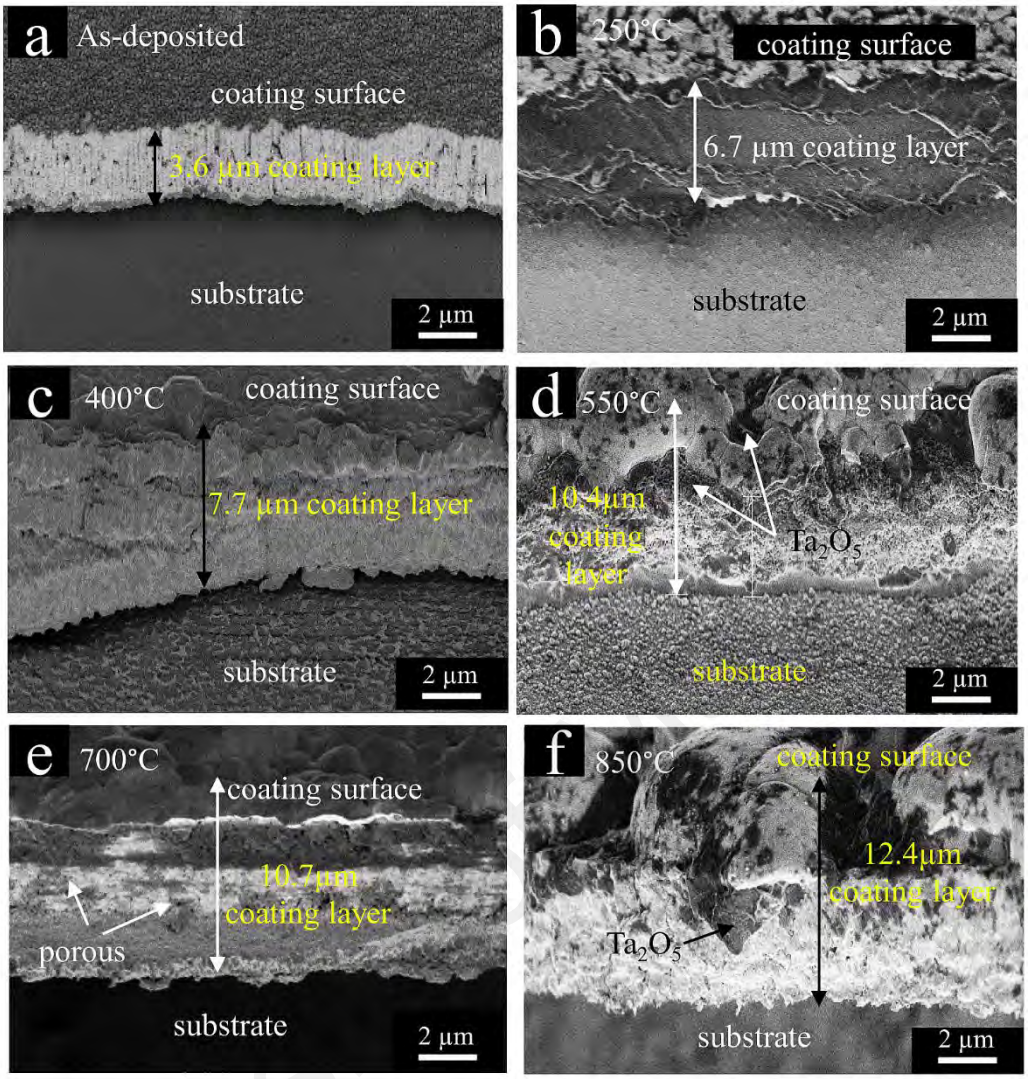


Figure 4.21: Cross section views of Ag/Ag-$Ta_2O_5$ thin film sample "$S_7$".

(a) as-deposited, and annealed at (b) 250, (c) 400, (d) 550, (d) 700 and (e) 850 °C

As the temperature increased further to 700 °C, where TaO is known to crystallize (Çetinörgü-Goldenberg et al., 2012), the size enlargement of $Ta_2O_5$ was more significant. This suggests the accelerated $Ta_2O_5$ migration rate associated with the enlarged, segregated Ag particles. The highlighted section in Figure 4.20(g) is magnified and displayed in Figure 4.20(h). It can be seen that the number of AgNPs islands at the surface diminished due to the slowing diffusion rate. As the AgNPs diffusion towards the surface progressed, the AgNPs content in the bulk gradually

declined. According to Velasco et al. (2016), the meagre AgNPs content in the bulk limits the diffusion process owning to insufficient momentum. The impact of the active migration of both AgNPs and $Ta_2O_5$ is a porous surface (Figure 4.21(e)). Beyond 800 °, the higher Ostwald ripening rate influenced the segregated Ag size and reduced the number of particles per area (Figure 4.20(i)). The increasingly segregated Ag completely covered the surface and left behind the $Ta_2O_5$ in the hole (Figures 4.20(i) and Figure 4.21(f)).

### 4.3.3 Surface wettability of "$S_6$" to "$S_{10}$" and annealed "$S_7$"

It is remarked that the contact angles obtained have a positive correlation with the surface morphology, as characterized by FESEM. Figure 4.22 exhibits the increasing contact angle trend with rising deposition power (51.8±1.0, 76.47±1.5, 97.2±3.5 °) and substrate temperature (68.76±0.7, 71.76±0.7, 76.47±1.5 °). This result demonstrates that the distribution of comparably larger particles (Figures 4.18(a, c & e)) on the film surface is more hydrophobic. A similar trend was noted for the effect of substrate temperature, which increased the hydrophobicity and was responsible for a more compact film (Figure 4.19(a, c & d)). The effect of annealing temperature on the contact angle is represented graphically in Figure 4.23. The readings for as-deposited "$S_7$", and 250, 400, 550, 700 and 850 °C annealed "$S_7$" were 76.47±1.5, 77.3±0.8, 78.7±2.1, 81.9±0.6, 82.0±0.6 and 83.8±0.3 °, respectively. It is supposed that the hydrophobicity slightly increased with Ag agglomeration size as an effect of the increasing annealing temperature (Figure 4.20).

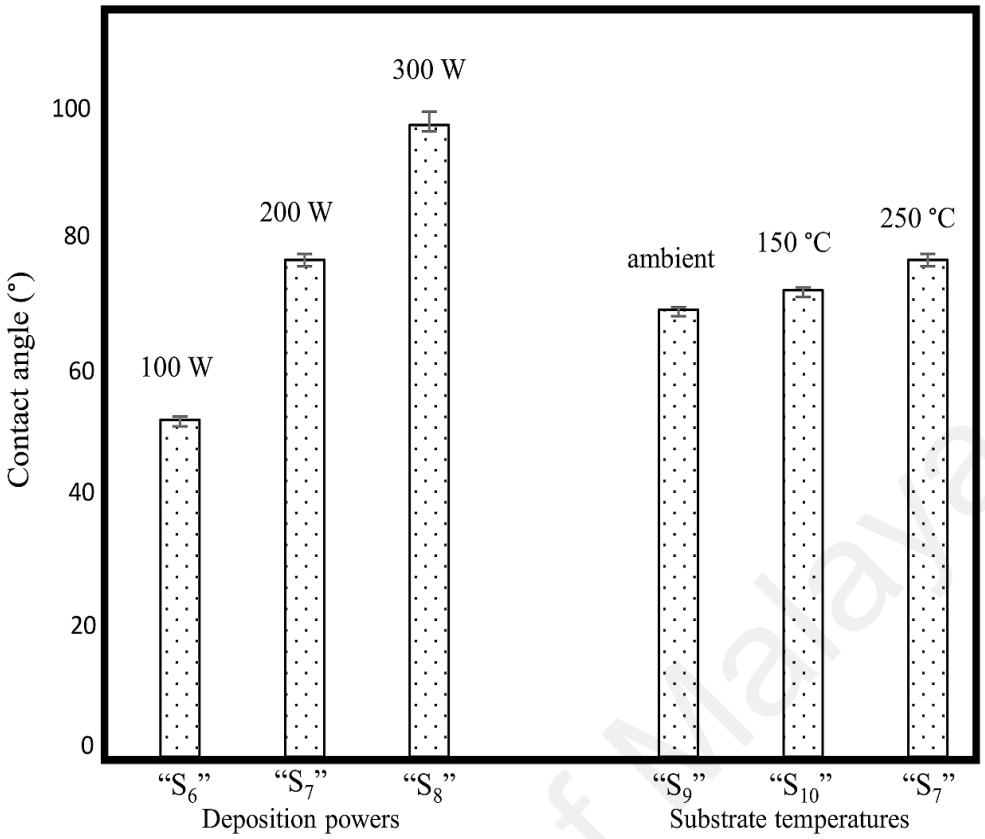


Figure 4.22: Contact angles of the films deposited at variation of power (100-300 W) and substrate temperature (ambient - 250 °C)

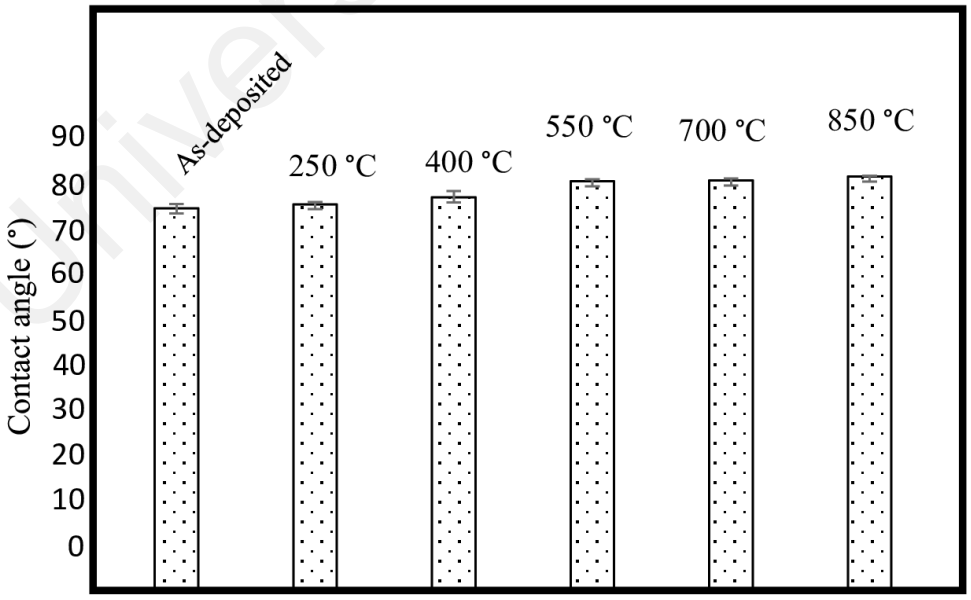


Figure 4.23: Contact angle of the as-deposited "$S_7$" and annealed at 250 to 850 °C

### 4.3.4 Adhesion strength of "$S_6$" to "$S_{10}$" and annealed "$S_7$"

The average adhesion strengths of Ag/Ag/Ag-$Ta_2O_5$ film as-deposited samples "$S_6$" to "$S_{10}$" are summarized in Table 4.9. "$S_7$" was selected for its highest adhesion strength (1302 ±26 mN) during annealing at 250–850 °C. The average adhesion strengths of Ag/Ag-$Ta_2O_5$ film samples as-deposited "$S_7$" and annealed "$S_7$" are tabulated in Table 4.10 and Table 4.11. The subsequent annealing process signified that 400 °C is an optimum temperature condition (3310 ±84 mN), as indicated in Table 4.11.

Table 4.10: Adhesion strength of as-deposited "$S_6$" to "$S_{10}$" of Ag/Ag-$Ta_2O_5$ thin films

| Samples | Adhesion Strength (mN) |
|---|---|
| "$S_6$" | 786 ±17 |
| "$S_7$" | 1302 ±26 |
| "$S_8$" | 1020 ±84 |
| "$S_9$" | 589 ±108 |
| "$S_{10}$" | 484 ±32 |

Table 4.11: Adhesion strength of as-deposited "$S_7$" and 250, 400, 550, 700 and 850 °C annealed "$S_7$"of Ag/Ag-$Ta_2O_5$ thin films

| Samples | Adhesion Strength (mN) |
|---|---|
| As-deposited | 1302 ±26 |
| 250 °C annealed | 1926 ±56 |
| 400 °C annealed | 3310 ±84 |
| 550 °C annealed | 2296 ±113 |
| 700 °C annealed | 2301 ±143 |
| 850 °C annealed | 953 ±10 |

Figures 4.24(a,b) represent the corresponding graphs of depth (I), load (II) and friction (III) versus distance for as-deposited "$S_7$" and 400 °C annealed "$S_7$". In Figure 4.24(a) the failure point on thin film is marked at 1330 mN, whereby total failure occurred at a distance of 799 µm. In Figure 4.24(b), the failure point occurred at 789 µm, representing 3373 mN adhesion strength. According to the results, the adhesion strength of the 400 °C annealed "$S_7$" improved by about 154 %.

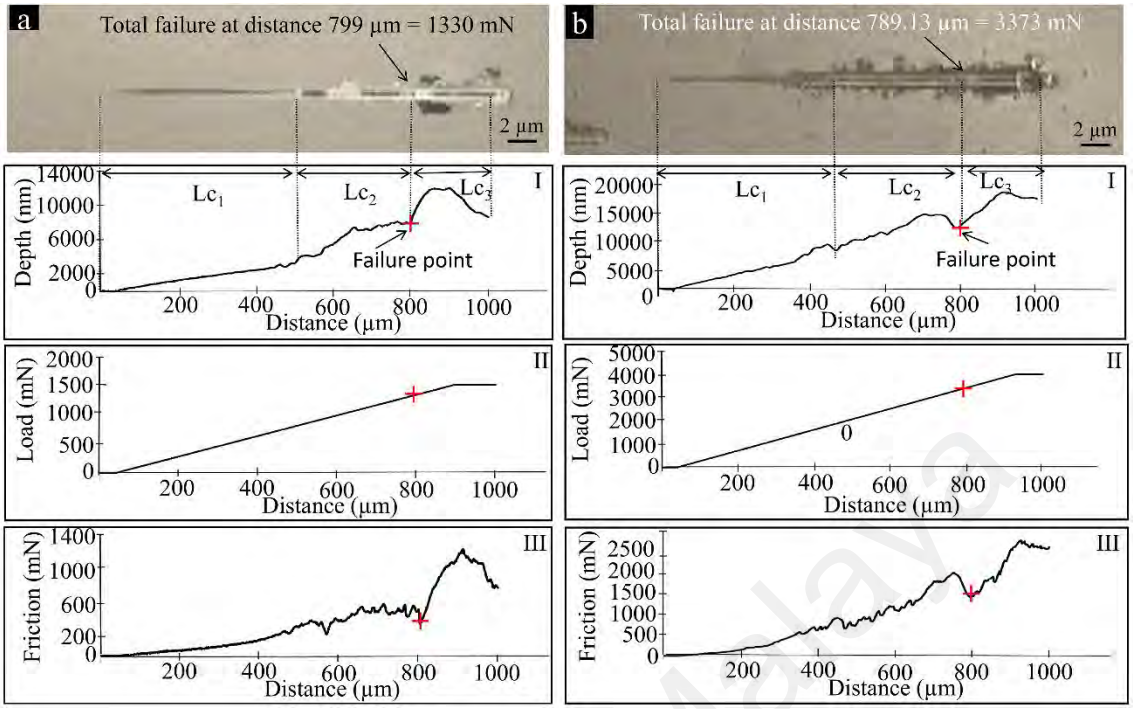


Figure 4.24: Optical surface scratch images, depth, load and friction with respect to scratch distance as well as failure points of the (a) as deposited "$S_7$" (1330mN) and (b) 400 °C annealed "$S_7$"(3373 mN)

### 4.3.5 Phase analysis of "$S_6$" to "$S_{10}$" and annealed "$S_7$"

Figure 4.25 depicts the XRD patterns of Ag/Ag-$Ta_2O_5$ thin film samples as-deposited "$S_6$" to "$S_{10}$". The predominant peak is likely associated with the Ag phase due to the amorphous nature of as-deposited $Ta_2O_5$. The orientations of the Ag cubic crystal planes are defined at (1 1 1), (0 0 2), (0 2 2), (1 1 3) and (2 2 2), consistent with standard data file ICSD No. 98-002- 4387. The peaks corresponding to specific phases produced similar outcomes for all samples, confirming that this material can retain its original structure in different PVD magnetron sputtering power and substrate temperature conditions.

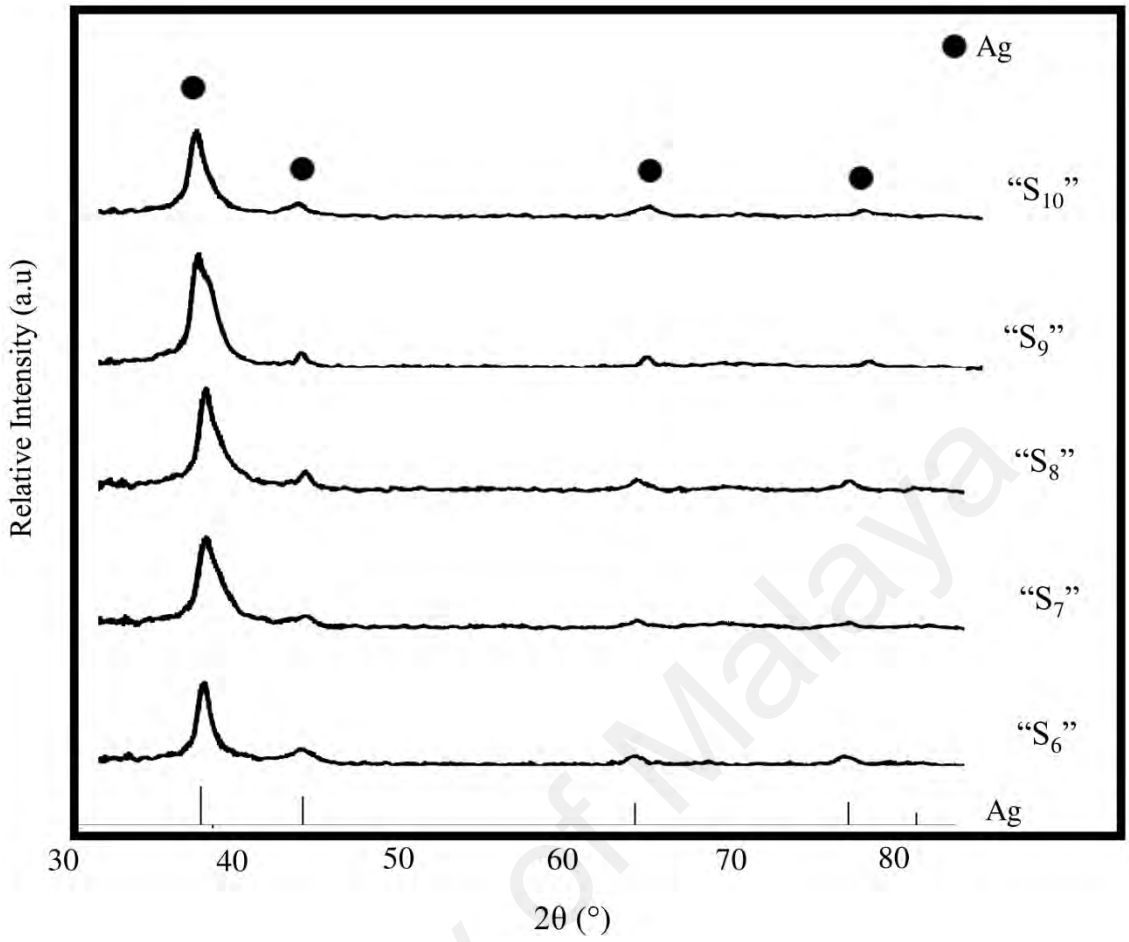


Figure 4.25: XRD patterns of Ag/Ag-$Ta_2O_5$ thin film of as-deposited "$S_6$" to "$S_{10}$"

However, some abrupt changes were observed after annealing the coating sample (Figure 4.26). After annealing the as-deposited "$S_7$", the Ag segregated from the bulk to the surface. Furthermore, annealing from 250 °C upwards promoted Ag crystallization. Thus, a single Ag phase with an intensified Ag peak was detected by XRD. When "$S_7$" was annealed between 550 and 700 ºC, $AgTaO_3$ (ICSD No. 98-004-0830) was present. The high kinetic energy persuaded the reactivity of Ag near, or on the $Ta_2O_5$ surface (Figures 4.20(e-h)), producing $AgTaO_3$ (ICSD No. 98-004-0830). When the "$S_7$" film was further annealed at 850 ºC, the XRD pattern shows diminished $AgTaO_3$, which correlates with the FESEM morphology shown in Figure 4.20(i).

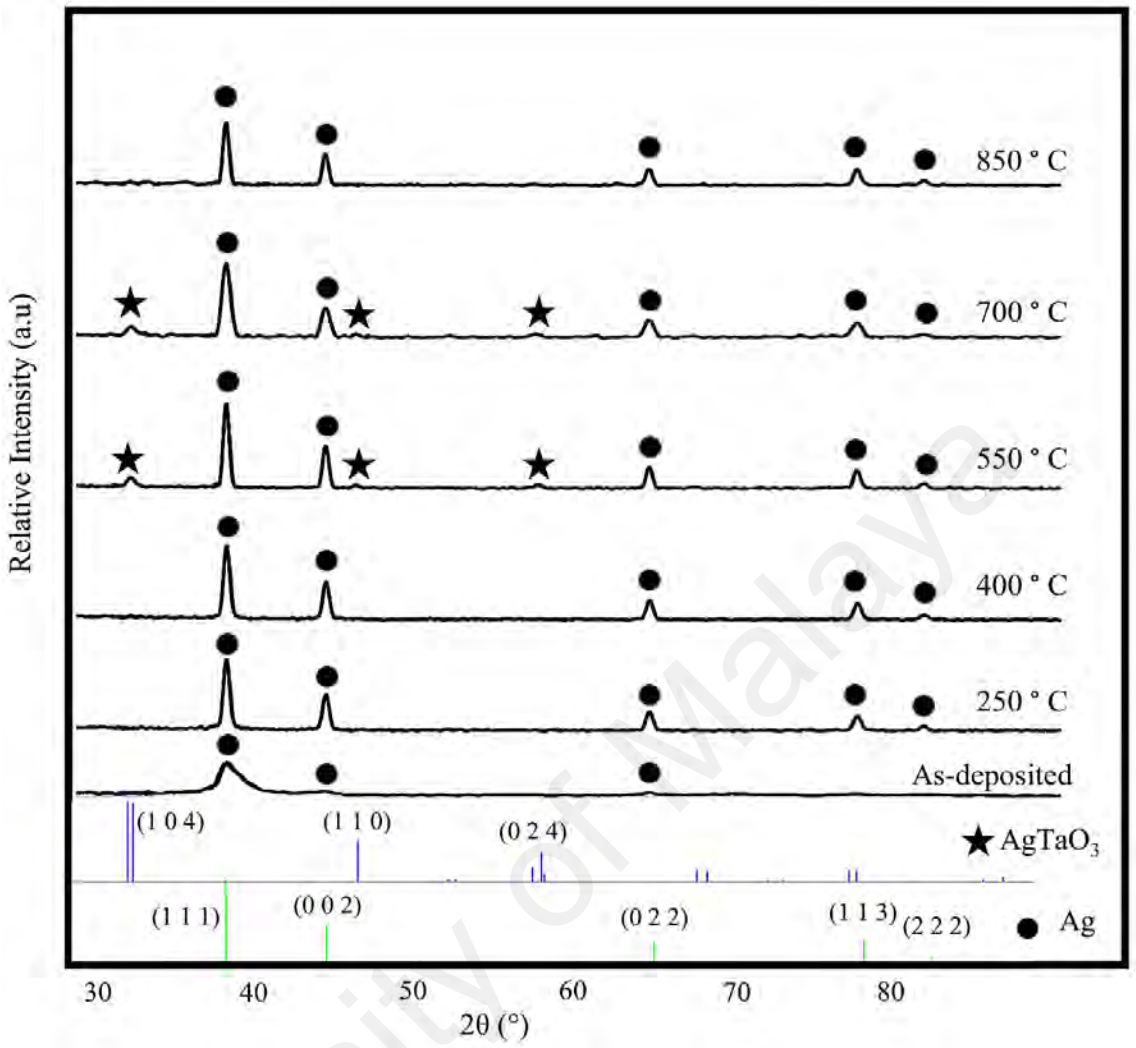


Figure 4.26: XRD patterns of Ag/Ag-$Ta_2O_5$ thin film of as-deposited "$S_7$" and after annealing at 250, 400, 550, 700 and 850 °C

### 4.3.6 Nano Indentation of "$S_7$" and annealed "$S_7$"

Figure 4.27 shows an in-situ SPM image with the areas of indentation, before indentation and after indentation. Figures 4.27(b & c) illustrate bar charts of the hardness and Young's modulus of as-deposited "$S_7$" and 250, 400, 500, 700 and 850 °C annealed "$S_7$". It should be noted that the Young's modulus calculation results have a similar trend to that observed for the hardness results. The main remark in Figure 4.27 is the poor hardness typical of nanocomposite film (Adochite et al., 2012). Apart from the hilly surface (before indentation in the image), the inconsistent hardness in Figure

4.27(b) may have been caused by the flawed contact area as explained in literature (Sarraf et al., 2017). Such contact area forms when the soft surface specimen being indented prefers to accumulate near the indenter tip, enlarging the contact area. This leads to inaccurate hardness values due to the material's elastic recovery. Thus, the indenter tip was prevented from penetrating the Ag/Ag-$Ta_2O_5$ film surface (Figure 4.27(a)-after indentation image).

The hardness rose dramatically from 0.65±0.42 GPa (as-deposited "$S_7$" specimen) to 1.12±0.43 GPa (400 °C annealed "$S_7$"), suggesting the crystallization of Ag and enhancement of Ostwald ripening. As suggested by the FESEM morphological analysis in Figure 4.20 and XRD patterns in Figure 4.26, crystallization normally contributes to the enhanced mechanical properties correlated with the improved adhesion strength after annealing. However, the reading in the bar graph dropped to 0.85±0.35 GPa at 550 °C annealing owning to the presence of a large amount of AgNPs over the surface (Figures 4.20(e-f)). Adochite et al. (2012) reported that the amorphous state of the film, the presence of small Ag particles on the film, induces a softer film. The reading on the bar graph then gradually increased to 0.96±0.24 GPa at 700 °C annealing. The crystallization of $Ta_2O_5$ at this stage was responsible for the sharply increasing hardness value following the prior drop in value. In due course, the reading rose rapidly up to 1.52±1.27 GPa at 850 °C.

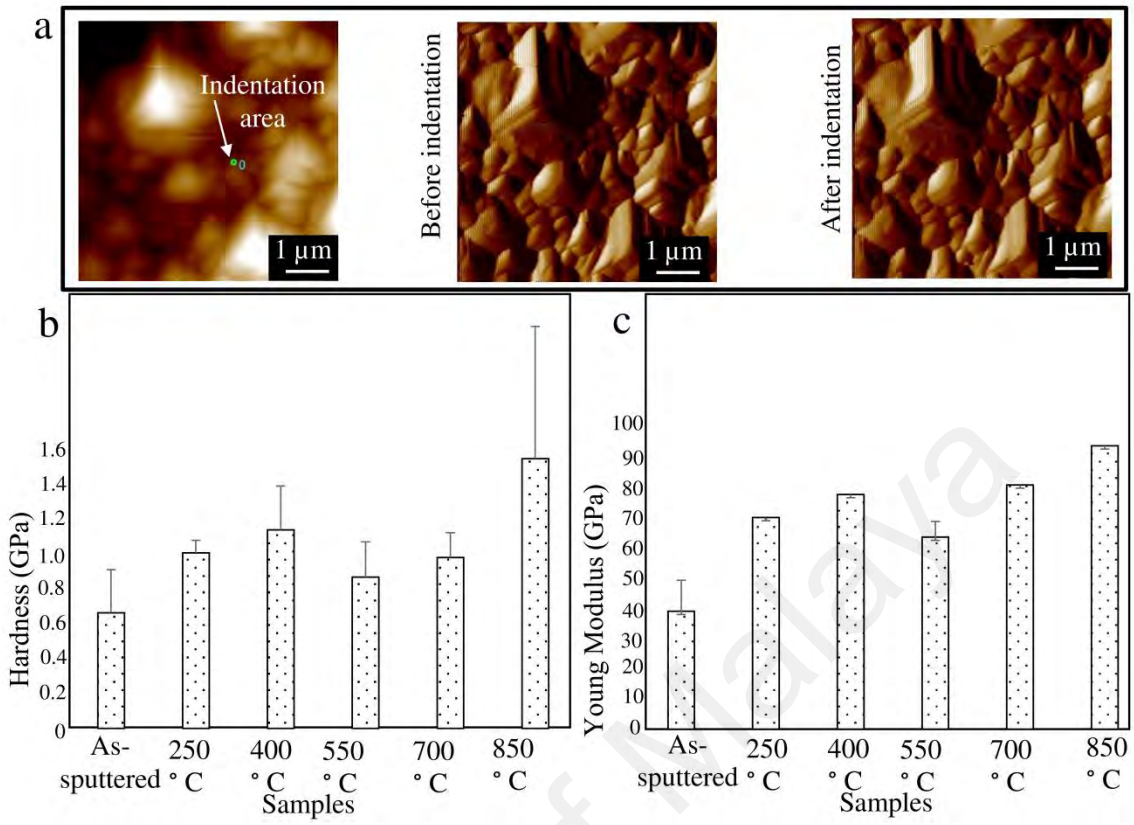


Figure 4.27: (a) In-situ SPM images of the area indentation, before indentation and after indentation on the 400 °C annealed "$S_7$", trends of (b) hardness and (b) Young's modulus of Ag/Ag-$Ta_2O_5$ film as-deposited "$S_7$" sample and 250, 400, 500, 700 and 850 °C annealed "$S_7$

### 4.3.7 Surface chemistry analysis of "$S_7$" and 400 °C annealed "$S_7$"

Figure 4.28(a & b) illustrate the XPS spectra of the as-deposited "$S_7$" and "$S_7$" annealed at 400 °C. The spectrum of the as-deposited "$S_7$" exhibits the major peaks characteristic of Ag Auger emission, O KLL (Auger electron), Ag 3p, Ag 3d, Ag 4d, O 1s, C 1s, Ta 4s, Ta 4p, Ta4d and Ta 4f. The 400 °C annealed "$S_7$" film obtained peaks of Ag Auger emission, Ag 3p, Ag 3d, Ag 4p, Ag 4d, O 1s and C 1 s. Both spectra confirm the results of the FESEM surface morphological analysis in Figure 4.20 (a & d) and verifies the Ag peaks from XRD phase analysis in Figure 4.26.

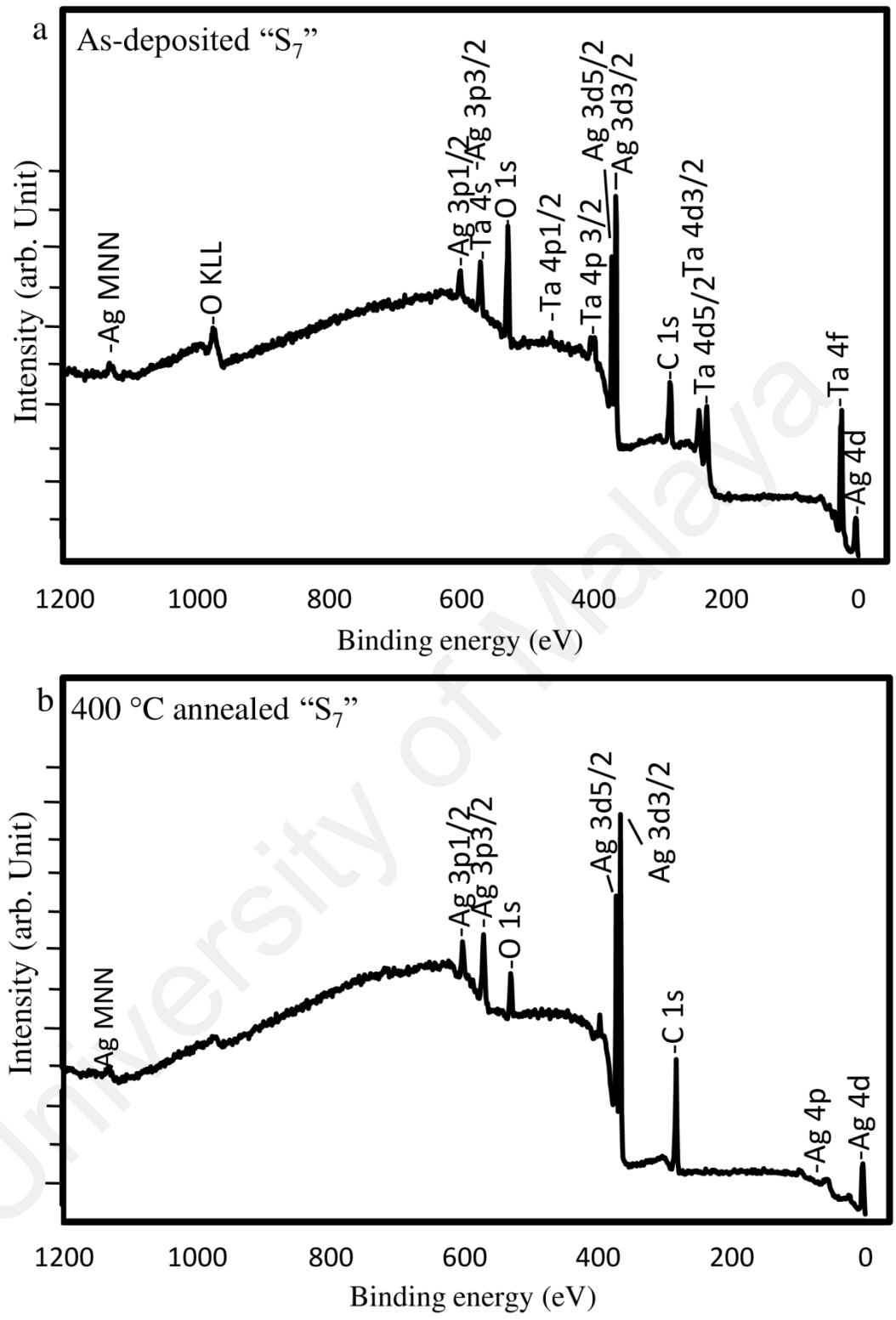


Figure 4.28: XPS spectra of the as-deposited sample "$S_7$" and 400 °C annealed "$S_7$" Ag/Ag-$Ta_2O_5$ thin films

The spectra were then analyzes at a take-off angle of 45 ° and are shown in the Figure 4.29 and Figure 4.30 with the linear background subtracted. These spectra were deconvoluted as shown by the dashed curve in Figure 4.29 and Figure 4.30 to investigate the bonding states of this film.

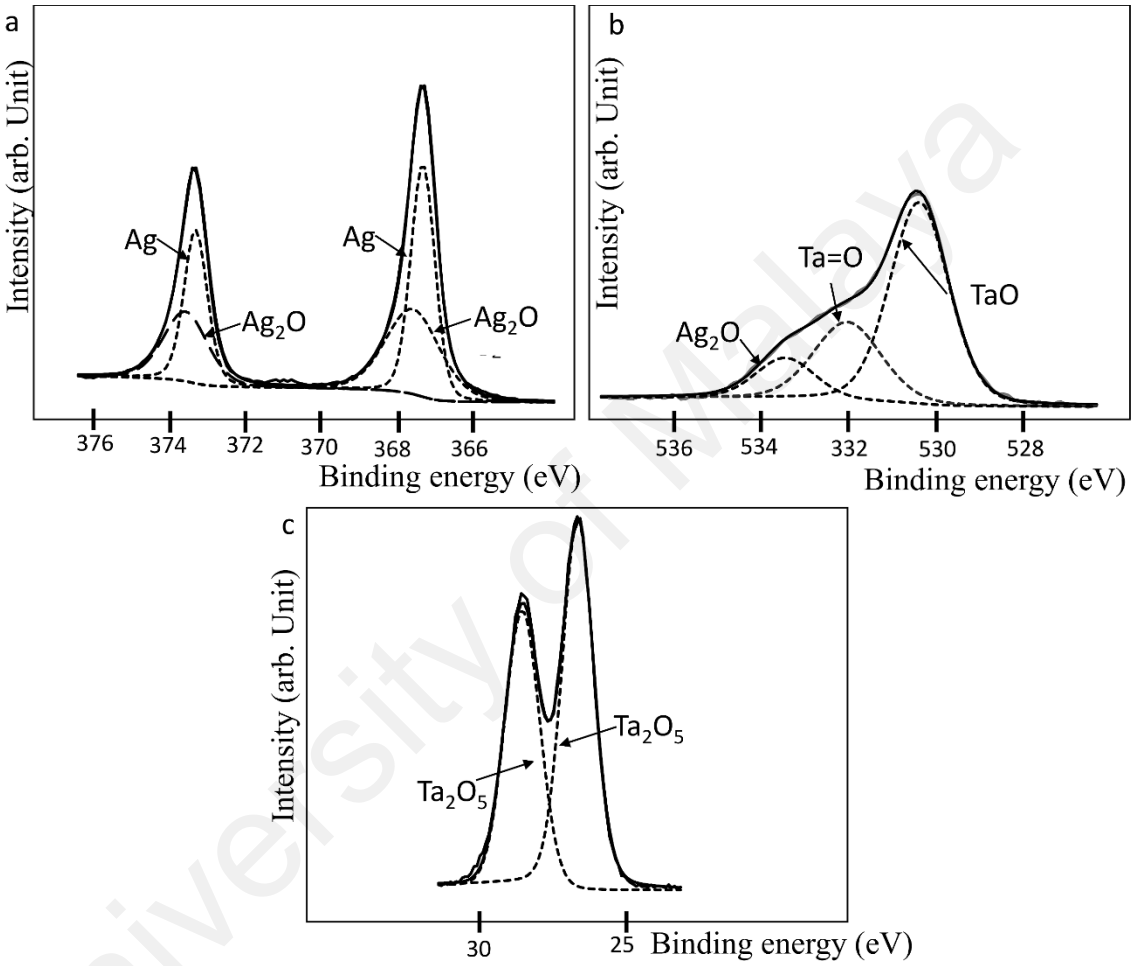


Figure 4.29: Deconvoluted photoelectron spectra (solid curves) of Ag3d (a), O1s (b), and Ta4f (c). Each spectrum was decomposed into its bonding states (shown by dashed curves) of as-deposited "$S_7$" Ag/Ag-$Ta_2O_5$ thin films

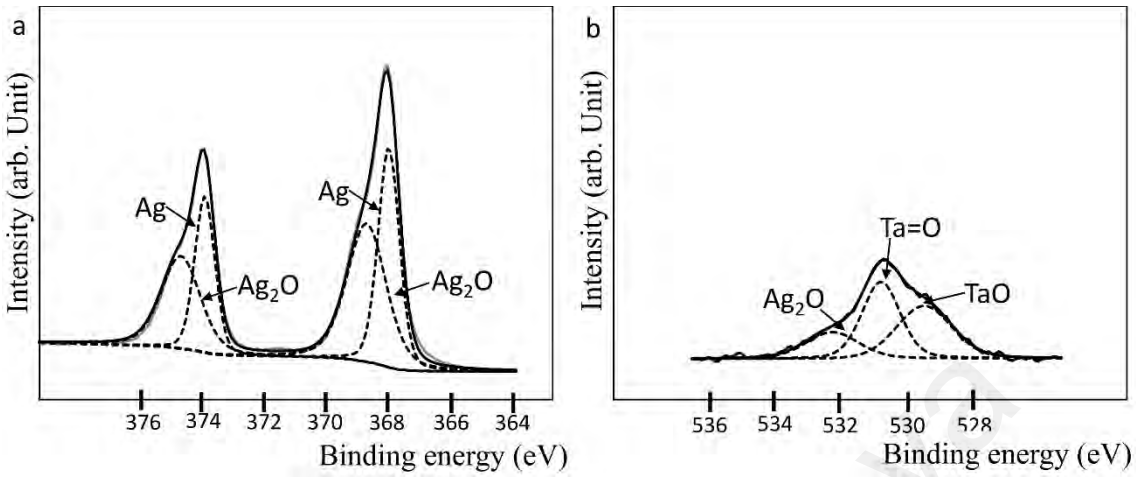


Figure 4.30: Deconvoluted photoelectron spectra (solid curves) of Ag3d (a) and O1s (b). Each spectrum was decomposed into its bonding states (shown by dashed curves) of 400 °C annealed "$S_7$" Ag/Ag-$Ta_2O_5$ thin films

For as the deposited case in Figure 4.29, the Ag3d spectra was deconvoluted into a major $Ag3d_{3/2}$ (peak centered at 367.33eV) and $Ag3d_{5/2}$ (373.0 eV), which are attributed to the Ag metal. Meanwhile, the deconvoluted peak centered at 367.59 and 373.57 eV correspond to $Ag_2O$ in Figure 4.29(a). The O1s spectrum comprises 3 peaks were centered at 530.40, 532.03 and 533.43 eV, which are attributable to TaO, Ta=O and $Ag_2O$, respectively (Figure 4.29(b)). The Ta4f spectrum in Figure 4.29(c) indicates $Ta4f_{5/2}$ (26.17 ev) and $Ta4f_{7/2}$ (28.05 eV), attributable to $Ta_2O_5$. Similar behavior has been observed in the annealed film case (Figure 4.30(a & b)). The Ag and $Ag_2O$ were centered at 368.04, 374.06, 368.77 and 374.84 eV, respectively originating from the pairs of $Ag3d_{3/2}$ and $Ag3d_{5/2}$ peaks. The TaO, Ta=O and $Ag_2O$ from O1s spectra peaks in Figure 4.30(b) were centered at 530.68, 532.15 and 533.46 eV, respectively. Due to annealing, the Ta spectrum did not appear in the Figure 4.28(b) confirming the segregated Ag particle covered the surface and left the Ag-$Ta_2O_5$ composite behind in the bulk coating.

### 4.3.8 *In-vitro* antibacterial activity and biocompatibility of uncoated SS 316L, and 400 and 700 °C annealed "$S_7$"

The antibacterial activity was analyzed for uncoated SS 316L, 400 °C annealed "$S_7$" and 700 °C annealed "$S_7$" of Ag/Ag-$Ta_2O_5$ thin films. The 400 °C annealed "$S_7$" diaplayed a halo inhibition zone around the material for both *S. aureus* and *E. coli,* whereas the uncoated SS 316L (control) did not show any halo inhibition zone (Figure 4.31).

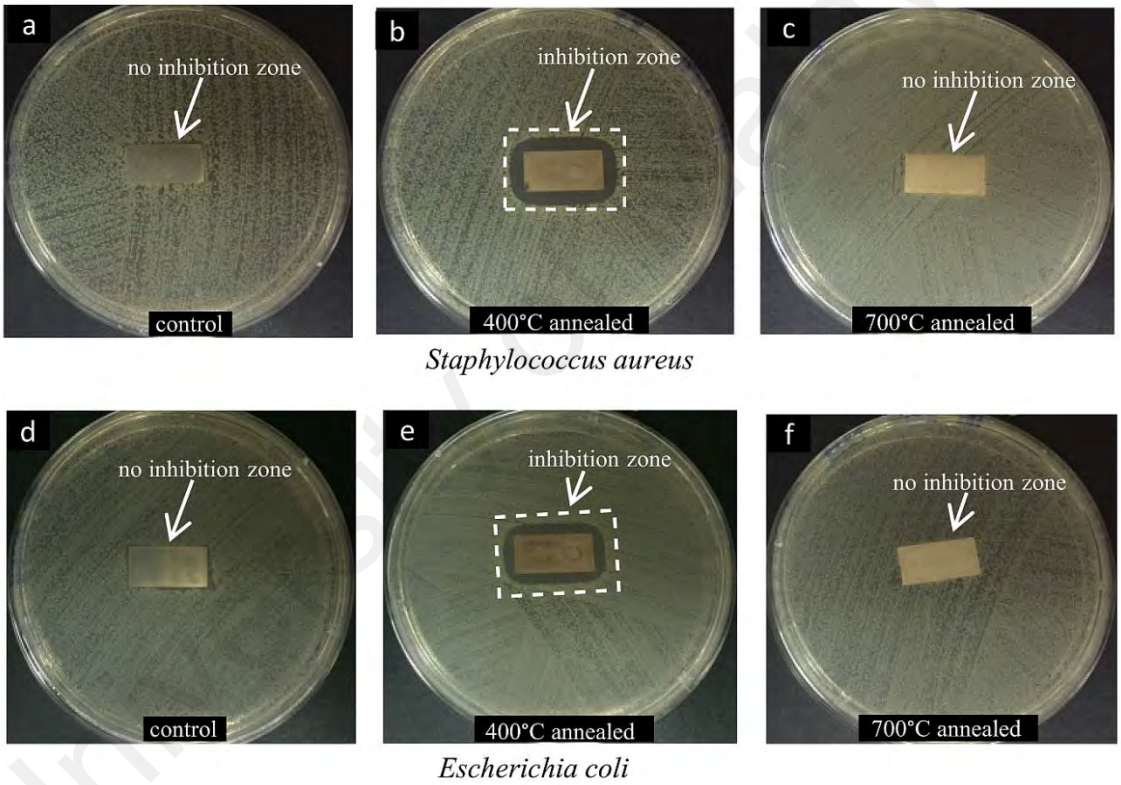


Figure 4.31: Halo inhibition test showing a (a,d) survived colonies of *S. aureus* and *E.coli* on the control sample, (b,e) zone of growth inhibition of of *S. aureus* and *E.coli* by 400 °C annealed "$S_7$", (c,f) no growth inhibition of of *S. aureus* and *E.coli* by 700 °C annealed "$S_7$". The images are representative of three replicates

Measurement of the inhibition zone diameters across the short axis (A) and long axis (B) demonstrated similar zone of inhibition for the coated material against both *E.*

*coli* and *S. aureus* (Table 4.12). The 400 °C annealed "$S_7$" results are (A: 16.33 ±0.58; B: 25.67 ±0.58) for *S. aureus* and (A: 16.33 ±1.15; B: 26.00 ±0.00) for *E. coli*. This indicates the good antibacterial performance of Ag/Ag-$Ta_2O_5$ thin films annealed at 400 °C. The Ag/Ag-$Ta_2O_5$ thin films developed in this work have a similar mean inhibition zone diameter with Ag-carbon nanotube coating with 27.9 ± 6.72 mm and 21.9 ± 4.33 mm mean inhibition zone diameters for *S. aureus* and *E. coli*, respectively (Rangari et al., 2010). Earlier finding for AgAu/PTFE coating that is applicable for medical polymer devices show 3 and 1 mm inhibition zone diameters against *S. aureus* and *E. coli*, respectively (Zaporojtchenko et al., 2006)

However, 700 °C annealed "$S_7$" produced results similar to the control sample. Growth inhibition were not seen for either *S. aureus* or *E. coli* pathogens. The significant difference between the 400 and 700 °C annealed "$S_7$" samples suggests that the new $AgTaO_3$ phase which precipitated in the 700 °C annealed "$S_7$" reduced the antibacterial efficiency.

Table 4.12**:** Average inhibition zone diameter of the control sample and 400 and 700 °C annealed "$S_7$" against *S.aureus* and *E.coli.*

| Test bacteria | Average inhibition zone diameter (mm) | | | | | |
|---|---|---|---|---|---|---|
| | Control sample | | 400 °C annealed "$S_7$" | | 700 °C annealed "$S_7$" | |
| | A | B | A | B | A | B |
| Staphylococcus aureus (NCTC 6571) | No inhibition | No inhibition | 16.33 ±1.15 | 26.00 ±0.00 | No inhibition | No inhibition |
| Escherichia coli (ATCC 15597) | No inhibition | No inhibition | 16.33 ±0.58 | 25.67 ±0.58 | No inhibition | No inhibition |

### 4.3.9 Cell attachment

The interaction of hBMSCs with uncoated SS 316L (control sample) and two Ag/Ag-$Ta_2O_5$ thin films (400 °C and 700 °C annealed "$S_7$") was eamined. To assess the cells' interaction with the samples, hBMSCs were seeded onto the samples and SEM micrographs and confocal images were captured. The SEM micrographs indicate that cell attachment happened in all sample groups, suggesting their biocompatibility property (Figures 4.32**(**b, e & g)). However, it was observed that hBMSCs seeded on the 400 °C annealed "$S_7$" colonised the sample surface more extensively than either the 700 °C annealed "$S_7$"or control sample. Moreover, the presence of an extracellular matrix (ECM) especially at the periphery of the hBMSCs-seeded 400 °C annealed "$S_7$" suggests that this material provides optimal conditions for cell adhesion and adaptation (Figure 4.32**(**f)). Although this notion has never been reported in studies of tests on similar materials as presented in this study, the importance of ECM secreted on

materials that support cell adhesion, signalling and homeostasis has been well-elucidated (Bruce et al., 2001; Secker et al., 2012). A difference in cell morphology was also observed between 400 °C annealed "$S_7$" and 700 °C annealed "$S_7$" or control sample. A difference in cell morphology was also observed between the 400°C annealed "$S_7$" and 700 °C annealed "$S_7$" or the control sample. The hBMSCs in contact with the 400 °C annealed "$S_7$" seem to have long filopodia and a spreading morphology compared with other sample groups. This may be due to the direct contact of the cells and tantalum oxide, which can enhance cell adherence as reported in other studies (Ceviker et al., 1998).

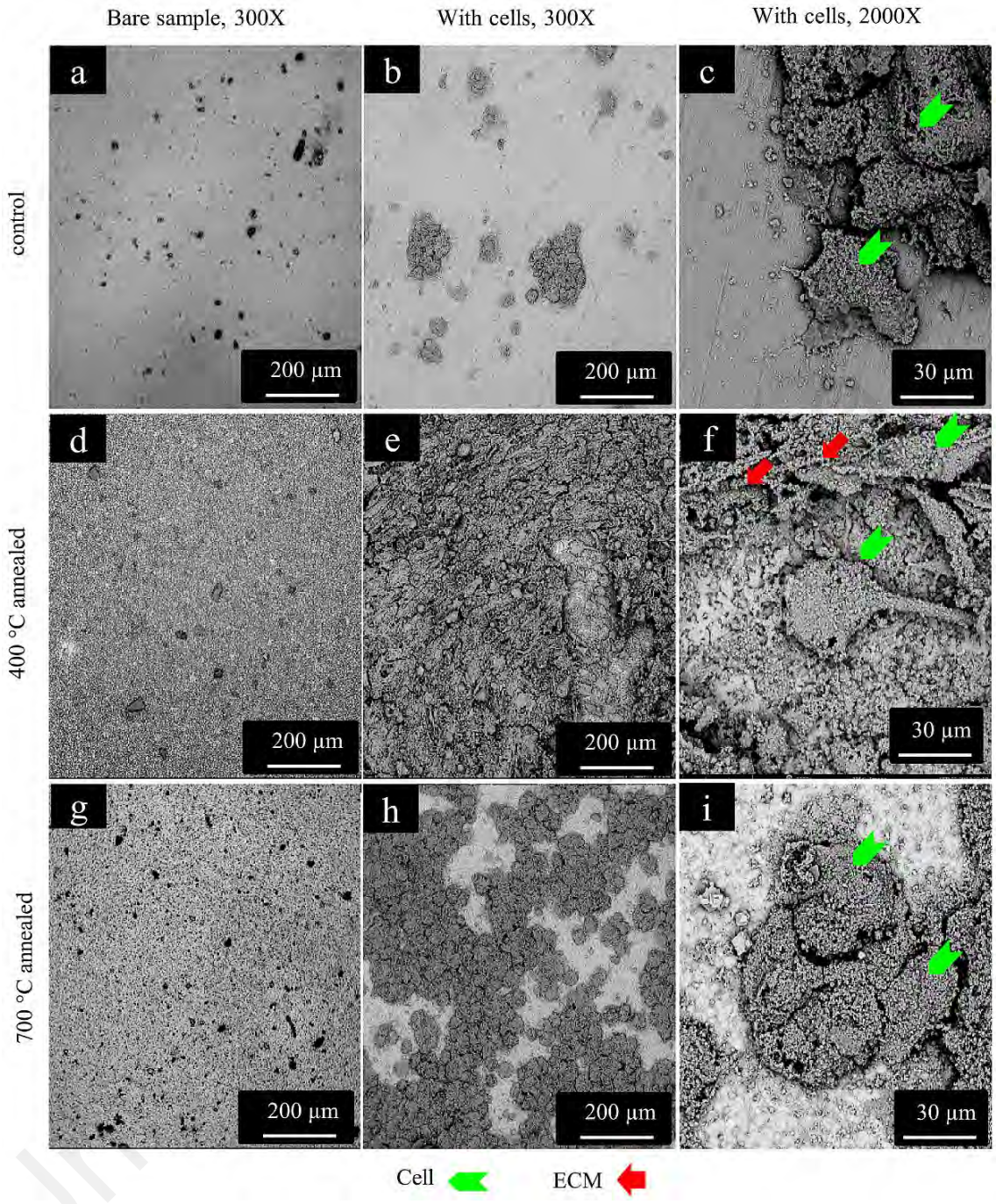


Figure 4.32: SEM micrographs of hBMSCs attached on control sample (a-c), 400 °C annaled "$S_7$" (d-f) and 700 °C annealed "$S_7$" (g-i) on day 14. The images are representative of three replicates

The cell-material interaction is a complex bi-directional and dynamic process that mimics to a certain extent the natural interactions of cells with the extracellular matrix. Cells tend to adhere and rearrange adsorbed extracellular matrix (ECM) proteins on the material surface in a fibril-like pattern (Tong et al., 2011). In the present study, the expression of F-actin protein by the control sample, 400 °C annealed "$S_7$" and 700 °C annealed "$S_7$" seeded hBMSCs were observed on the day 14 of the post-seeding. The confocal images confirmed that the seeded cells had expressed F-actin protein on all sample groups (Figure 4.33 (b, e & g)). However, hBMSCs seeded on the 400 °C annealed "$S_7$" seemed to have a widely spread fibril-like pattern. This phenomenon occurs when the surface chemistry of the material is favorable for optimal cell attachment, as delineated in earlier studies (Llopis-Hernández et al., 2011). Moreover, the nucleus staining further supports the SEM analysis finding that 400 °C annealed "$S_7$" seeded with hBMSCs colonized the material surface much more extensively than the other sample groups (Figure 4.33(d**)).**

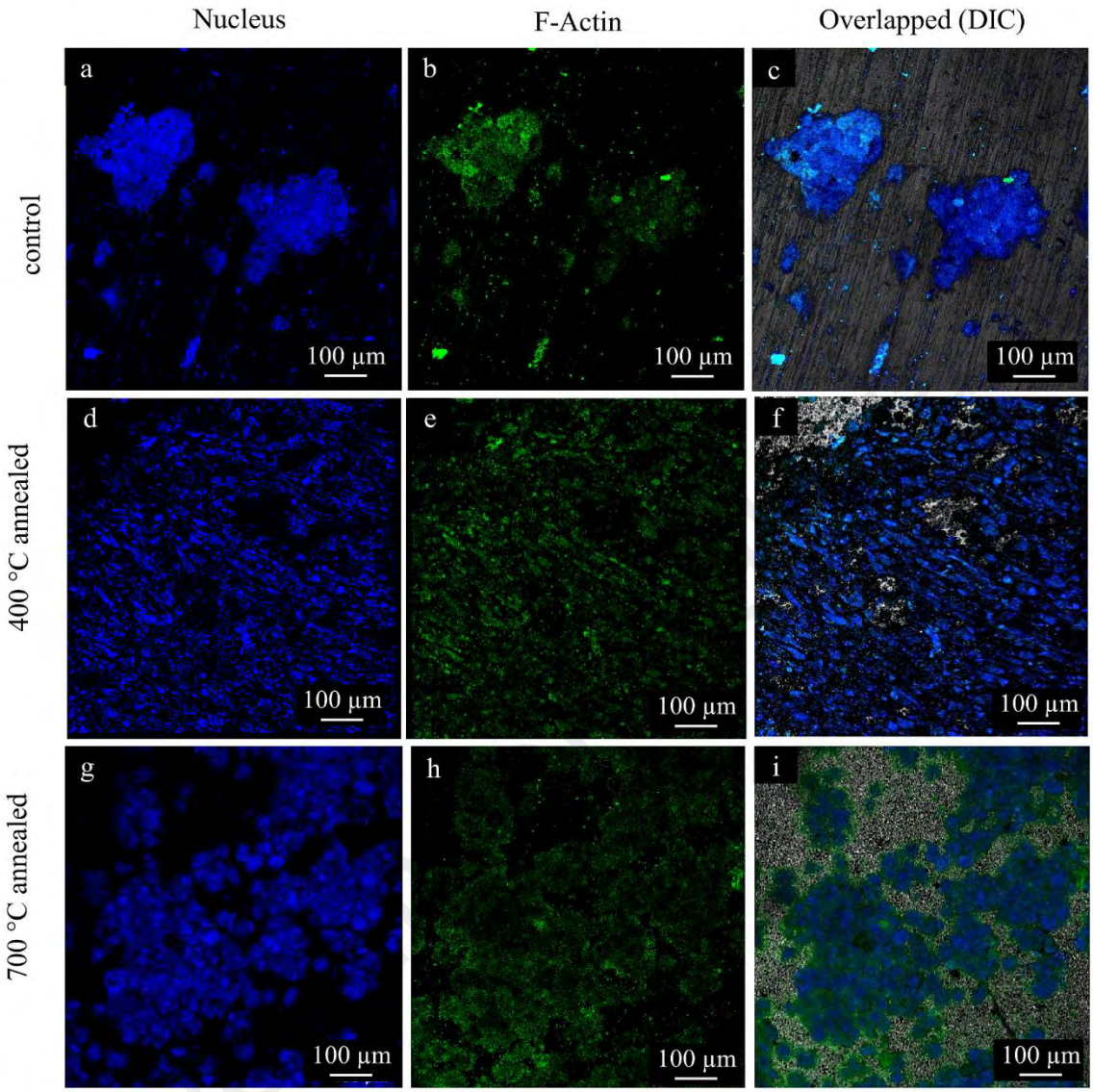


Figure 4.33: hBMSCs F-actin confocal profile on control sample (a-c), 400 °C annealed "$S_7$" (d-f) and 700 °C annealed "$S_7$" (g-i) on day 14. The (differential interference contrast) DIC images demonstrate the overlapped images of F-actin staining of cells (Green) counterstained with Hoechst blue nuclei staining (Blue) and the surface of the control sample, 400 °C annealed "$S_7$" and 700 °C annealed "$S_7$" (Grey). The images are representative of three replicates

### 4.3.10 Cell viability and proliferation

Tantalum has been widely used clinically since 1940s owing to its excellent corrosion resistance and biocompatibility (S. Kumar et al., 2017). However, only few studies have examined the optimal conditions corresponding to the antimicrobial activity and biocompatibility of Ag/Ag-$Ta_2O_5$ prepared at different annealing temperatures (Hergenrother et al., 1995; Mikami et al., 2007). In the present study, the viability and proliferative potential of the 400-700 °C annealed "$S_7$" and SS316L control sample on hBMSCs were studied using AB cell viability/proliferation assay. The reduction of AB percentage was measured based on optical density, and it correlated positively with the density of viable cells. It was found that the hBMSCs proliferation seeded on 400-700 °C annealed "$S_7$" and SS 316L control sample on day 3 dropped significantly by about 12, 5 and 4 % ($p$=0.01), respectively from day 1 (Figure 4.34). This drop in cell proliferation could be due to the cells having adapted to the new material surface micro-environment, which is different than that on the plastic surface of culture flask. However, an increase in cell proliferation was observed on day 7 and 14 compared with day 1. The proliferation rate of cells was most significant on day 14 on 400 °C annealed "$S_7$" and 700 °C annealed "$S_7$" (42 %, $p$=0.01), while the rate was 33 % for the control sample ($p$=0.01) compared with day 1 (Figure 4.34). When comparing the hBMSCs viability between samples at different time point, the 400 °C annealed "$S_7$" and 700 °C annealed "$S_7$" seeded hBMSCs showed more significant cell viability on day 7 and 14 than the control sample ($p$=0.01). Moreover, a marginal yet significantly greater increase in cell viability was observed in the 400 °C annealed "$S_7$" seeded with cell on day 14 than in the 700 °C annealed "$S_7$" (Figure 4.34, 1.1-fold, $p$=0.04). This finding allows speculating that the 400 °C annealed "$S_7$" exhibits superior biocompatibility to both 700 °C annealed "$S_7$" or control sample.

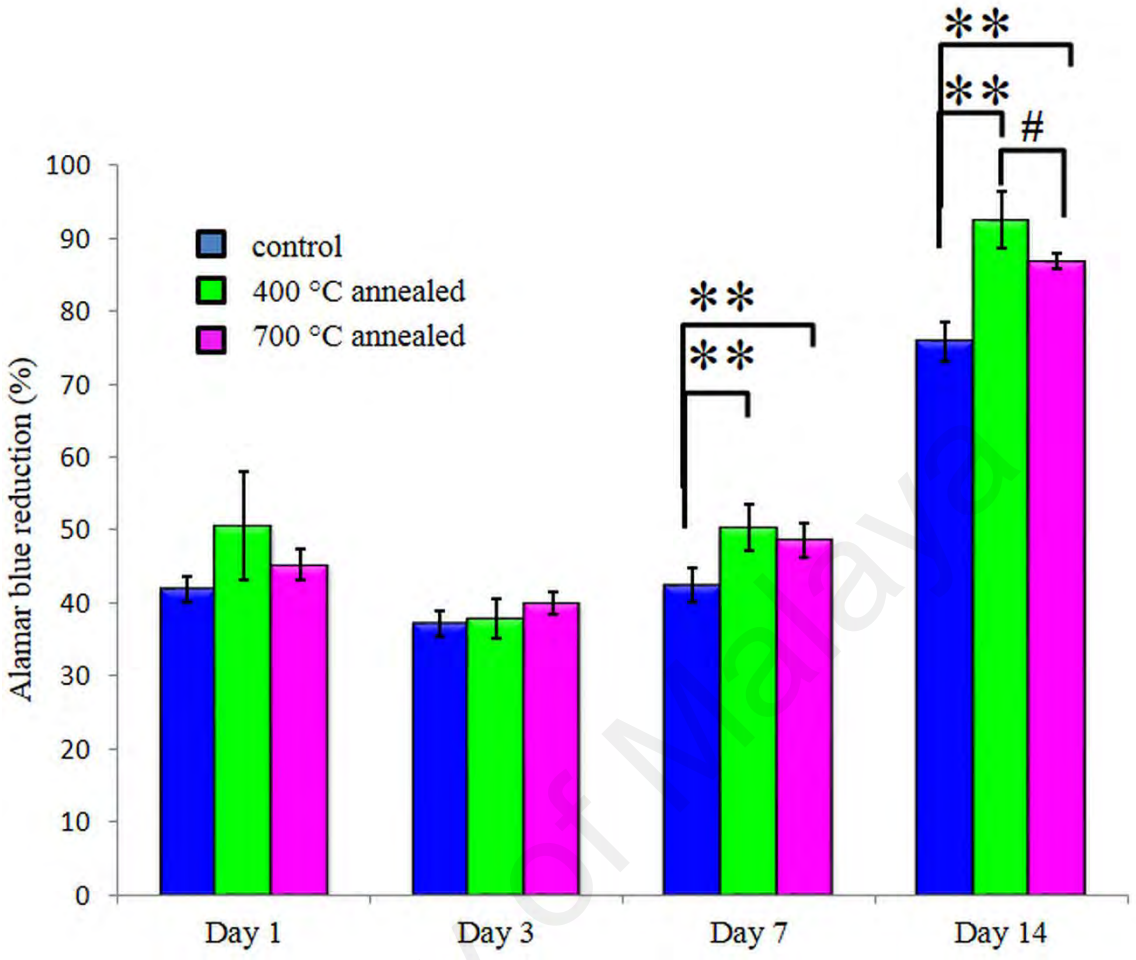


Figure 4.34: hBMSCs viability/proliferation seeded on 400 and 700 °C annealed-"$S_7$" and control sample on day 1, 3, 7 and 14. The alamarBlue™ (AB) reduction was measured using the formula provided in manufacture protocol. The AB reduction is positively correlated with cell density. (Significant level: ** $p < 0.01$, relative to SS316L and $^{\#}$ $p < 0.05$, relative to Ag/Ag-$Ta_2O_5$ 700 °C)

### 4.3.11 Summary

A range of deposited particle sizes were obtained by applying various deposition powers. The results indicate that the substrate temperature influenced the as-deposited film compactness. Moreover, the as-deposited nanocomposite film exhibited low adhesion strength and poor crystallization. Post annealing at a range of temperatures significantly altered the morphology of the as-deposited samples. This change in

morphology also helped the film phase to attain better adhesion strength. Annealing at 400°C induced excessive Ag segregation and improved crystallinity, which resulted in excellent adhesion strength. Nevertheless, beyond 550 °C the tendency of $Ta_2O_5$ to segregate at the surface was obvious. At the surface, the segregated $Ta_2O_5$ may react with Ag in the vicinity and form a new phase, $AgTaO_3$, which may be responsible for diminished adhesion strength, antibacterial performance and biocompatibility. The Ag/Ag-$Ta_2O_5$ thin film sample 400 °C annealed "$S_7$" demonstrated outstanding antibacterial activity, hBMSCs attachment and proliferation activity in contrast to the 700 °C annealed $S_7$ and uncoated SS 316L.

### 4.4 General summary of results finding

The homogenous distribution of Ag-$Ta_2O_5$ and Ag/Ag-$Ta_2O_5$ nanocomposite thin films (confirmed by EDX analysis) signifies the successful deposition on the surface of stainless steel substrate (as-deposited). However, the annealing process altered the surface morphology significantly. The results demonstrate that the Ag particles segregated and crystallized, which was additionally confirmed by the FESEM surface microstructural analysis presented in Figures 4.1, 4.3, 4.14 and 4.20. The $Ta_2O_5$ segregated when the annealing temperature reached 700 °C. The resultant porosity and substantial increase in thickness (Figure 4.20) support the notion of $Ta_2O_5$ migration from the composite bulk to the surface.

The increase in Ag agglomeration size as a function of annealing temperature also demonstrates the improvement in thin film hardness. According to Figure 4.27, the hardness and Young's modulus values increased with annealing (except the 550 °C annealed "$S_7$" thin film).

The Ag segregation suggests the hydrophobicity, the highest adhesion strength, and increase in the peak intensity of the XRD pattern. It can be seen in Figure 4.4, Figure 4.15 and 4.22 the hydrophobicity properties of all as-deposited samples increased upon annealing.

All the as-deposited samples "$S_1$" to "$S_{10}$" showed the relatively low adhesion strength. However, the adhesion strength was significantly increased after the annealing process. The adhesion strength of "$S_1$", "$S_4$" and "$S_7$" were improved after the thermal treatment process at 400 °C by about 302 %, 152 % and 154 % in Method A, B and C, respectively. In all the deposition methods, the as-deposited thin film which was annealed at 400 °C showed no phase changes and the film surface of this sample does not flake off during the scratch test as illustrated in Figure 4.5, Figure 4.16 and Figure 4.24. This ceramic-metal nanocomposite characteristic is favorable due to its ductility of Ag and hardness of $Ta_2O_5$, which could lead to optimum durability and adhesion strength for surgical instruments. The 2927 mN (400 °C annealed "$S_1$" in method A), 2916 mN (400 °C annealed "$S_4$" in method B) and 3310 mN (400 °C annealed "$S_7$" in method C) adhesion strength obtained in this work is much higher than other coatings developed by PVD magnetron sputtering for biomedical applications. In other studies, the adhesion strength for AgSiN, $AgTiO_2$ reached only up to 596 mN at 577.62 µm distance (Mohamad Zaidi et al., 2018; Sarraf et al., 2018; Umi & Mahmoodian, 2017). The highest adhesion strength for the annealed Ta/TaO reported by Rahmati et al. (2015b), was 1907 mN, while for. Rafieerad et al. (2016) it was 2220 mN for Pd/PdO coating.

The antibacterial surfaced surgical instruments are passing through its infancy and there are not many studies available describing the required characteristics for surgical instruments. However, a few studies carried out to improve the characteristics of

medical devices suggest a surface with low roughness is desirable for medicinal applications to prevent infection (Rahmati et al., 2015a; Siegel et al., 2011). These findings further support the idea of minimal surface roughness in the low-intensity area of Ag particles according to the AFM result in Figure 4.7. In Figure 4.7 of Method A, single layer Ag-$Ta_2O_5$ thin film (as-deposited "$S_1$") when annealed at 400 °C exhibits 28 nm surface roughness is ideal condition for the liberation of $Ag^+$, $Ta^+$ and $O^{2-}$ ions that lies within the desirable range suggested by Siegel et al. (2011) and Rahmati et al. (2015a). High hydrophobicity as suggested by the mentioned results is very desirable for surgical instruments. The 78.7±2.1 ° contact angle of 400 °C annealed-S7 Ag/Ag-$Ta_2O_5$ thin film falls within the wanted range as recommended by the previous established research (Chang et al., 2014; Ponsonnet et al., 2003). Considerably hydrophobic surfaces demote the attachment of liquids, resists the microbial attachment and influence the cell proliferation.

Additionally, the XRD diffraction also confirms the elemental distribution analysis results for the single layer Ag-$Ta_2O_5$ and multilayer Ag/Ag-$Ta_2O_5$ thin film surface (Table 4.2 and 4.7). The existence of segregated Ag on the coated thin film is further supported by the dominant Ag peak in the diffraction pattern from the $2\theta$ positions of 38.12 to 81.55 ° in Figure 4.8, Figure 4.9, Figure 4.17 and Figure 4.25. Furthermore, the electron bright field diffraction spot in the rings pattern from SAED analysis in Figure 4.11 is correlated with the crystallized segregated Ag surface of 400 °C annealed "$S_1$". In XPS analysis as illustrated in Figure 4.28 b, the absent of Ta spectra supported the results of FESEM-EDX and XRD.

This research provides insight study of the mechanical and biological properties of $AgTaO_3$ compound achieving by annealing the Ag-$Ta_2O_5$ thin film. In this work, a new phase $AgTaO_3$ is formed by the Ag-$Ta_2O_5$ reaction at high annealing temperature can

determine the efficiency of antibacterial and biocompatibility properties. The 400 °C annealed "$S_7$" with no $AgTaO_3$ exhibited an outstanding antibacterial and biocompatibility properties. The 700 °C annealed "$S_7$" which grouped in the same method is not perform as an antibacterial agent, and has a poor biocompatibility owing to its $AgTaO_3$ precipitation.

Therefore, incorporating Ag-$Ta_2O_5$ and Ag/Ag-$Ta_2O_5$ nanocomposite, the homogeneity of particles (limiting bacterial adhesion) in the as-deposited sample, the segregated Ag microstructure (efficient antibacterial activity) (Sharratt, 2006), strong hydrophobic character (Wendlandt et al., 2016) improved adhesion strength (Othman et al., 2015), and thermal stability (able to sustain sterilization thermal cycles) (Hryniewicz & Rokicki, 2018), excellent antibacterial performance, hBMSCs attachment and cell proliferation were achieved in this work may contribute to superior Nano composite thin film based surgical instruments (Chan et al., 2017).

# CHAPTER 5: CONCLUSION AND FUTURE WORK

This chapter presents the conclusions from this research and future works suggestions. The three main objectives of the present research were to: 1) develop single layer Ag-$Ta_2O_5$ and multilayer Ag/Ag-$Ta_2O_5$ thin films on SS 316L by using PVD magnetron sputtering, 2) improve the adhesion strength and crystallinity of as-deposited films by post annealing and 3) characterize the physicochemical properties (microstructure, elemental composition, hydrophobicity, micro mechanical, morphology, phase, structure, surface chemistry), antibacterial and biocompatibility performance of the deposited thin films. Thus, the conclusions were drawn in addressing these objectives.

## 5.1 Conclusions

Single layer Ag-$Ta_2O_5$ and multilayer Ag/Ag-$Ta_2O_5$ nanocomposite thin films were successfully developed and deposited using PVD magnetron sputtering onto SS 316L for surgical instrument applications.

In this study, the as-deposited "$S_7$" using Method C achieved the optimum conditions for the adhesion strength of as-deposited PVD multilayer Ag/Ag-$Ta_2O_5$ on stainless steel 316L. The as-deposited "$S_7$" that was run at 200 W power, 45 sccm argon flow rate, 6 sccm oxygen flow rate and 250 °C substrate temperature resulted in 1302±26 mN adhesion strength. With all methods, the as-deposited sample exhibited comparably low adhesion strength, low crystallinity and higher wettability.

The mechanical stability was significantly improved by post annealing both as-deposited single layer Ag-$Ta_2O_5$ and multilayer Ag/Ag-$Ta_2O_5$. The annealing prompted significant segregation of Ag at the surface, and the enhancement of film adhesion strength and hydrophilicity properties. According to the adhesion strength evaluation,

the best thin film adhesion strength with 154 % improvement was achieved by annealing the as-deposited "$S_7$" at 400 ºC (3310±84 mN) with Method C. Upon annealing, a new $AgTaO_3$ phase precipitated in the "$S_7$" thin film annealed at temperatures in the 550–700 °C range and 2 °C/min ramp rate.

The $AgTaO_3$ phase also formed in "$S_1$" annealed at 500 °C and 5 °C/min. However, in the "$S_1$" sample annealed at the same temperature and a lower ramp rate (2 °C/min) the $AgTaO_3$ phase was absent. This $AgTaO_3$ compound actually deteriorated the adhesion strength, antibacterial performance and biocompatibility properties. "$S_7$" (Ag/Ag-$Ta_2O_5$ thin film) annealed at 400 °C with method C exhibited superior antibacterial performance against *S. aureus* and *E. coli*. The *in vivo* test demonstrated that "$S_7$" annealed at 400 °C is extremely biocompatible with hBMSCs. Thus, the best adhesion strength, excellent antibacterial performance and outstanding biocompatibility properties were obtained with method C.

In summary, the SS 316L coated with annealed Ag-$Ta_2O_5$ and Ag/Ag-$Ta_2O_5$ achieved in this research may contribute to the development of highly satisfactory thin film-based surgical instruments. The findings from this study can be beneficial to the global healthcare environment and economy by reducing infections and treatment costs. Therefore, the need for antibiotics will diminish, consequently lowering the risk of antibiotic resistance that is a threat to humans.

## 5.2 Future work

Further research will be carried out to methodically study the effects of $AgTaO_3$ precipitation on the mechanical and biological behavior of an Ag-$Ta_2O_5$ nanocomposite layer. An alternative process comprising a rapid thermal annealing (RTA) system may be utilized to crystallize the as-deposited film to avoid $AgTaO_3$ precipitation.

.

## REFERENCES


Abenojar, J., Velasco, F., Torralba, J., Bas, J., Calero, J., & Marce, R. (2002). Reinforcing 316L stainless steel with intermetallic and carbide particles. *Materials Science and Engineering: A, 335*(1-2), 1-5.

Achache, S., Alhussein, A., Guelorget, B., Salut, R., Francois, M., & Sanchette, F. (2018). Effect of oxygen addition on microstructure and mechanical properties of quaternary TNTZ superelastic thin films obtained by magnetron sputtering. *Materials chemistry and physics, 217*, 262-269.

Adochite, R., Munteanu, D., Torrell, M., Cunha, L., Alves, E., Barradas, N., . . . Eyidi, D. (2012). The influence of annealing treatments on the properties of Ag: TiO2 nanocomposite films prepared by magnetron sputtering. *Applied surface science, 258*(8), 4028-4034.

Aijaz, A., Ji, Y.-X., Montero, J., Niklasson, G. A., Granqvist, C. G., & Kubart, T. (2016). Low-temperature synthesis of thermochromic vanadium dioxide thin films by reactive high power impulse magnetron sputtering. *Solar Energy Materials and Solar Cells, 149*, 137-144.

Akter, M., Sikder, M. T., Rahman, M. M., Ullah, A. A., Hossain, K. F. B., Banik, S., . . . Kurasaki, M. (2017). A systematic review on silver nanoparticles-induced cytotoxicity: Physicochemical properties and perspectives. *Journal of Advanced Research*, *9*, 1-16.

Alias, R., Mahmoodian, R., Shukor, M. H. A., Yew, B. S., & Muhamad, M. (2018). *Enhancement of as-sputtered silver-tantalum oxide thin film coating on biomaterial stainless steel by surface thermal treatment.* Paper presented at the AIP Conference Proceedings.

Alishahi, M., Mahboubi, F., Khoie, S. M., Aparicio, M., Lopez-Elvira, E., Méndez, J., & Gago, R. (2016). Structural properties and corrosion resistance of tantalum nitride coatings produced by reactive DC magnetron sputtering. *RSC Advances, 6*(92), 89061-89072.

Alvarez-Lorenzo, C., Garcia-Gonzalez, C. A., Bucio, E., & Concheiro, A. (2016). Stimuli-responsive polymers for antimicrobial therapy: drug targeting, contact-killing surfaces and competitive release. *Expert opinion on drug delivery, 13*(8), 1109-1119.

Alves, M., Grenho, L., Lopes, C., Borges, J., Vaz, F., Vaz, I., & Fernandes, M. (2018). Antibacterial effect and biocompatibility of a novel nanostructured ZnO-coated gutta-percha cone for improved endodontic treatment. *Materials Science and Engineering: C, 92*, 840-848.

Arias, C. A., & Murray, B. E. (2015). A new antibiotic and the evolution of resistance. *New England Journal of Medicine, 372*(12), 1168-1170.

Arslan, E., Totik, Y., Celik, A., & Efeoglu, I. (2010). Effect of annealing on adhesion of TiB2 films deposited by pulsed magnetron sputtering. *Surface Engineering, 26*(8), 567-570.

Atefyekta, S., Ercan, B., Karlsson, J., Taylor, E., Chung, S., Webster, T. J., & Andersson, M. (2016). Antimicrobial performance of mesoporous titania thin films: role of pore size, hydrophobicity, and antibiotic release. *International Journal of Nanomedicine, 11*, 977.

Bah, S. T., Ba, C. O., D'Auteuil, M., Ashrit, P., Sorelli, L., & Vallée, R. (2016). Fabrication of TaOxNy thin films by reactive ion beam-assisted ac double magnetron sputtering for optical applications. *Thin Solid Films, 615*, 351-357.

Bai, L., Hang, R., Gao, A., Zhang, X., Huang, X., Wang, Y., . . . Chu, P. K. (2015). Nanostructured titanium–silver coatings with good antibacterial activity and cytocompatibility fabricated by one-step magnetron sputtering. *Applied Surface Science, 355*, 32-44.

Balas, M., Dumitrache, F., Badea, M., Fleaca, C., Badoi, A., Tanasa, E., & Dinischiotu, A. (2018). Coating Dependent In Vitro Biocompatibility of New Fe-Si Nanoparticles. *Nanomaterials, 8*(7), 495.

Balouiri, M., Sadiki, M., & Ibnsouda, S. K. (2016). Methods for in vitro evaluating antimicrobial activity: A review. *Journal of Pharmaceutical Analysis, 6*(2), 71-79.

Bekmurzayeva, A., Duncanson, W. J., Azevedo, H. S., & Kanayeva, D. (2018). Surface modification of stainless steel for biomedical applications: Revisiting a century-old material. *Materials Science and Engineering: C*.

Blackford, J. T., Blackford, L. W., Disegi, J., & Bohner, M. (2006). Chapter 9 - Biomaterials, Surgical Implants, and Instruments. In J. A. A. A. Stick (Ed.), *Equine Surgery (Third Edition)* (pp. 96-111). Saint Louis: W.B. Saunders.

Blees, M., Winkelman, G., Balkenende, A., & Den Toonder, J. (2000). The effect of friction on scratch adhesion testing: application to a sol–gel coating on polypropylene. *Thin Solid Films, 359*(1), 1-13.

Boi, M., Bianchi, M., Gambardella, A., Liscio, F., Kaciulis, S., Visani, A., . . . Lungaro, L. (2015). Tough and adhesive nanostructured calcium phosphate thin films deposited by the pulsed plasma deposition method. *RSC Advances, 5*(96), 78561-78571.

B , F., Giner, I., Keller, A., Grundmeier, G., & Fischer, H. (2016). Plasma-Enhanced Chemical Vapor Deposition (PE-CVD) yields better Hydrolytical Stability of Biocompatible SiOx Thin Films on Implant Alumina Ceramics compared to Rapid Thermal Evaporation Physical Vapor Deposition (PVD). *ACS applied materials & interfaces, 8*(28), 17805-17816.

Bosetti, M., Masse, A., Tobin, E., & Cannas, M. (2002). Silver coated materials for external fixation devices: in vitro biocompatibility and genotoxicity. *Biomaterials, 23*(3), 887-892.

Bouala, G. N., Etiemble, A., Der Loughian, C., Langlois, C., Pierson, J.-F., & Steyer, P. (2018). Silver influence on the antibacterial activity of multi-functional Zr-Cu based thin film metallic glasses. *Surface and Coatings Technology, 343*, 108-114.

Bruce, M., McConnell, I., Will, R., & Ironside, J. (2001). Detection of variant Creutzfeldt-Jakob disease infectivity in extraneural tissues. *The Lancet, 358*(9277), 208-209.

Bunting, A., & Cheung, R. (2016). Evaluation of residual stress in sputtered tantalum thin-film. *Applied Surface Science, 371*, 571-575.

Burd, A., Kwok, C. H., Hung, S. C., Chan, H. S., Gu, H., Lam, W. K., & Huang, L. (2007). A comparative study of the cytotoxicity of silver-based dressings in monolayer cell, tissue explant, and animal models. *Wound repair and regeneration, 15*(1), 94-104.

Bushroa, A., Masjuki, H., Muhamad, M., & Beake, B. (2011). Optimized scratch adhesion for TiSiN coatings deposited by a combination of DC and RF sputtering. *Surface and Coatings Technology, 206*(7), 1837-1844.

Campa, C. C., Silva, R. L., Margaria, J. P., Pirali, T., Mattos, M. S., Kraemer, L. R., . . . Dalmarco, E. M. (2018). Inhalation of the prodrug PI3K inhibitor CL27c improves lung function in asthma and fibrosis. *Nature communications, 9*(1), 5232.

Campoccia, D., Montanaro, L., & Arciola, C. R. (2013). A review of the biomaterials technologies for infection-resistant surfaces. *Biomaterials, 34*(34), 8533-8554.

Çetinörgü-Goldenberg, E., Klemberg-Sapieha, J.-E., & Martinu, L. (2012). Effect of postdeposition annealing on the structure, composition, and the mechanical and optical characteristics of niobium and tantalum oxide films. *Applied optics, 51*(27), 6498-6507.

Ceviker, N., Keskil, S., & Baykaner, K. (1998). A new coated bipolar coagulator. *Acta neurochirurgica, 140*(6), 619-620.

Chan, C.-W., Carson, L., Smith, G. C., Morelli, A., & Lee, S. (2017). Enhancing the antibacterial performance of orthopaedic implant materials by fibre laser surface engineering. *Applied Surface Science, 404*, 67-81.

Chandrasekaran, S., Abbott, A., Miller, S., Zimmer, B., Weinstein, M., Thrupp, L., . . . Kirn, T. (2018). Direct-from-blood culture disk diffusion to determine antimicrobial susceptibility of Gram-negative bacteria: Preliminary report from the Clinical and Laboratory Standards Institute Methods Development and Standardization Working Group. *Journal of Clinical Microbiology*, JCM. 01678-01617.

Chang, H.-I., & Wang, Y. (2011). Cell responses to surface and architecture of tissue engineering scaffolds. In *Regenerative medicine and tissue engineering-cells and biomaterials*: InTech.

Chang, Y.-Y., Huang, H.-L., Chen, H.-J., Lai, C.-H., & Wen, C.-Y. (2014). Antibacterial properties and cytocompatibility of tantalum oxide coatings. *Surface and Coatings Technology, 259*, 193-198.

Chen, Q., & Thouas, G. A. (2015). Metallic implant biomaterials. *Materials Science and Engineering: R: Reports, 87*, 1-57.

Chen, W., Liu, Y., Courtney, H., Bettenga, M., Agrawal, C., Bumgardner, J., & Ong, J. (2006). In vitro anti-bacterial and biological properties of magnetron co-sputtered silver-containing hydroxyapatite coating. *Biomaterials, 27*(32), 5512-5517.

Chen, Y.-W., Hsieh, S.-C., Yang, Y.-C., Hsu, S.-h., Kung, M.-L., Lin, P.-Y., . . . Hung, H.-S. (2018). Functional engineered mesenchymal stem cells with fibronectin-gold composite coated catheters for vascular tissue regeneration. *Nanomedicine: Nanotechnology, Biology and Medicine, 14*(3), 699-711.

Chiu, H. T., Sukachonmakul, T., Kuo, M. T., Wang, Y. H., & Wattanakul, K. (2014). Surface modification of aluminum nitride by polysilazane and its polymer-derived amorphous silicon oxycarbide ceramic for the enhancement of thermal conductivity in silicone rubber composite. *Applied Surface Science, 292*, 928-936.

Chou, H.-T., & Hsu, H.-C. (2016). The effect of annealing temperatures to prepare ZnO seeds layer on ZnO nanorods array/TiO 2 nanoparticles photoanode. *Solid-State Electronics, 116*, 15-21.

Chuang, K.-T., Abdullah, H., Leu, S.-J., Cheng, K.-B., Kuo, D.-H., Chen, H.-C., . . . Hu, W.-T. (2017). Metal oxide composite thin films made by magnetron sputtering for bactericidal application. *Journal of Photochemistry and Photobiology A: Chemistry, 337*, 151-164.

Cloutier, M., Mantovani, D., & Rosei, F. (2015). Antibacterial coatings: challenges, perspectives, and opportunities. *Trends in biotechnology, 33*(11), 637-652.

Coad, B. R., Griesser, H. J., Peleg, A. Y., & Traven, A. (2016). Anti-infective surface coatings: design and therapeutic promise against device-associated infections. *PLoS pathogens, 12*(6), 1005598.

Cornejo-Juárez, P., Vilar-Compte, D., Pérez-Jiménez, C., Namendys-Silva, S., Sandoval-Hernández, S., & Volkow-Fernández, P. (2015). The impact of hospital-acquired infections with multidrug-resistant bacteria in an oncology intensive care unit. *International Journal of Infectious Diseases, 31*, 31-34.

Dai, X., Zhou, A., Feng, L., Wang, Y., Xu, J., & Li, J. (2014). Molybdenum thin films with low resistivity and superior adhesion deposited by radio-frequency magnetron sputtering at elevated temperature. *Thin Solid Films, 567*, 64-71.

Dancer, S. J., Stewart, M., Coulombe, C., Gregori, A., & Virdi, M. (2012). Surgical site infections linked to contaminated surgical instruments. *Journal of Hospital Infection, 81*(4), 231-238.

Dasgupta, S., Das, S., Chawan, N. S., & Hazra, A. (2015). Nosocomial infections in the intensive care unit: Incidence, risk factors, outcome and associated pathogens in a public tertiary teaching hospital of Eastern India. *Indian journal of critical care medicine: peer-reviewed, official publication of Indian Society of Critical Care Medicine, 19*(1), 14.

De Las Heras, E., Ybarra, G., Lamas, D., Cabo, A., Dalibon, E. L., & Brühl, S. P. (2017). Plasma nitriding of 316L stainless steel in two different N2-H2 atmospheres-Influence on microstructure and corrosion resistance. *Surface and Coatings Technology, 313*, 47-54.

de Lissovoy, G., Fraeman, K., Hutchins, V., Murphy, D., Song, D., & Vaughn, B. B. (2009). Surgical site infection: incidence and impact on hospital utilization and treatment costs. *American journal of infection control, 37*(5), 387-397.

Dervaux, J., Cormier, P.-A., Moskovkin, P., Douheret, O., Konstantinidis, S., Lazzaroni, R., . . . Snyders, R. (2017). Synthesis of nanostructured Ti thin films by combining glancing angle deposition and magnetron sputtering: A joint experimental and modeling study. *Thin Solid Films, 636*, 644-657.

Dixit, S., Popat, P. P., Rawat, S. S., & Sivarajan, S. (2016). Multilayer PVD Surface Engineered Coatings for Sheet Metal Forming Tools. *Indian Journal of Science and Technology, 9*(41).

Dolgin, E. (2010). Sequencing of superbugs seen as key to combating their spread. In: Nature Publishing Group.

Dominguez-Wong, C., Loredo-Becerra, G., Quintero-González, C., Noriega-Treviño, M., Compeán-Jasso, M., Niño-Martínez, N., . . . Ruiz, F. (2014). Evaluation of the antibacterial activity of an indoor waterborne architectural coating containing Ag/TiO2 under different relative humidity environments. *Materials Letters, 134*, 103-106.

Donaldson, O. K., Hattar, K., & Trelewicz, J. R. (2016). Metastable tantalum oxide formation during the devitrification of amorphous tantalum thin films. *Journal of the American Ceramic Society, 99*(11), 3775-3783.

Dualeh, A., Tétreault, N., Moehl, T., Gao, P., Nazeeruddin, M. K., & Grätzel, M. (2014). Effect of annealing temperature on film morphology of organic–inorganic hybrid pervoskite solid-state solar cells. *Advanced Functional Materials, 24*(21), 3250-3258.

Elahi, A. S., & Ghoranneviss, M. (2016). Review of the chemical vapour deposition applications for the microelectronic devices. *International Journal of Materials and Product Technology, 52*(3-4), 353-361.

Etiemble, A., Der Loughian, C., Apreutesei, M., Langlois, C., Cardinal, S., Pelletier, J., . . . Steyer, P. (2016). Innovative Zr-Cu-Ag thin film metallic glass deposed by magnetron PVD sputtering for antibacterial applications. *Journal of Alloys and Compounds*, 707, 155-161.

Fang, D., Yao, P., & Li, H. (2014). Influence of annealing temperature on the structural and optical properties of Mg–Al co-doped ZnO thin films prepared via sol–gel method. *Ceramics International, 40*(4), 5873-5880.

Franci, G., Falanga, A., Galdiero, S., Palomba, L., Rai, M., Morelli, G., & Galdiero, M. (2015). Silver nanoparticles as potential antibacterial agents. *Molecules, 20*(5), 8856-8874.

Gassner, M., de Figueiredo, M. R., Schalk, N., Franz, R., Weiß, C., Rudigier, H., . . . Czettl, C. (2016). Energy consumption and material fluxes in hard coating deposition processes. *Surface and Coatings Technology, 299*, 49-55.

Ge, H., Zhang, J., Yuan, Y., Liu, J., Liu, R., & Liu, X. (2017). Preparation of organic–inorganic hybrid silica nanoparticles with contact antibacterial properties and their application in UV-curable coatings. *Progress in Organic Coatings, 106*, 20-26.

Gleich, S., Soler, R., Fager, H., Bolvardi, H., Achenbach, J.-O., Hans, M., . . . Scheu, C. (2018). Modifying the nanostructure and the mechanical properties of Mo 2 BC hard coatings: Influence of substrate temperature during magnetron sputtering. *Materials & Design, 142*, 203-211.

Gliga, A. R., Skoglund, S., Wallinder, I. O., Fadeel, B., & Karlsson, H. L. (2014). Size-dependent cytotoxicity of silver nanoparticles in human lung cells: the role of cellular uptake, agglomeration and Ag release. *Particle and fibre toxicology, 11*(1), 11.

Gnanarajan, S., & Lam, S. (2008). Evolution of epitaxial Ta 2 O 5 and Ta 2 O films during thermal oxidation of epitaxial tantalum films on sapphire substrates. *Journal of Vacuum Science & Technology A: Vacuum, Surfaces, and Films, 26*(3), 494-497.

Gnanarajan, S., Lam, S., & Foley, C. (2007). Optically transparent and electrically conducting epitaxial Ta 2 O films. *Journal of applied physics, 101*(6), 063535.

Gu, J., Zhong, Z., Chen, S., Yang, C., & Hou, J. (2014). *Effect of Argon Gas Pressure on Optical Properties of Zinc Oxide Thin Films Deposited by RF Magnetron Sputtering Technique.* Paper presented at the Advanced Materials Research.

Guzman, M., Dille, J., & Godet, S. (2012). Synthesis and antibacterial activity of silver nanoparticles against gram-positive and gram-negative bacteria. *Nanomedicine: Nanotechnology, Biology and Medicine, 8*(1), 37-45.

Hajipour, M. J., Fromm, K. M., Ashkarran, A. A., de Aberasturi, D. J., de Larramendi, I. R., Rojo, T., . . . Mahmoudi, M. (2012). Antibacterial properties of nanoparticles. *Trends in biotechnology, 30*(10), 499-511.

Hassan, M., Bushroa, A., & Mahmoodian, R. (2015). Identification of critical load for scratch adhesion strength of nitride-based thin films using wavelet analysis and a proposed analytical model. *Surface and Coatings Technology, 277*, 216-221.

Hee, A. C., Jamali, S. S., Bendavid, A., Martin, P. J., Kong, C., & Zhao, Y. (2016). Corrosion behaviour and adhesion properties of sputtered tantalum coating on Ti6Al4V substrate. *Surface and Coatings Technology, 307*, 666-675.

Heim, W. P., & Brassell, J. (2017). Method for coating surgical intruments: U.S. Patent Application No. 15/293,395.

Hergenrother, R., Chee, U. H., & Schaller, L. (1995). Guidewire and method of pretreating metal surfaces for subsequent polymer coating: U.S. Patent 5,443,455.

Hollstein, F., & Louda, P. (1999). Bio-compatible low reflective coatings for surgical tools using reactive dc-magnetron sputtering and arc evaporation—a comparison regarding steam sterilization resistance and nickel diffusion. *Surface and Coatings Technology, 120*, 672-681.

Hou, X., Qin, H., Gao, H., Mankoci, S., Zhang, R., Zhou, X., . . . Sahai, N. (2017). A systematic study of mechanical properties, corrosion behavior and biocompatibility of AZ31B Mg alloy after ultrasonic nanocrystal surface modification. *Materials Science and Engineering: C, 78*, 1061-1071.

Hryniewicz, T., & Rokicki, R. (2018). Modification of Nitinol Biomaterial for Medical Applications. *World Scientific News, 96*, 35-58.

Hu, J., Muratore, C., & Voevodin, A. A. (2007). Silver diffusion and high-temperature lubrication mechanisms of YSZ–Ag–Mo based nanocomposite coatings. *Composites Science and Technology, 67*(3-4), 336-347.

Hu, S., Shaner, M. R., Beardslee, J. A., Lichterman, M., Brunschwig, B. S., & Lewis, N. S. (2014). Amorphous TiO2 coatings stabilize Si, GaAs, and GaP photoanodes for efficient water oxidation. *Science, 344*(6187), 1005-1009.

Huang, H.-L., Chang, Y.-Y., Chen, H.-J., Chou, Y.-K., Lai, C.-H., & Chen, M. Y. (2014a). Antibacterial properties and cytocompatibility of tantalum oxide coatings with different silver content. *Journal of Vacuum Science & Technology A: Vacuum, Surfaces, and Films, 32*(2), 02B117.

Huff, M. A., & Sunal, P. (2015). Method and system for integrated MEMS and NEMS using deposited thin films having pre-determined stress states: U.S. Patent No. 9,053,929.

Hussain, S., Hess, K., Gearhart, J., Geiss, K., & Schlager, J. (2005). In vitro toxicity of nanoparticles in BRL 3A rat liver cells. *Toxicology in vitro, 19*(7), 975-983.

Iconaru, S. L., Chapon, P., Le Coustumer, P., & Predoi, D. (2014). Antimicrobial activity of thin solid films of silver doped hydroxyapatite prepared by sol-gel method. *The Scientific World Journal, 2014*.

Imamura, H., Adachi, T., Kin, T., Ono, S., Sakai, Y., Adachi, T., . . . Shapiro, A. J. (2018). An engineered cell sheet composed of human islets and human fibroblast, bone marrow–derived mesenchymal stem cells, or adipose–derived mesenchymal stem cells: An in vitro comparison study. *Islets*, 1-11.

Incerti, L., Rota, A., Valeri, S., Miguel, A., García, J., Rodríguez, R., & Osés, J. (2011). Nanostructured self-lubricating CrN-Ag films deposited by PVD arc discharge and magnetron sputtering. *Vacuum, 85*(12), 1108-1113.

Ivanova, A. A., Surmenev, R. A., Surmeneva, M. A., Mukhametkaliyev, T., Loza, K., Prymak, O., & Epple, M. (2015). Hybrid biocomposite with a tunable antibacterial activity and bioactivity based on RF magnetron sputter deposited coating and silver nanoparticles. *Applied Surface Science, 329*, 212-218.

Ivanova, A. A., Surmeneva, M. A., Tyurin, A., Pirozhkova, T., Shuvarin, I., Prymak, O., . . . Surmenev, R. A. (2016). Fabrication and physico-mechanical properties of thin magnetron sputter deposited silver-containing hydroxyapatite films. *Applied Surface Science, 360*, 929-935.

Jain, R., Faith, N. G., Milkowski, A., Nelson, K., Busche, D., Lynn, D. M., . . . Abbott, N. L. (2016). Using Chemoattractants to Lure Bacteria to Contact-Killing Surfaces. *Angewandte Chemie, 128*(19), 5792-5796.

Jamuna-Thevi, K., Bakar, S., Ibrahim, S., Shahab, N., & Toff, M. (2011). Quantification of silver ion release, in vitro cytotoxicity and antibacterial properties of nanostuctured Ag doped TiO2 coatings on stainless steel deposited by RF magnetron sputtering. *Vacuum, 86*(3), 235-241.

Jiang, J., Wang, Y., Nie, X., Xiao, G. J. M., & Design. (2016). Microstructure evolution of semisolid billet of nano-sized SiCp/7075 aluminum matrix composite during partial remelting process. *Materials & Design*, *96*, 36-43.

Jiang, Y., Jahagirdar, B. N., Reinhardt, R. L., Schwartz, R. E., Keene, C. D., Ortiz-Gonzalez, X. R., . . . Blackstad, M. (2002). Pluripotency of mesenchymal stem cells derived from adult marrow. *Nature, 418*(6893), 41.

Jin, W., Wang, G., Lin, Z., Feng, H., Li, W., Peng, X., . . . Chu, P. K. (2017). Corrosion resistance and cytocompatibility of tantalum-surface-functionalized biomedical ZK60 Mg alloy. *Corrosion Science, 114*, 45-56.

Jingjing, Z., Zehua, W., Pinghua, L., & Zhiqiang, W. (2015). Adhesion properties and fracture mechanism of plasma sprayed NiCrAl/Al2O3–13wt.% TiO2 coatings by post annealing. *Journal of Adhesion Science and Technology, 29*(4), 256-270.

Jocham, C., Schmidt, T. W., Wuzella, G., Teischinger, A., & Kandelbauer, A. (2011). Adhesion improvement of powder coating on medium density fibreboard (MDF) by thermal pre-treatment. *Journal of Adhesion Science and Technology, 25*(15), 1937-1946.

Kaviyarasu, K., Magdalane, C. M., Kanimozhi, K., Kennedy, J., Siddhardha, B., Reddy, E. S., . . . Letsholathebe, D. (2017). Elucidation of photocatalysis, photoluminescence and antibacterial studies of ZnO thin films by spin coating method. *Journal of Photochemistry and Photobiology B: Biology, 173*, 466-475.

Khaydukov, Y., Morari, R., Lenk, D., Zdravkov, V., Merkel, D., Seidlhofer, B.-K., . . . Steitz, R. (2017). *Magnetic state of Nb (l-7nm)/Cu30Ni70 (6nm) superlattices revealed by Polarized Neutron Reflectometry and SQUID magnetometry.* Paper presented at the Journal of Physics: Conference Series.

Kleinstreuer, N. C., Hoffmann, S., Alépée, N., Allen, D., Ashikaga, T., Casey, W., . . . Gellatly, N. (2018). Non-animal methods to predict skin sensitization (II): an assessment of defined approaches. *Critical reviews in toxicology, 48*(5), 359-374.

Klevens, R. M., Morrison, M. A., Nadle, J., Petit, S., Gershman, K., Ray, S., . . . Townes, J. M. (2007). Invasive methicillin-resistant Staphylococcus aureus infections in the United States. *298*(15), 1763-1771.

Köse, C., & Kacar, R. (2016). In Vitro Bioactivity and Corrosion Properties of Laser Beam Welded Medical Grade AISI 316L Stainless Steel in Simulated Body Fluid. *International Journal of Electrochemical Science, 11*, 2762-2777.

Köser, C. U., Holden, M. T., Ellington, M. J., Cartwright, E. J., Brown, N. M., Ogilvy-Stuart, A. L., . . . Harris, S. R. (2012). Rapid whole-genome sequencing for investigation of a neonatal MRSA outbreak. *New England Journal of Medicine, 366*(24), 2267-2275.

Kulinets, I. (2015). 1 - Biomaterials and their applications in medicine. In S. F. Amato & R. M. Ezzell (Eds.), *Regulatory Affairs for Biomaterials and Medical Devices* (pp. 1-10): Woodhead Publishing.

Kumar, S., Bhushan, P., & Bhattacharya, S. (2017a). Coatings on Surgical Tools and How to Promote Adhesion of Bio-Friendly Coatings on Their Surfaces. *Adhesion in Pharmaceutical, Biomedical, and Dental Fields*, 207.

Kumar, S. S., Sharma, A., Rao, G. M., & Suwas, S. (2017b). Investigations on the effect of substrate temperature on the properties of reactively sputtered zirconium carbide thin films. *Journal of Alloys and Compounds, 695*, 1020-1028.

Kumar, T. S., & Madhumathi, K. (2016). Antibiotic delivery by nanobioceramics. *Therapeutic delivery, 7*(8), 573-588.

Kyaw, H., Myint, M., Al-Harthi, S., Maekawa, T., Yanagisawa, K., Sellai, A., & Dutta, J. J. T. S. F. (2019). The influence of initial gold nanoparticles layer on migration of silver nanoparticles in silver/glass matrix. *Thin Solid Films.*

Lan, W.-C., Ou, S.-F., Lin, M.-H., Ou, K.-L., & Tsai, M.-Y. (2013). Development of silver-containing diamond-like carbon for biomedical applications. Part I: Microstructure characteristics, mechanical properties and antibacterial mechanisms. *Ceramics International, 39*(4), 4099-4104.

Lankoff, A., Sandberg, W. J., Wegierek-Ciuk, A., Lisowska, H., Refsnes, M., Sartowska, B., . . . Kruszewski, M. (2012). The effect of agglomeration state of silver and titanium dioxide nanoparticles on cellular response of HepG2, A549 and THP-1 cells. *Toxicology letters, 208*(3), 197-213.

Lázár, V., Singh, G. P., Spohn, R., Nagy, I., Horváth, B., Hrtyan, M., . . . C ő, B. (2013). Bacterial evolution of antibiotic hypersensitivity. *Molecular systems biology, 9*(1), 700.

Leaper, D. J. (2006). Silver dressings: their role in wound management. *International wound journal, 3*(4), 282-294.

Lee, G. J., Kim, H. S., Yoon, C. S., Kim, J., Park, I., & Lee, Y. P. (2013a). Optical and Structural Properties of Ag: Ta2O5 Nanocomposites. *Journal of nanoscience and nanotechnology, 13*(5), 3451-3454.

Lee, J.-h., Lee, Y. J., Cho, H.-j., & Shin, H. (2013b). Guidance of in vitro migration of human mesenchymal stem cells and in vivo guided bone regeneration using aligned electrospun fibers. *Tissue Engineering Part A, 20*(15-16), 2031-2042.

Lee, J., Liou, M.-L., & Duh, J.-G. (2017). The development of a Zr-Cu-Al-Ag-N thin film metallic glass coating in pursuit of improved mechanical, corrosion, and antimicrobial property for bio-medical application. *Surface and Coatings Technology, 310*, 214-222.

Lemire, J. A., Harrison, J. J., & Turner, R. J. (2013). Antimicrobial activity of metals: mechanisms, molecular targets and applications. *Nature Reviews Microbiology, 11*(6), 371.

Leng, Y., Chen, J., Yang, P., Sun, H., Wang, J., & Huang, N. (2006). The biocompatibility of the tantalum and tantalum oxide films synthesized by pulse metal vacuum arc source deposition. *Nuclear Instruments and Methods in Physics Research Section B: Beam Interactions with Materials and Atoms, 242*(1-2), 30-32.

Leslie, D. C., Waterhouse, A., Berthet, J. B., Valentin, T. M., Watters, A. L., Jain, A., . . . Donovan, K. (2014). A bioinspired omniphobic surface coating on medical devices prevents thrombosis and biofouling. *Nature biotechnology, 32*(11), 1134.

Li, X.-Y., Li, H.-J., Wang, Z.-J., Xia, H., Xiong, Z.-Y., Wang, J.-X., & Yang, B.-C. (2009). Effect of substrate temperature on the structural and optical properties of ZnO and Al-doped ZnO thin films prepared by dc magnetron sputtering. *Optics Communications, 282*(2), 247-252.

Li, Y., Qian, Y., Zhao, G., Xu, J., & Li, M. (2017). Preparation of Nb 2 AlC coating by DC magnetron sputtering and subsequent annealing. *Ceramics International*.

Liao, J., Anchun, M., Zhu, Z., & Quan, Y. (2010). Antibacterial titanium plate deposited by silver nanoparticles exhibits cell compatibility. *International Journal of Nanomedicine, 5*, 337.

Lin, S.-S., Huang, J.-L., & Lii, D.-F. (2004). The effects of rf power and substrate temperature on the properties of ZnO films. *Surface and Coatings Technology, 176*(2), 173-181.

Liu, J., Li, L., Wei, B., Wen, F., Cao, H., & Pei, Y. (2018a). Effect of sputtering pressure on the surface topography, structure, wettability and tribological performance of DLC films coated on rubber by magnetron sputtering. *Surface and Coatings Technology*.

Liu, L., Ye, S.-H., Gu, X., Russell, T., Xu, Z., Sankar, J., . . . Yun, Y. (2018b). Comparison of endothelial cell attachment on surfaces of biodegradable polymer-coated magnesium alloys in a microfluidic environment. *PloS one, 13*(10), e0205611.

Liu, Z. L., & Xiang, L. (2014). Effects of working pressure and substrate temperature on the structure and mechanical properties of nanocrystalline SiC thin films deposited by bias-enhanced hot filament chemical vapor deposition. *Thin Solid Films, 562*, 24-31.

Llopis-Hernández, V., Rico, P., Ballester-Beltrán, J., Moratal, D., & Salmerón-Sánchez, M. (2011). Role of Surface Chemistry in Protein Remodeling at the Cell-Material Interface. *PloS one, 6*(5), e19610.

Loch, D. A., & Ehiasarian, A. P. (2016). Study of the effect of RF-power and process pressure on the morphology of copper and titanium sputtered by ICIS. *Surface and Coatings Technolog y, 327, 200-206.*

Lopes, C., Gonçalves, C., Borges, J., Polcar, T., Rodrigues, M., Barradas, N., . . . Macedo, F. (2015). Evolution of the functional properties of titanium–silver thin films for biomedical applications: Influence of in-vacuum annealing. *Surface and Coatings Technology, 261*, 262-271.

Lu, Y.-M., Hwang, W.-S., Liu, W., & Yang, J. (2001). Effect of RF power on optical and electrical properties of ZnO thin film by magnetron sputtering. *Materials Chemistry and Physics, 72*(2), 269-272.

Lyness, A., Kraft, C., Picken, A., Harriman, J., & Thomas, R. (2018). Evaluation of a novel cyclic olefin polymer container system for the cryopreservation of adherent and suspension human cell types. *Cytotherapy, 20*(5), S67.

Mahan, J. E. (2000). Physical vapor deposition of thin films. *Physical Vapor Deposition of Thin Films, by John E. Mahan, pp. 336. ISBN 0-471-33001-9. Wiley-VCH, January 2000.*, 336.

Mahapatro, A. (2015). Bio-functional nano-coatings on metallic biomaterials. *Materials Science and Engineering: C, 55*, 227-251.

Maheshwari, S. U., Samuel, V. K., & Nagiah, N. (2014). Fabrication and evaluation of (PVA/HAp/PCL) bilayer composites as potential scaffolds for bone tissue regeneration application. *Ceramics International, 40*(6), 8469-8477.

Mazzi, A., Bazzanella, N., Orlandi, M., Edla, R., Patel, N., Fernandes, R., & Miotello, A. (2016). Physical vapor deposition of mixed-metal oxides based on Fe, Co and Ni as water oxidation catalysts. *Materials Science in Semiconductor Processing, 42*, 155-158.

Meng, F., & Sun, Z. (2009). A mechanism for enhanced hydrophilicity of silver nanoparticles modified TiO2 thin films deposited by RF magnetron sputtering. *Applied Surface Science, 255*(13-14), 6715-6720.

Meran, Z., Besinis, A., De Peralta, T., & Handy, R. D. (2018). Antifungal properties and biocompatibility of silver nanoparticle coatings on silicone maxillofacial prostheses in vitro. *Journal of Biomedical Materials Research Part B: Applied Biomaterials, 106*(3), 1038-1051.

Mikami, T., Minamida, Y., Koyanagi, I., & Houkin, K. (2007). Novel bipolar forceps with protein repellence using gold–polytetrafluoroethylene composite film. *Operative Neurosurgery, 60*(2), 157- 161.

Mishra, S. K., Teotia, A. K., Kumar, A., & Kannan, S. (2017). Mechanically tuned nanocomposite coating on titanium metal with integrated properties of biofilm inhibition, cell proliferation, and sustained drug delivery. *Nanomedicine: Nanotechnology, Biology and Medicine, 13*(1), 23-35.

Mohamad Zaidi, U. Z., Bushroa, A. R., Ghahnavyeh, R. R., & Mahmoodian, R. (2018). Crystallite size and microstrain: XRD line broadening analysis of AgSiN thin films. *Pigment & Resin Technology*.

Mohseni, E., Zalnezhad, E., & Bushroa, A. R. (2014). Comparative investigation on the adhesion of hydroxyapatite coating on Ti–6Al–4V implant: A review paper. *International Journal of Adhesion and Adhesives, 48*, 238-257.

Moreira, H., Costa-Barbosa, A., Marques, S. M., Sampaio, P., & Carvalho, S. (2017). Evaluation of cell activation promoted by tantalum and tantalum oxide coatings deposited by reactive DC magnetron sputtering. *Surface and Coatings Technology, 330*, 260-269.

Mulligan, C., Papi, P., & Gall, D. (2012). Ag transport in CrN–Ag nanocomposite coatings. *Thin Solid Films, 520*(22), 6774-6779.

Mungchamnankit, A., Horprathum, M., Chananonnawathorn, C., Patthanasettakul, V., Eiamchai, P., Thongmee, A., & Sukplang, P. (2016). *Fabrication and Characterization of Antibacterial Tantalum Oxide Thin Films Deposited by Reactive Magnetron Sputtering.* Paper presented at the Key Engineering Materials.

Muratore, C., Voevodin, A. A., Hu, J., Jones, J. G., & Zabinski, J. S. (2005). Growth and characterization of nanocomposite yttria-stabilized zirconia with Ag and Mo. *Surface and Coatings Technology, 200*(5-6), 1549-1554.

Nasab, M. B., & Hassan, M. R. (2010). Metallic biomaterials of knee and hip-A review. *Trends in Biomaterials & Artificial Organs, 24*(1), 69-82.

Navarre, S. W., & Steiman, H. R. (2002). Root-end fracture during retropreparation: a comparison between zirconium nitride-coated and stainless steel microsurgical ultrasonic instruments. *Journal of endodontics, 28*(4), 330-332.

Navarro, M., Michiardi, A., Castaño, O., & Planell, J. A. (2008). *Biomaterials in orthopaedics*, 5(27), 1137-1158.

Nejadnik, M. R., van der Mei, H. C., Norde, W., & Busscher, H. J. (2008). Bacterial adhesion and growth on a polymer brush-coating. *Biomaterials, 29*(30), 4117-4121.

Nouri, A., & Wen, C. (2015). Introduction to surface coating and modification for metallic biomaterials. In *Surface coating and modification of metallic biomaterials*, 3-60.

Oshkour, A. A., Pramanik, S., Mehrali, M., Yau, Y. H., Tarlochan, F., & Osman, N. A. A. (2015). Mechanical and physical behavior of newly developed functionally graded materials and composites of stainless steel 316L with calcium silicate and hydroxyapatite. *journal of the mechanical behavior of biomedical materials, 49*, 321-331.

Othman, M., Bushroa, A., & Abdullah, W. N. R. (2015). Evaluation techniques and improvements of adhesion strength for TiN coating in tool applications: a review. *Journal of Adhesion Science and Technology, 29*(7), 569-591.

Otieno, F., Airo, M., Ranganathan, K., & Wamwangi, D. (2016). Annealed silver-islands for enhanced optical absorption in organic solar cell. *Thin Solid Films, 598*, 177-183.

Otter, J. A., Yezli, S., & French, G. L. (2011). The role played by contaminated surfaces in the transmission of nosocomial pathogens. *Infection Control & Hospital Epidemiology, 32*(7), 687-699.

Page, K., Wilson, M., & Parkin, I. P. (2009). Antimicrobial surfaces and their potential in reducing the role of the inanimate environment in the incidence of hospital-acquired infections. *Journal of Materials Chemistry, 19*(23), 3819-3831.

Pal, S., Tak, Y. K., & Song, J. M. (2007). Does the antibacterial activity of silver nanoparticles depend on the shape of the nanoparticle? A study of the gram-negative bacterium Escherichia coli. *Applied and environmental microbiology, 73*(6), 1712-1720.

Pandey, P., Kunwar, S., Sui, M., Li, M.-Y., Zhang, Q., & Lee, J. (2018). Effect of Annealing Temperature on Morphological and Optical Transition of Silver Nanoparticles on c-Plane Sapphire. *Journal of nanoscience and nanotechnology, 18*(5), 3466-3477.

Parida, P., Behera, A., & Mishra, S. C. Classification of Biomaterials used in Medicine. (2012).

Park, J., Kim, D.-J., Kim, Y.-K., Lee, K.-H., Lee, K.-H., Lee, H., & Ahn, S. (2003). Improvement of the biocompatibility and mechanical properties of surgical tools with TiN coating by PACVD. *Thin Solid Films, 435*(1-2), 102-107.

Park, J., & Lakes, R. S. (2007). *Biomaterials: an introduction*: Springer Science & Business Media.

Peng, S., Yao, T., Yang, Y., Zhang, K., Jiang, J., Jin, K., . . . Wang, Y. (2016). Influences of the RF power ratio on the optical and electrical properties of GZO thin films by DC coupled RF magnetron sputtering at room temperature. *Physica B: Condensed Matter, 503*, 111-116.

Perez, I., Sosa, V., Gamboa, F., Galindo, J. T. E., Gonzalez, P. G. M., Enriquez-Carrejo, J. L., & Farias, R. (2018). Influence of post-deposition annealing on the chemical states of crystalline tantalum pentoxide films , 124(11), 792.

Plecko, M., Sievert, C., Andermatt, D., Frigg, R., Kronen, P., Klein, K., . . . Ferguson, S. (2012). Osseointegration and biocompatibility of different metal implants-a comparative experimental investigation in sheep. *BMC musculoskeletal disorders, 13*(1), 32.

Pokropinski, H., Hunter, A. W., Brennan, K. W., & Jamiolkowski, D. D. (2000). Ethylene-propylene coatings for suture s: U.S. Patent 6,083,243.

Ponsonnet, L., Reybier, K., Jaffrezic, N., Comte, V., Lagneau, C., Lissac, M., & Martelet, C. (2003). Relationship between surface properties (roughness, wettability) of titanium and titanium alloys and cell behaviour. *Materials Science and Engineering: C, 23*(4), 551-560.

Popa, A., Stan, G., Enculescu, M., Tanase, C., Tulyaganov, D., & Ferreira, J. (2015). Superior biofunctionality of dental implant fixtures uniformly coated with durable bioglass films by magnetron sputtering. *journal of the mechanical behavior of biomedical materials, 51*, 313-327.

Pozio, A., Alvisi, M., Pilloni, L., Valerini, D., & Giorgi, L. (2016). Durability study of PVD-catalysed cathode for polymer electrolyte fuel cells.

Qi, F., Chen, Y., Zheng, B., Zhou, J., Wang, X., Li, P., & Zhang, W. (2016). Facile growth of large-area and high-quality few-layer ReS 2 by physical vapour deposition. *Materials Letters, 184*, 324-327.

Rafieerad, A., Bushroa, A., Nasiri-Tabrizi, B., Vadivelu, J., Baradaran, S., Mesbah, M., & Zavareh, M. A. (2016). Mechanical properties, corrosion behavior and in-

vitro bioactivity of nanostructured Pd/PdO coating on Ti–6Al–7Nb implant. *Materials & Design, 103*, 10-24.

Rahmati, B., Sarhan, A. A., Zalnezhad, E., Kamiab, Z., Dabbagh, A., Choudhury, D., & Abas, W. (2015a). Development of Tantalum Oxide (Ta-O) thin film coating on biomedical Ti-6Al-4V alloy to enhance mechanical properties and biocompatibility. *Ceramics International* , 42(1), 466-480.

Rahmati, B., Zalnezhad, E., Sarhan, A. A., Kamiab, Z., Tabrizi, B. N., & Abas, W. (2015b). Enhancing the adhesion strength of tantalum oxide ceramic thin film coating on biomedical Ti–6Al–4V alloy by thermal surface treatment. *Ceramics International, 41*(10), 13055-13063.

Rai, M., Yadav, A., & Gade, A. (2009). Silver nanoparticles as a new generation of antimicrobials. *Biotechnology advances, 27*(1), 76-83.

Raj, P. D., Gupta, S., & Sridharan, M. (2014). Studies on Nanostructured V2O5 Deposited by Reactive DC Magnetron Sputtering. In *Physics of Semiconductor Devices* (pp. 573-576): Springer.

Rangari, V. K., Mohammad, G. M., Jeelani, S., Hundley, A., Vig, K., Singh, S. R., & Pillai, S. (2010). Synthesis of Ag/CNT hybrid nanoparticles and fabrication of their nylon-6 polymer nanocomposite fibers for antimicrobial applications. *Nanotechnology, 21*(9), 095102.

Raniero, W., Della Mea, G., & Campostrini, M. (2016). Functionalization of Surfaces with Optical Coatings Produced by PVD Magnetron Sputtering. In *Research Perspectives on Functional Micro-and Nanoscale Coatings*, 170-207.

Raza, M. R., Ahmad, F., Muhamad, N., Sulong, A. B., Omar, M., Akhtar, M. N., & Aslam, M. (2016). Effects of solid loading and cooling rate on the mechanical properties and corrosion behavior of powder injection molded 316 L stainless steel. *Powder Technology, 289*, 135-142.

Reddy, B. N. K., & Udayashankar, N. (2016). The effect of annealing temperature on the structural, morphological, mechanical and surface properties of intermetallic NiTi alloy thin films. *Surface and Coatings Technology, 5*, 62-71.

Rhandhawa, H. S. (1991). Method for coated surgical instruments and tools: U.S. Patent 4,981,756.

Rizwan, M., Alias, R., Zaidi, U. Z., Mahmoodian, R., & Hamdi, M. (2018). Surface modification of valve metals using plasma electrolytic oxidation for antibacterial applications: A review. *Journal of Biomedical Materials Research Part A, 106*(2), 590-605.

Saha, R., & Nix, W. D. (2002). Effects of the substrate on the determination of thin film mechanical properties by nanoindentation. *Acta materialia, 50*(1), 23-38.

Salman, A., Sharaha, U., Rodriguez-Diaz, E., Shufan, E., Riesenberg, K., Bigio, I. J., & Huleihel, M. (2017). Detection of antibiotic resistant Escherichia Coli bacteria

using infrared microscopy and advanced multivariate analysis. *Analyst, 142*(12), 2136-2144.

Salwiczek, M., Qu, Y., Gardiner, J., Strugnell, R. A., Lithgow, T., McLean, K. M., & Thissen, H. (2014). Emerging rules for effective antimicrobial coatings. *Trends in biotechnology, 32*(2), 82-90.

Sankar, M., Vishnu, J., Gupta, M., & Manivasagam, G. (2019). Magnesium-based alloys and nanocomposites for biomedical application. In *Applications of Nanocomposite Materials in Orthopedics*, 83-109.

Sarraf, M., Dabbagh, A., Abdul Razak, B., Mahmoodian, R., Nasiri-Tabrizi, B., Hosseini, H. R. M., . . . Sukiman, N. L. (2018). Highly-ordered TiO 2 nanotubes decorated with Ag 2 O nanoparticles for improved biofunctionality of Ti6Al4V. *Surface and Coatings Technology, 349*, 1008-1017.

Sarraf, M., Razak, B. A., Dabbagh, A., Nasiri-Tabrizi, B., Kasim, N. H. A., & Basirun, W. J. (2016). Optimizing PVD conditions for electrochemical anodization growth of well-adherent $Ta_2O_5$ nanotubes on Ti–6Al–4V alloy. *RSC Advances, 6*(82), 78999-79015.

Sarraf, M., Razak, B. A., Nasiri-Tabrizi, B., Dabbagh, A., Kasim, N. H. A., Basirun, W. J., & Sulaiman, E. B. (2017). Nanomechanical properties, wear resistance and in-vitro characterization of Ta2O5 nanotubes coating on biomedical grade Ti–6Al–4V. *journal of the mechanical behavior of biomedical materials, 66*, 159-171.

Sax, H., Bloemberg, G., Hasse, B., Sommerstein, R., Kohler, P., Achermann, Y., . . . Böttger, E. C. (2015). Prolonged outbreak of Mycobacterium chimaera infection after open-chest heart surgery. *Clinical Infectious Diseases, 61*(1), 67-75.

Secker, T., Hervé, R., Zhao, Q., Borisenko, K., Abel, E., & Keevil, C. (2012). Doped diamond-like carbon coatings for surgical instruments reduce protein and prion-amyloid biofouling and improve subsequent cleaning. *Biofouling, 28*(6), 563-569.

Shahverdi, A. R., Fakhimi, A., Shahverdi, H. R., & Minaian, S. (2007). Synthesis and effect of silver nanoparticles on the antibacterial activity of different antibiotics against Staphylococcus aureus and Escherichia coli. *Nanomedicine: Nanotechnology, Biology and Medicine, 3*(2), 168-171.

Sharratt, T. (2006). Bacteria resistant coating for surgical instrument: U.S. Patent Application 11/443,482.

Shevtsov, M. A., Yudintceva, N. M., Blinova, M. I., Voronkina, I. V., Suslov, D. N., Galibin, O. V., . . . Albul, A. V. (2018). Evaluation of the temporary effect of physical vapor deposition silver coating on resistance to infection in transdermal skin and bone integrated pylon with deep porosity. *Journal of Biomedical Materials Research Part B: Applied Biomaterials*.

Sidane, D., Chicot, D., Yala, S., Ziani, S., Khireddine, H., Iost, A., & Decoopman, X. (2015). Study of the mechanical behavior and corrosion resistance of hydroxyapatite sol–gel thin coatings on 316 L stainless steel pre-coated with titania film. *Thin Solid Films, 593*, 71-80.

Siegel, J., Krajcar, R., Kolská, Z., Hnatowicz, V., & Švorčík, V. (2011). Annealing of gold nanostructures sputtered on polytetrafluoroethylene. *Nanoscale research letters, 6*(1), 588.

Siegel, J., Polívková, M., Staszek, M., Kolářová, K., Rimpelová, S., & Švorčík, V. (2015). Nanostructured silver coatings on polyimide and their antibacterial response. *Materials Letters, 145*, 87-90.

Soenen, S. J., Parak, W. J., Rejman, J., & Manshian, B. (2015). (Intra) Cellular Stability of Inorganic Nanoparticles: Effects on Cytotoxicity, Particle Functionality, and Biomedical Applications. *Chemical reviews, 115*(5), 2109-2135.

Spellberg, B., Bartlett, J. G., & Gilbert, D. N. (2013). The future of antibiotics and resistance. *New England Journal of Medicine, 368*(4), 299-302.

Spellberg, B., & Gilbert, D. N. (2014). The future of antibiotics and resistance: a tribute to a career of leadership by John Bartlett. *Clinical Infectious Diseases, 59*(2), 71-75.

Srinivasan, N., Kain, V., Birbilis, N., Krishna, K. M., Shekhawat, S., & Samajdar, I. (2015). Near boundary gradient zone and sensitization control in austenitic stainless steel. *Corrosion Science, 100*, 544-555.

Stan, G., Marcov, D., Pasuk, I., Miculescu, F., Pina, S., Tulyaganov, D., & Ferreira, J. (2010). Bioactive glass thin films deposited by magnetron sputtering technique: The role of working pressure. *Applied Surface Science, 256*(23), 7102-7110.

Stan, G., Morosanu, C., Marcov, D., Pasuk, I., Miculescu, F., & Reumont, G. (2009). Effect of annealing upon the structure and adhesion properties of sputtered bio-glass/titanium coatings. *Applied Surface Science, 255*(22), 9132-9138.

Stan, G., Popa, A., Galca, A., Aldica, G., & Ferreira, J. (2013). Strong bonding between sputtered bioglass–ceramic films and Ti-substrate implants induced by atomic inter-diffusion post-deposition heat-treatments. *Applied Surface Science, 280*, 530-538.

Stuart, B. W., Gimeno-Fabra, M., Segal, J., Ahmed, I., & Grant, D. M. (2017). Mechanical, structural and dissolution properties of heat treated thin-film phosphate based glasses. *Applied Surface Science, 416*, 605-617.

Sugiyama, M., Akita, M., Alépée, N., Fujishiro, M., Hagino, S., Handa, Y., . . . Katoh, M. (2018). Comparative assessment of 24-hr primary skin irritation test and human patch test data with in vitro skin irritation tests according to OECD Test Guideline 439 (for quasi-drugs in Japan). *The Journal of toxicological sciences, 43*(12), 751-768.

Sumita, M., Hanawa, T., & Teoh, S. (2004). Development of nitrogen-containing nickel-free austenitic stainless steels for metallic biomaterials. *Materials Science and Engineering: C, 24*(6-8), 753-760.

Surmeneva, M. A., Kleinhans, C., Vacun, G., Kluger, P. J., Schönhaar, V., Müller, M., . . . Prymak, O. (2015). Nano-hydroxyapatite-coated metal-ceramic composite of iron-tricalcium phosphate: Improving the surface wettability, adhesion and proliferation of mesenchymal stem cells in vitro. *Colloids and Surfaces B: Biointerfaces, 135*, 386-393.

Surmeneva, M. A., Sharonova, A. A., Chernousova, S., Prymak, O., Loza, K., Tkachev, M. S., . . . Surmenev, R. A. (2017). Incorporation of silver nanoparticles into magnetron-sputtered calcium phosphate layers on titanium as an antibacterial coating. *Colloids and Surfaces B: Biointerfaces* , 156, 104-113.

Suzuki, S., & Ueno, K. (2016). Apparent contact angle calculated from a water repellent model with pinning effect. *Langmuir, 33*(1), 138-143.

Swartjes, J., Sharma, P., Kooten, T., Van der Mei, H., Mahmoudi, M., Busscher, H., & Rochford, E. (2015). Current developments in antimicrobial surface coatings for biomedical applications. *Current medicinal chemistry, 22*(18), 2116-2129.

Tang, C., Klimenkov, M., Jaentsch, U., Leiste, H., Rinke, M., Ulrich, S., . . . Stueber, M. (2017). Synthesis and characterization of Ti 2 AlC coatings by magnetron sputtering from three elemental targets and ex-situ annealing. *Surface and Coatings Technology, 309*, 445-455.

Tong, X., Zhang, H., & Li, D. (2015). Effect of annealing treatment on mechanical properties of nanocrystalline α-iron: an atomistic study. *Scientific reports, 5*, 8459.

Tong, Z., Sant, S., Khademhosseini, A., & Jia, X. (2011). Controlling the Fibroblastic Differentiation of Mesenchymal Stem Cells Via the Combination of Fibrous Scaffolds and Connective Tissue Growth Factor. *Tissue Engineering Part A, 17*(21-22), 2773-2785.

Tran, P. A., Hocking, D. M., & O'Connor, A. J. (2015). In situ formation of antimicrobial silver nanoparticles and the impregnation of hydrophobic polycaprolactone matrix for antimicrobial medical device applications. *Materials Science and Engineering: C, 47*, 63-69.

Uday, M., Ahmad-Fauzi, M., Noor, A. M., & Rajoo, S. (2016). *Current Issues and Problems in the Joining of Ceramic to Metal*: Dr Mahadzir Ishak (Ed.), InTech.

Umi, Z., & Mahmoodian, R. (2017). *Comparative study on microstructure, crystallite size and lattice strain of as-deposited and thermal treatment silver silicon nitride coating on Ti6Al4V alloy.* Paper presented at the IOP Conference Series: Materials Science and Engineering, Kuala Lumpur, Malaysia.

Vanags, L. Z., Tan, J. T., Santos, M., Michael, P. S., Ali, Z., Bilek, M. M., . . . Bursill, C. A. (2017). Plasma activated coating immobilizes apolipoprotein AI to

stainless steel surfaces in its bioactive form and enhances biocompatibility. *Nanomedicine: Nanotechnology, Biology and Medicine, 13*(7), 2141-2150.

Varlashkin, P. (2011). Approaches to quantification of amorphous content in crystalline drug substance by powder X-ray diffraction. *American Pharmaceutical Review, 14*(1).

Velasco, S. C., Cavaleiro, A., & Carvalho, S. (2016). Functional properties of ceramic-Ag nanocomposite coatings produced by magnetron sputtering. *Progress in Materials Science, 84*, 158-191.

Velickova, N., & Milev, M. (2017). Micronucleus Assay as Genotoxicity Method to Determine the Human Health Risk. *International Journal of Current Research in Chemistry and Pharmaceutical Sciences, 4*(5), 31-35.

Ventola, C. L. (2015). The antibiotic resistance crisis: part 1: causes and threats. *Pharmacy and Therapeutics, 40*(4), 277.

Wang, B., Wei, S., Guo, L., Wang, Y., Liang, Y., Xu, B., . . . Chen, X. (2017a). Effect of deposition parameters on properties of TiO2 films deposited by reactive magnetron sputtering. *Ceramics International, 43*(14), 10991-10998.

Wang, K.-C., Shen, P.-S., Li, M.-H., Chen, S., Lin, M.-W., Chen, P., & Guo, T.-F. (2014). Low-temperature sputtered nickel oxide compact thin film as effective electron blocking layer for mesoscopic NiO/CH3NH3PbI3 perovskite heterojunction solar cells. *ACS applied materials & interfaces, 6*(15), 11851-11858.

Wang, Z.-l., He, R.-z., Tu, B., Cao, X., He, J.-s., Xia, H.-s., . . . Wu, Z.-j. (2017b). Enhanced biocompatibility and osseointegration of calcium titanate coating on titanium screws in rabbit femur. *Journal of Huazhong University of Science and Technology [Medical Sciences], 37*(3), 362-370.

Waykar, R. G., Pawbake, A. S., Kulkarni, R. R., Jadhavar, A. A., Funde, A. M., Waman, V. S., . . . Jadkar, S. R. (2016). Influence of RF power on structural, morphology, electrical, composition and optical properties of Al-doped ZnO films deposited by RF magnetron sputtering. *Journal of Materials Science: Materials in Electronics, 27*(2), 1134-1143.

Weber, D. J., Rutala, W. A., Miller, M. B., Huslage, K., & Sickbert-Bennett, E. (2010). Role of hospital surfaces in the transmission of emerging health care-associated pathogens: norovirus, Clostridium difficile, and Acinetobacter species. *American journal of infection control, 38*(5), S25-S33.

Wen, L., Feil, S., Wolters, M., Thunemann, M., Regler, F., Schmidt, K., . . . Gawaz, M. (2018). A shear-dependent NO-cGMP-cGKI cascade in platelets acts as an auto-regulatory brake of thrombosis. *Nature communications, 9*(1), 4301.

Wendlandt, R., Thomas, M., Kienast, B., & Schulz, A. (2016). In-vitro evaluation of surgical helmet systems for protecting surgeons from droplets generated during orthopaedic procedures. *Journal of Hospital Infection, 94*(1), 75-79.

Wettlaufer, L., & Penn, D. (2018). Medical Devices: Definition and Clinical Testing. *Drug Discovery and Evaluation: Methods in Clinical Pharmacology*, 1-12.

Wojcieszak, D., Mazur, M., Kaczmarek, D., Mazur, P., Szponar, B., Domaradzki, J., & Kepinski, L. (2016). Influence of the surface properties on bactericidal and fungicidal activity of magnetron sputtered Ti–Ag and Nb–Ag thin films. *Materials Science and Engineering: C, 62*, 86-95.

Wuu, D.-S., Horng, R.-H., Tseng, W.-H., Lin, W.-T., & Kung, C.-Y. (2000). Influences of temperature ramping rate on GaN buffer layers and subsequent GaN overlayers grown by metalorganic chemical vapor deposition. *Journal of crystal growth, 220*(3), 235-242.

Xu, L.-C., & Siedlecki, C. A. (2007). Effects of surface wettability and contact time on protein adhesion to biomaterial surfaces. *Biomaterials, 28*(22), 3273-3283.

Xu, S., Ma, X., Tang, G., & Zhang, Q. (2015). Air annealing effect on scratch behaviour of BCN films. *Surface Engineering, 31*(7), 549-555.

Xu, Z., Qiu, Z., Liu, Q., Huang, Y., Li, D., Shen, X., . . . Tang, Y. (2018). Converting organosulfur compounds to inorganic polysulfides against resistant bacterial infections. *Nature communications, 9*.

Yilmaz, B., Doğan, S., & Çelikler Kasimoğullari, S. (2018). Hemocompatibility, cytotoxicity, and genotoxicity of poly (methylmethacrylate)/nanohydroxyapatite nanocomposites synthesized by melt blending method. *International Journal of Polymeric Materials and Polymeric Biomaterials, 67*(6), 351-360.

Yu, J., Sun, X., Gong, H., Dong, L., Zhao, M., Wan, R., . . . Li, D. (2017a). Influence of Ag concentration on microstructure, mechanical properties and cytocompatibility of nanoscale Ti-Ag-N/Ag multilayers. *Surface and Coatings Technology, 312*, 128-133.

Yu, K., Lo, J. C., Yan, M., Yang, X., Brooks, D. E., Hancock, R. E., . . . Kizhakkedathu, J. N. (2017b). Anti-adhesive antimicrobial peptide coating prevents catheter associated infection in a mouse urinary infection model. *Biomaterials, 116*, 69-81.

Zaporojtchenko, V., Podschun, R., Schürmann, U., Kulkarni, A., & Faupel, F. (2006). Physico-chemical and antimicrobial properties of co-sputtered Ag–Au/PTFE nanocomposite coatings. *Nanotechnology, 17*(19), 4904.

Zhabrev, V., Bystrov, Y. A., Efimenko, L., Komlev, A., Baryshnikov, V., Kolomiitsev, A., & Shapovalov, V. (2004). The effect of thermal treatment on the structure of tantalum oxide films grown on titanium. *Technical physics letters, 30*(5), 396-398.

Zhang, D., Qi, Z., Wei, B., Wu, Z., & Wang, Z. (2017a). Anticorrosive yet conductive Hf/Si 3 N 4 multilayer coatings on AZ91D magnesium alloy by magnetron sputtering. *Surface and Coatings Technology, 309*, 12-20.

Zhang, H., Luo, C. G., Duo, S. W., Liu, Q., Wen, R. C., Yuan, M. Y., & Wu, Y. L. (2017b). *Effect of Deposition Time on Hardness and Bonding Strength of Magnetron Sputtered TiN Coatings on 316 Stainless Steel.* Paper presented at the Key Engineering Materials.

Zhang, L., Peng, H., Qin, Q., Fan, Q., Bao, S., & Wen, Y. (2018). Effects of annealing on hardness and corrosion resistance of 60NiTi film deposited by magnetron sputtering. *Journal of Alloys and Compounds, 746, 45-53.*

Zhao, P., Liu, D., Xu, X., & Zhang, F. (2007). *Influence on optical and electrical properties of silver layer by adjoining $Ta_2O_5$ layers.* Paper presented at the 3rd International Symposium on Advanced Optical Manufacturing and Testing Technologies: Advanced Optical Manufacturing Technologies.

Zhao, W., Zhou, Q., Zhang, Y., Chen, Y., Ren, J., Zhao, S., & Zheng, J. (2016). Formation of silver single crystal polyhedra with high catalytic activity toward oxidation of ascorbic acid in highly ordered SiO 2 cavities. *Journal of Electroanalytical Chemistry, 768*, 41-46.

## LIST OF PUBLICATIONS

| No | List of paper | Status |
|---|---|---|
| 1) | Alias, R., Mahmoodian, R., Rizwan, M., & Hamdi, M. (2018). Study the effect of thermal annealing on adhesion strength of Silver-tantalum oxide thin film deposited by reactive magnetron sputtering. *Journal of Adhesion Science &Technology*, 1-18. | ISI Published Q3 IF: 1.210 |
| 2 | Rizwan, M., Alias, R., Zaidi, U. Z., Mahmoodian, R., & Hamdi, M. (2018). Surface modification of valve metals using plasma electrolytic oxidation for antibacterial applications: A review. *Journal of Biomedical Materials Research Part A, 106*(2), 590-605. | ISI Published Q2 IF: 3.221 |
| 3 | R Alias, R Mahmoodian, MHA Shukor, YB Seok, M Muhamad. (2018). Enhancement of as-sputtered silver-tantalum oxide thin film coating on biomaterial stainless steel by surface thermal treatment, AIP Conference Proceedings 1948 (1), 020003 | ISI Proceeding Published |
| 4 | Alias, R., Mahmoodian, R. & Hamdi, M. Development and characterization of a multilayer silver/silver-tantalum oxide thin film coating on stainless steel for biomedical applications. *International Journal of Adhesion & Adhesive,* 92, 89-98. | ISI Published Q2 IF: 2.5 |
| 5 | Alias, R., Mahmoodian, R. & Hamdi, M. Effect of temperature ramping rate on the morphology, phase and adhesion strength of Ag-$Ta_2O_5$ thin film. *Journal of Metals, Minerals and Materials.* | Under-review Revise Submitted Q1 IF: 2.305 |

| | | |
|---|---|---|
| 6 | **Alias, R**., Mahmoodian, Genasan, K., Vellasamy K.M. & Hamdi, M. Mechanical, antibacterial, and biocompatibility mechanism of PVD grown Silver-Tantalum-oxide-based Nanostructured thin film on stainless steel 316L for surgical applications. *Materials Science and Engineering C* | Under-review<br>Q1<br>IF: 4.959 |